In-situ study of Ga_2O_3 thermal expansion and epitaxy by synchrotron based x-ray diffraction and reflection high-energy electron diffraction

Dissertation
zur Erlangung des akademischen Grades

Doctor rerum naturalium

(Dr. rer. nat.)

im Fach: Physik

Spezialisierung: Experimentalphysik

eingereicht an der

Mathematisch-Naturwissenschaftlichen Fakultät

der Humboldt-Universität zu Berlin

von

M.Sc. Zongzhe Cheng

Präsidentin der Humboldt-Universität zu Berlin:
Prof. Dr.-Ing. Dr. Sabine Kunst
Dekan der Mathematisch-Naturwissenschaftlichen Fakultät
Prof. Dr. Elmar Kulke

Gutachter/innen:
1. Prof. Dr. Henning Riechert
2. Prof. Dr. Ferdinand Scholz
3. PD Dr. Martin Schmidbauer

Tag der mündlichen Prüfung: 16. August 2019

To my wife Jing Ma

and our parents Jiakai, Lifen, Jianguo, and Shuzhen

for their love, trust, and support.

Zusammenfassung

Diese Arbeit präsentiert eine umfassende in-situ Studie zur thermischen Ausdehnung von β-Ga_2O_3 im Temperaturbereich von Raumtemperatur (RT) bis 1200 K sowie zum Wachstum dünner Ga_2O_3 Schichten durch plasmaunterstützte Molekularstrahlepitaxie (MBE). Hierfür kamen synchrotron-basierte hochauflösende Röntgenbeugung (HRXRD) sowie die Beugung hochenergetischer Elektronen bei Reflexion (RHEED) zum Einsatz. Die experimentellen Befunde gestatten detaillierte quantitative Aussagen zu den Ausdehnungskoeffizienten (CTE) von β-Ga_2O_3 und erlauben ein tieferes Verständnis des Wachstumsprozesses von Ga_2O_3 sowohl im Rahmen der Homo- als auch der Heteroepitaxie.

Die thermische Ausdehnung von einkristallinem β-Ga_2O_3 Bulkmaterial wurde präzise mittels in-situ HRXRD sowie Beugung unter streifendem Einfall (GID) in einem Temperaturfenster zwischen 298 und 1200 K untersucht. Das experimentell bestimmte Ausdehnungsverhalten ist in guter Übereinstimmung mit numerischen Fits auf Grundlage des Einstein-Modells. Die bestimmten CTEs zeigen eine starke Anisotropie, wobei α_a, der Ausdehnungskoeffizient entlang der a-Achse, etwa der Hälfte von α_b und α_c, den Koeffizienten entlang der Achsen b und c, entspricht. Für das Wachstum dünner homoepitaktischer, (100)-orientierter β-Ga_2O_3 Schichten konnte durch RHEED-Oszillationen zusammen mit hochauflösender Transmissionselektronenmikroskopie (HRTEM) und Rasterkraftmikroskopie (AFM) ein Lage-für-Lage Wachstumsmodus nachgewiesen werden. In den homoepitaktischen Schichten wurden ausschließlich Kristallzwillinge gefunden, die auf die Zweifachpositionierung der Adatome auf der (100)-Ebene während des Wachstums zurückzuführen sind. Für die Heteroepitaxie von Ga_2O_3 auf Sapphirsubstraten mit unterschiedlichen Oberflächenorientierungen wurde die Phasenbildung und -stabilisierung sowie der Abbau von Verspannungen untersucht. Auf [0001]-orientiertem Sapphir beginnt das Wachstum zunächst mit α-Ga_2O_3, oberhalb einer kritischen Schichtdicke von etwa 2.1 nm setzt es sich durch die Bildung von β-Ga_2O_3 fort. Jedoch lässt sich einkristallines α-Ga_2O_3 mit Schichtdicken größer als 10 nm kohärent auf Sapphirsubstraten anderer Orientierungen (a-, m- und r-plane) abscheiden. Mithilfe von in-situ HRXRD Analytik konnte gezeigt werden, dass die anisotrope Verspannung einer dünnen α-Ga_2O_3 Schicht sehr rasch innerhalb der ersten Nanometer relaxiert.

Schlüsselwörter: Hochauflösende Röntgenbeugung, kinematische Näherung,

Lage-für-Lage Wachstum, Molekularstrahlepitaxie, Beugung hochenergetischer Elektronen bei Reflexion, Verspannungsrelaxation, thermische Ausdehnung, transparente halbleitende Oxide

Abstract

This thesis presents a comprehensive *in-situ* study on the thermal expansion of β-Ga_2O_3 from room temperature (RT) to 1200 K, and the thin film growth of Ga_2O_3 as carried out by oxygen plasma assisted molecular beam epitaxy (MBE) using synchrotron-based high-resolution x-ray diffraction (HRXRD) and reflection high-energy electron diffraction (RHEED). The obtained results provide a quantitative analysis on the coefficients of thermal expansion (CTE) of β-Ga_2O_3, and a deeper understanding in the growth process of Ga_2O_3 in both homoepitaxy and heteroepitaxy.

The thermal expansion property of single-crystalline bulk β-Ga_2O_3 has been precisely characterized by *in-situ* HRXRD including grazing incidence diffraction (GID) in the temperature window between 298 and 1200 K. The measured thermal expansion results are in good agreement with the fittings based on the Einstein model. The evaluated CTEs show a strong anisotropy, whereby α_a, the coefficient along axis *a*, is approximately half of α_b and α_c, the coefficients along axis *b* and axis *c*. As for the thin film epitaxy, a layer-by-layer growth mode of (100)-oriented β-Ga_2O_3 homoepitaxy has been evidenced by the RHEED oscillations together with high-resolution transmission electron microscopy (HRTEM) and atomic force microscopy (AFM) results. In the β-Ga_2O_3 homoepitaxial films, twin domains are exclusively found, and have been attributed to a double positioning of the adatoms on the (100) plane during growth. In heteroepitaxy, the phase stabilization and strain relaxation of Ga_2O_3 grown on sapphire substrates with different surface orientations have been studied. On *c*-plane sapphire the growth starts with α-Ga_2O_3 followed by a subsequent formation of monoclinic β-Ga_2O_3 above a critical thickness of around 2.1 nm. However, single-crystalline α-Ga_2O_3 can be coherently deposited with thicknesses above 10 nm on sapphire substrates with other surface orientations (*a*-, *m*-, and *r*-plane). It is found by *in-situ* HRXRD that the strain in heteroepitaxial α-Ga_2O_3 thin film is anisotropically distributed and relaxes rapidly in the first a few nanometers.

Keywords: High-resolution x-ray diffraction, kinematic approximation, layer-by-layer growth, molecular beam epitaxy, reflection high-energy electron diffraction, strain relaxation, thermal expansion, transparent semiconducting oxides

Scientific contributions

Peer-reviewed publications

Z. Cheng, M. Hanke, Z. Galazka, A. Trampert
Thermal expansion of single-crystalline β-Ga_2O_3 from 298K to 1200K as studied by synchrotron-based high resolution x-ray diffraction
Applied Physics Letters **113** (2018), 182102

Z. Cheng, M. Hanke, Z. Galazka, A. Trampert
Growth mode evolution during (100)-oriented β-Ga_2O_3 homoepitaxy
Nanotechnology **29** (2018), 395705

Z. Cheng, M. Hanke, P. Vogt, O. Bierwagen, A. Trampert
Phase formation and strain relaxation of Ga_2O_3 on various sapphire orientations as studied by synchrotron-based x-ray diffraction
Applied Physics Letters **111** (2017), 162104

T. Krause, M. Hanke, L. Nicolai, **Z. Cheng**, M. Niehle, A. Trampert, M. Kahnt, G. Falkenberg, C. G. Schroer, J. Hartmann, H. Zhou, H.-H. Wehmann, A. Waag
Structure and composition of isolated core-Shell (In,Ga)N/GaN rods based on nanofocus x-ray diffraction and scanning transmission electron microscopy
Physical Review Applied **7** (2017), 024033

T. Krause, M. Hanke, **Z. Cheng**, M. Niehle, A. Trampert, M. Rosenthal, M. Burghammer, J. Ledig, J. Hartmann, H. Zhou, H.-H. Wehmann, A. Waag
Nanofocus x-ray diffraction and cathodoluminescence investigations into individual core-shell (In,Ga)N/GaN rod light emitting diodes
Nanotechnology **27** (2016), 325707

Conference contributions

P. Mazzolini, P. Vogt, **Z. Cheng**, M. Hanke, R. Schewski, C. Wouters, M. Albrecht, O. Bierwagen
Faceting and catalysis during molecular beam epitaxy of Ga_2O_3 homoepitaxial thin film
Compound semiconductor week, Cambridge, Massachusetts, USA (2018)

Z. Cheng, M. Hanke, Z. Galazka, A. Trampert
Growth mode evolution during (100)-oriented β-Ga_2O_3 homoepitaxy
Spring meeting of the German physical society (DPG-Frühjahrstagung), Berlin, Germany (2018)

Z. Cheng, M. Hanke, Z. Galazka, A. Trampert
In-situ growth mode study of homoepitaxial (100)-oriented β-Ga_2O_3
The 9th joint BER II and BESSY II user meeting, Berlin, Germany (2017)

Z. Cheng, M. Hanke, O. Bierwagen, Z. Galazka, A. Trampert
Strain dynamics of heteroepitaxial grown α-Ga_2O_3 and homoepitaxial growth of β-Ga_2O_3 as studied by synchrotron based HRXRD and RHEED
The 2nd international workshop on Ga_2O_3 and related materials, Parma, Italy (2017)

Z. Cheng, M. Hanke, N. Boudet, A. Trampert
Growth observations of Ga_2O_3 on various sapphire orientations as studied by synchrotron-based x-ray diffraction
ESRF User meeting, Grenoble, France (2017)

Z. Cheng, P. Vogt, R. Schewski, O. Bierwagen, M. Albrecht, A. Trampert, M. Hanke
Pseudomorphic growth and relaxation of α-Ga_2O_3 on sapphire substrate
Spring meeting of the German physical society (DPG-Frühjahrstagung), Dresden, Germany (2016)

Z. Cheng, P. Vogt, R. Schewski, O. Bierwagen, M. Albrecht, M. Hanke, A. Trampert
Pseudomorphic growth of α-Ga_2O_3 layers and crystallization of amorphous Ga_2O_3 layer by annealing
The 7th joint BER II and BESSY II user meeting, Berlin, Germany (2015)

List of abbreviations

2D	two-dimensional
3D	three-dimensional
AFM	atomic force microscopy
a. u.	arbitrary units
BESSY II	Berliner Elektronenspeicherring-Gesellschaft für Synchrotronstrahlung II
CBM	conduction band minimum
CCD	charge-coupled device
CTR	crystal truncation rod
EFG	edge-defined film-fed growth
FET	field effect transistor
FWHM	full width at half maximum
FZ	floating zone
GID	grazing incidence diffraction
HRTEM	High resolution transmission electron microscopy
HRXRD	high-resolution x-ray diffraction
HZB	Helmholtz-Zentrum Berlin
MBE	molecular beam epitaxy
MFC	mass-flow controller
Mist-CVD	mist-chemical vapor deposition
MOCVD	metal-organic chemical vapor deposition
PECVD	plasma-enhanced chemical vapor deposition
PLD	pulsed laser deposition
QMS	quadrupole mass spectrometry
RF	radio-frequency
RHEED	reflection high-energy electron diffraction
RSM	reciprocal space map
SSP	single-side-polished
TSO	transparent semiconducting oxide
UHV	ultra-high vacuum
VBM	valence band maximum

Table of Contents

Zusammenfassung v
Abstract vii
Scientific contributions ix
Abbreviations xi

1 Introduction **1**

2 An introduction to Ga_2O_3 **5**
2.1 Polymorphs of Ga_2O_3 5
2.2 Structure and properties of α-Ga_2O_3 and β-Ga_2O_3 6

3 Growth and characterization methods **13**
3.1 Molecular beam epitaxy 13
3.2 *In-situ* analytical methodologies 14
3.2.1 Synchrotron-based HRXRD 16
3.2.2 Reflection high-energy electron diffraction 21
3.2.3 Quadrupole mass spectroscopy 23

4 Thermal expansion of β-Ga_2O_3 **25**
4.1 Motivation 25
4.2 Thermal expansion of β-Ga_2O_3 as probed by HRXRD 26
4.3 Analysis of the anisotropic thermal expansion 28
4.4 Summary 32

5 Growth mode evolution of (100)-oriented β-Ga_2O_3 homoepitaxy **35**
5.1 Motivation 35
5.2 Preparation of substrates 36
5.3 Layer-by-layer growth mode 36
5.4 Formation of twin domains 40
5.5 The growth mode at higher growth rates 47
5.6 Summary 49

6 Heteroepitaxy of Ga_2O_3 on various oriented sapphire substrates **51**
6.1 Kinematic scattering approximation 52
6.2 The structure of Ga_2O_3 on *c*-plane sapphire substrates 59
6.2.1 Preparation of substrates 60
6.2.2 β-Ga_2O_3 formation on *c*-plane sapphire substrate 60
6.3 Growth and strain relaxation of single crystalline α-Ga_2O_3 thin film 68
6.3.1 Strain relaxation of high quality α-Ga_2O_3 grown on *a*-plane sapphire substrates 69
6.3.2 α-Ga_2O_3 stabilized on *m*-plane sapphire substrates . . . 73
6.3.3 α-Ga_2O_3 stabilized on *r*-plane sapphire substrates 77
6.4 Summary 79

7 Summary and outlook **81**

Bibliography **85**

Appendices **97**

A Sketch of the PHARAO beamline **99**
A.1 Combination of MBE and diffractometer 99
A.2 The six-circle diffractometer 100

B Code of numerical simulation **101**

Acknowledgement **103**

1 Introduction

Since an investigation of the phase equilibria in the Al_2O_3-Ga_2O_3-H_2O system and a comprehensive introduction of the five Ga_2O_3 polymorphs were reported by Roy *et al.* in 1952,[1] Ga_2O_3 has been studied for a long time in its fundamental properties and applications. Ga_2O_3 has a large bandgap of around 5 eV, and therefore is transparent to photons with wavelength down to approximately 235 nm. Electrically, Ga_2O_3 can be tuned from insulating to conducting, depending on the growth condition and doping.[2–5] The breakdown voltage of Ga_2O_3 is up to around 8 MV/cm, which is much higher than Si and 4H-SiC, the commonly used materials for high-power electronics. These fascinating physical properties make Ga_2O_3 a very promising candidate for applications in electronic devices, such as solar-blind ultra-violet (UV) photodetectors,[6–8] gas sensors (O_2, H_2, and CH_4),[9–14] field-effect transistor (FET),[15–20] and other high-power electronics.[21]

As commonly identified, there are five different phases of Ga_2O_3, which are named as α, β, γ, δ, and ϵ. α-Ga_2O_3 is a meta-stable form at ambient condition, and was first reported by Weiser and Milligan.[22] Compared with the monoclinic β-phase, though α-Ga_2O_3 is less stable at ambient condition, it has a more common rhombohedral structure. This crystal structure makes it easier to control the orientation and the rotational domains as grown on substrates with the same surface symmetry, such as sapphire (α-Al_2O_3).[23–25] Among the five polymorphic phases, the β-modification is the most stable structure and has drawn most of the attention in Ga_2O_3 study. In addition to the epitaxial or bulk growth of β-Ga_2O_3, Roy *et al.* have presented the conversion of the other polymorphs to the monoclinic β-Ga_2O_3 through a thermal treatment process.[1]

In order to pave the way towards applications for Ga_2O_3, we need to understand the fundamental properties of the material itself and the epitaxial growth process in particular, which would therefore allow us to improve the crystal quality of the thin films. For this research purpose, the molecular beam epitaxy (MBE) is a very suitable growth method, since it can control the growth very precisely, in respective of the film thickness and material purity. The com-

bined synchrotron-based high-resolution x-ray diffraction (HRXRD) and reflection high-energy electron diffraction (RHEED) enable a direct *in-situ* access to the crystallography of the thin film during homo- and heteroepitaxial growth and the unit cell deformation within strain relaxation and thermal expansion. The structural information during the growth and at different temperatures, as studied by the *in-situ* analytic tools, is the main focus in this thesis.

The scope of this thesis

This thesis is distributed into the following chapters:

Chapter 2 gives an introduction of Ga_2O_3, concerning its applications and some of its fundamental properties, such as crystal structure, bandgap, and thermal conductivity.

Chapter 3 introduces the MBE system and the analytical tools used in this thesis. All the epitaxial and thermal expansion studies in this study were carried out at the plasma-assisted MBE with continuous *in-situ* characterizations, including synchrotron-based HRXRD and RHEED.

Chapter 4 demonstrates the anisotropic thermal expansion behavior of the bulk β-Ga_2O_3 in respect of crystal directions. The Einstein model fitting, which agrees very well with the experimental results, is applied to interpret CTEs of β-Ga_2O_3.

Chapter 5 presents the growth mode of (100)-oriented β-Ga_2O_3 homoepitaxy and the formation of defects in the thin film. A layer-by-layer growth mode is evidenced by the RHEED specular spot intensity oscillation together with the high-resolution transmission electron microscopy (HRTEM) and atomic force microscopy (AFM) results.[26, 27] Twin domains and stacking faults are probed by HRTEM and the formation mechanism is interpreted by the double positioning of the unit cells during growth.

Chapter 6 talks about the phase stabilization and strain relaxation of Ga_2O_3 on sapphire substrates in different surface orientations. The single-crystalline α-Ga_2O_3 can be deposited above 10 nm on sapphire substrates, and the lattice mismatch induced strain is anisotropically distributed in the thin film, and rapidly

relaxed during the growth.

Chapter 7 summarizes the results of the thesis and presents an outlook.

2 An introduction to Ga_2O_3

This chapter gives a general introduction of Ga_2O_3, a wide bandgap semiconducting (or semi-insulating depending on growth condition) group-III sesquioxide, which has been intensively investigated in this work. Five polymorphs of Ga_2O_3, regarding the crystal structure and the development of different growth methods, are introduced. Physical properties of the most relevant α- and β-modifications such as band structure, break-down field and thermal conductivity are reviewed, demonstrating its great potential in a wide variety of applications. The results from recent research and the motivation of our study in Ga_2O_3 are also addressed.

2.1 Polymorphs of Ga_2O_3

The five polymorphs of Ga_2O_3, namely α, β, γ, δ, and ϵ were first reported by Roy *et. al.* in 1952.[1] The structure of these five phases have been dedicatedly studied and are commonly known as corundum for α, monoclinic for β, defect spinel for γ, and orthorhombic for both δ and ϵ.[28–33] Some of their concerned properties are summarized in table 2.1. In addition to the structure information, the energies of Ga_2O_3 polymorphs calculated within the general gradient approximation based on the density functional theory (DFT) are also presented. It indicates that in a condition with low temperature and ambient pressure, the monoclinic β-Ga_2O_3 is thermodynamically the most stable phase,[28] which agrees well with the experimental results.[1, 34, 35] One featured property of Ga_2O_3 is the large bandgap as shown in table 2.1, varying slightly in different phases, thereof α-Ga_2O_3 has the largest bandgap of approximately 5 eV. Another highly attractive property is the very high breakdown field of β-Ga_2O_3, which is expected to be about 8 MV cm^{-1} and has already been demonstrated to around 3.8 MV cm^{-1} in Sn-doped β-Ga_2O_3 metal-oxide-semiconductor field-effect transistor (MOSFET).[15] These two fascinating physical properties empower Ga_2O_3 to be an extremely promising candidate for a large variety of applications in electronics and optoelectronics, which will be talked in details later

Table 2.1 Summary of some physical properties of Ga_2O_3 polymorphs.

	Space group	Lattice parameters (Å) [1, 28, 30, 36–39]	Energy/eV (T = 0 K) [29]	Bandgap/eV [40, 41]
α-Ga_2O_3	$R\bar{3}/c$	a = 4.98-5.04 c = 13.4-13.6	-31.084	5.03-5.08
β-Ga_2O_3	C2/m	a = 12.12-12.34 b = 3.03-3.04 c = 5.80-5.87 β = 103.83°	-31.158	4.66-4.69
γ-Ga_2O_3	$Fd\bar{3}/m$	a = 8.24-8.30	-30.900	4.4-5.0
δ-Ga_2O_3	$Ia\bar{3}$ Suggested as a nanocrystalline form of ϵ-Ga_2O_3.	a = 9.4-10.0		
ϵ-Ga_2O_3	$Pna2_1$	a = 5.06-5.12 b = 8.69-8.79 c = 9.3-9.4	-31.072	4.9

in this chapter.

2.2 Structure and properties of α-Ga_2O_3 and β-Ga_2O_3

In this thesis, the research has been focused on α-Ga_2O_3 and β-Ga_2O_3 out of the five phases mentioned above. Compared with the other phases, α-Ga_2O_3 possesses the largest bandgap, and it shares the same crystal symmetry with many other materials that have been widely used in the field of semiconductor research such as sapphire and wurtzite III-V compounds. However, it is a meta-stable phase at ambient condition, therefore the epitaxial growth of single crystalline α-Ga_2O_3 is still challenging especially in MBE. β-Ga_2O_3 is more stable at ambient condition, and has been intensively investigated in its crystal structure, bulk growth, thin film epitaxy and electrical structure. The recent development in melt-growth methods improves the availability of high quality β-Ga_2O_3 bulk substrates, which therefore offers more opportunities for the studies in its ho-

moepitaxy and bulk properties. A general introduction of these two phases in several aspects is given.

α-modification of gallium oxide

As listed in table 2.1, the crystal structure of α-Ga_2O_3 is described by space group $R\bar{3}/c$, the same as sapphire.[1, 42] It is sketched in figure 2.1, in which the Ga atoms are octahedrally coordinated by six oxygen atoms. The lattice mismatch between α-Ga_2O_3 and α-Al_2O_3 is 3.4% along c-axis and 4.6% along a-axis (lattice parameters of α-Al_2O_3: a = 4.758 Å, c = 12.991Å). Because of the same crystal structure and relatively small lattice mismatch, the study on α-Ga_2O_3 heteroepitaxy has been mainly carried out on sapphire substrates.[23–25, 43–45] However, α-Ga_2O_3 is thermodynamically less stable than β-Ga_2O_3 at both the ambient and the epitaxial growth conditions, therefore in metal-organic chemical vapour deposition (MOCVD), pulsed-laser deposition (PLD) and MBE, α-Ga_2O_3 only grows up to a critical thickness of 3 monolayers on *c*-plane oriented sapphire substrates in the temperature window between 923 and 1073 K.[25, 45] In 2008, α-Ga_2O_3 single crystalline films were successfully deposited on *c*-plane sapphire substrate to a thickness of 240 nm at a growth rate of a few nm per minute by mist chemical vapor deposition (Mist-CVD).[24] In addition to the epitaxial growth, α-Ga_2O_3 can also be transformed from β-Ga_2O_3 under a pressure of 4.4 GPa at around 1273 K.[46]

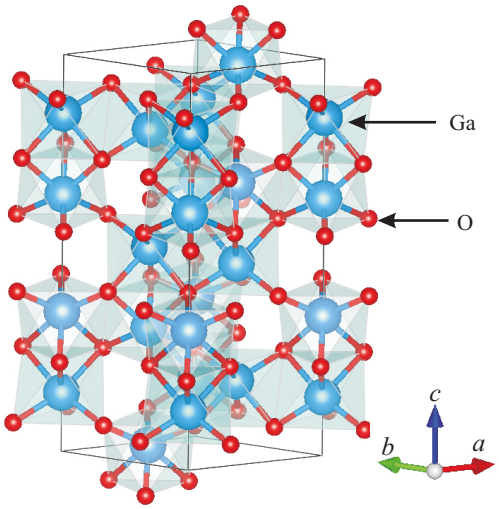

Figure 2.1 The crystal structure of α-Ga_2O_3 is viewed along approximately the $[11\bar{2}0]$ direction. It has a corundum crystal structure. In this sketch, Ga and O atoms are colored in blue and red, respectively.

The band structure of α-Ga_2O_3, as shown in figure 2.2, is calculated by He

et al. based on DFT.[41] The conduction band minimum (CBM) is at Γ, and the calculated average value of electron effective mass is $m_0^* = 0.276 m_0$. Unlike the conduction band, the valence band is almost flat, indicating a large effective mass for holes in it. The direct bandgap at Γ is 5.08 eV, and the indirect bandgap between Γ and L is 5.03 eV. On account of such a large bandgap, α-Ga_2O_3 is transparent in the visible light range, and regarding the wavelength down to the deep UV regime, it therefore has a potential in the application of solar-blind UV photodetectors.

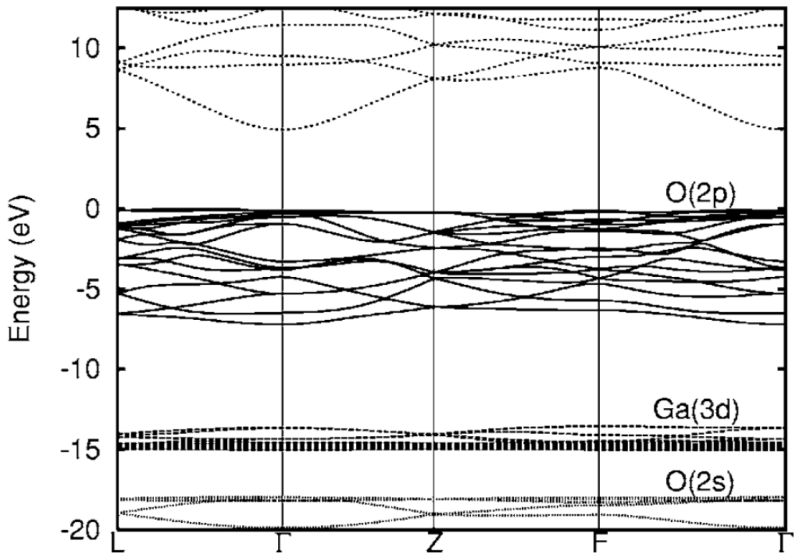

Figure 2.2 The band structure of α-Ga_2O_3, and the top of the valence band is aligned to zero. The **k** points are Γ = (000), L = $(0\frac{1}{2}0)$, Z = $(\frac{1}{2}\frac{1}{2}\frac{1}{2})$, F = $(\frac{1}{2}\frac{1}{2}0)$.[41]

β-modification of gallium oxide

The β-modification has a monoclinic structure (lattice parameters are listed in table 2.1) and appears thermodynamically more stable than the other phases.[47] The crystal structure of β-Ga_2O_3 is sketched in figure 2.3. In a β-Ga_2O_3 unit cell, there are two types of Ga atoms and three types of oxygen atoms in respect of crystallography. One type of Ga atoms is in a tetrahedral coordination geometry [Ga (I)], and the other one in an octahedral coordination site [Ga (II)].[48, 49] Such a crystal structure leads to anisotropy in many of its physical properties. In the recent research, Ueda and Hosono have reported that the electrical conductivity and carrier mobility along [001] are one order of magnitude smaller than these along [010].[50] Schubert *et al.* reported a strong anisotropy of the phonon modes in the crystal, which is important for the thermal conductivity

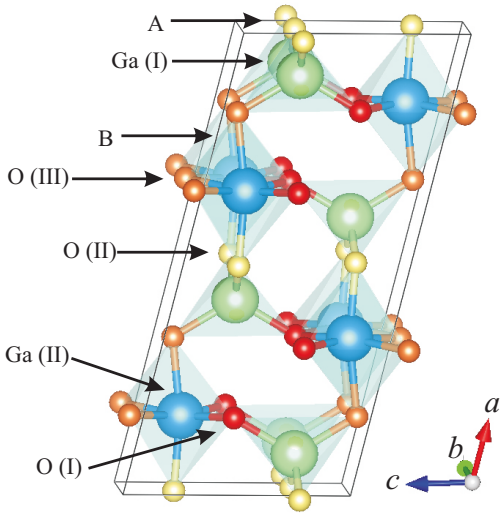

Figure 2.3 The crystal structure of β-Ga_2O_3 is viewed along roughly the *b* direction. In the lattice, there are two inequivalent Ga sites and three inequivalent O sites. Half of the Ga atoms are in the slightly distorted tetrahedra sites Ga (I) formed by four O atoms, and the rest of Ga atoms are in the highly distorted octahedra sites Ga (II) with six O atoms. The (100) plane has two different surface terminations A and B. The (100)-B has lower surface energy, and makes the (100) plane can be easily cleaved.

and expansion studies.[51] Slomski *et al.* have observed the expected anisotropy of the thermal conductivity that it is around 29 W/mK (27 W/mK reported by Guo *et al.*) along the [010] direction, which is higher than those along the other directions.[52, 53]

In figure 2.4, the DFT calculation as performed by He *et al.* shows a very flat valence band of β-Ga_2O_3 in its band structure, similar like α-Ga_2O_3.[41] The CBM locates at Γ, and the electron effective mass is $m_0^* = 0.342 m_0$. The direct bandgap at point Γ is 4.69 eV, which is 0.03 eV broader than the indirect bandgap at M-Γ. Though it is smaller than α-Ga_2O_3, it is still larger than most of the widely used materials listed in table 2.2. Because of this large bandgap, though a little bit smaller than the α-phase, it is still transparent up to (in respective of energy) the optical regime of deep UV. Therefore the thermodynamically more stable β-Ga_2O_3 has also been considered as a promising material candidate for solar-blind photodetectors working in the deep UV range.[7, 54, 55]

As shown in table 2.2, β-Ga_2O_3 is expected to have a breakdown field of around 8 $MVcm^{-1}$, which is much larger than for Si, GaAs, SiC, and GaN, these materials generally used in high-power electronics.[56, 57] However, the low thermal conductivity of β-Ga_2O_3 is a physical property that limits its applications, since it requires more heat engineering in the β-Ga_2O_3-based high power devices, like heat-sinks using diamond or SiC.[39, 52, 53] The heat capacity

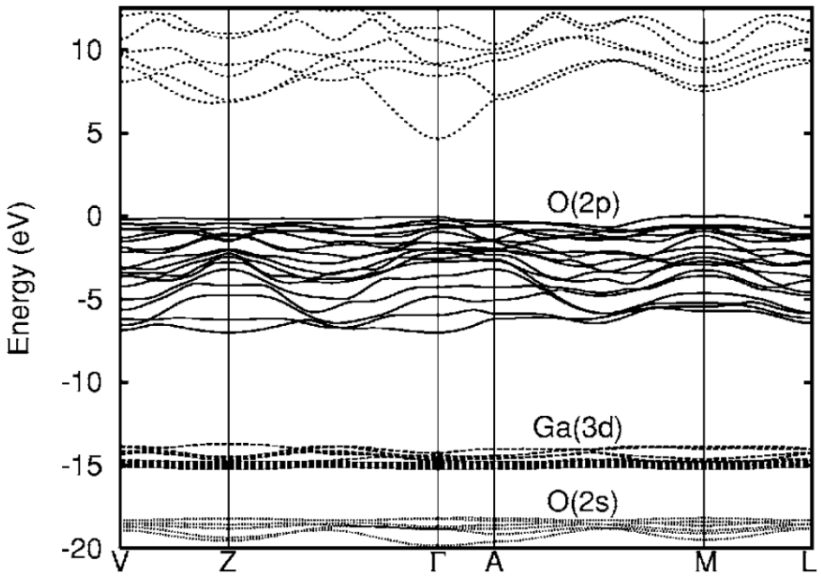

Figure 2.4 The band structure of β-Ga_2O_3. The top of the valence band is aligned to be 0 eV. The **k** points are $\Gamma = (000)$, $A = (00\frac{1}{2})$, $Z = (\frac{1}{2}\frac{1}{2}0)$, $M = (\frac{1}{2}\frac{1}{2}\frac{1}{2})$, $L = (0\frac{1}{2}\frac{1}{2})$, $V = (0\frac{1}{2}0)$.[41]

of β-Ga_2O_3 has been investigated by Guo *et al.* using a differential scanning calorimeter.[52] The fitted Debye temperature is 738 K, which is lower than the value of 872 K as predicated by the first-principles calculation.[30]

Table 2.2 Properties of β-Ga_2O_3 relative to other more commonly used semiconductors. [39]

	Si	GaAs	4H-SiC	GaN	Diamond	β-Ga_2O_3
Bandgap, E_g (eV)	1.1	1.43	3.25	3.4	5.5	4.85
Breakdown field, E_C (MV/cm)	0.3	0.4	2.5	3.3	10	8
Electron mobility, μ (cm^2C/Vs)	1480	8400	1000	1250	2000	300
Thermal conductivity, λ (W/cm K)	1.5	0.5	4.9	2.3	20	0.1-0.3

The development in the growth of large diameter β-Ga_2O_3 bulk crystals, especially using the melt growth methods, is an important factor that drives the increasing interest in studies of this material. Its heteroepitaxial growth on *c*-plane sapphire substrates has been carried out by MBE, PLD, and MOCVD, however the crystal quality is not as good as the homoepitaxial film.[45] The

heteroepitaxial β-Ga_2O_3 thin films have been observed containing in-plane rotational domains, which significantly lowers the electron mobility at the domain boundaries. Therefore the β-Ga_2O_3 homoepitaxy becomes highly interesting, since homoepitaxy is expected to grow thin films with higher crystal quality. The homoepitaxial substrates can be prepared from the single crystalline β-Ga_2O_3 bulks, which have been successfully grown by the Czochralski method,[58–60] edge-defined film-fed growth (EFG),[61, 62] and floating zone (FZ) method.[50] The β-Ga_2O_3 substrates used in this study are prepared from the Czochralski method grown bulk in the Leibniz-Institute for Crystal Growth (IKZ). These substrates are single crystals and defect free. More specifically, they have no twin domain or stacking fault, and therefore provide ideal surfaces for homoepitaxy. In chapter 4, the study on β-Ga_2O_3 thermal expansion will be given. In chapter 5, we talk about its homoepitaxy in MBE, and use *in-situ* characterization tools to analyze its growth mode.

3 Growth and characterization methods

This chapter gives an introduction to the plasma-assisted MBE, the synthesis methodology by which all the thin films in this thesis have been grown, and a variety of *in-situ* analytical tools, which help to characterize the epitaxial films and the bulk crystals.

3.1 Molecular beam epitaxy at PHARAO beamline

After the initial development of MBE for GaAs and GaAs/$Al_xGa_{1-x}As$ growth, as realized by A. Y. Cho and J. R. Arthur in the 1970s,[63] this deposition method has been subsequently evolved to a wider range of materials because of its advantage in the precise control of the growth and the high material purity. The growth of Ga_2O_3 has also been carried out in MBE for thin film deposition.[64–67] Compared with the vapor phase based growth methods, such as plasma-enhanced chemical vapor deposition (PE-CVD), MOCVD, and mist-CVD, MBE is able to control the epitaxial growth in an atomic monolayer scale, since the depositing beam flux in the MBE can be accurately manipulated by the effusion cell temperature. The ultra-high vacuum (UHV) in the growth chamber significantly reduces the density of impurities in the epitaxial crystal, as the diffusing elements are either pumped away or condensed on the cold chamber side walls. The line-of-sight molecular or atomic beam propagation also yields high crystal quality and a relatively easier control of the growth condition, such as the deposition rate and the chemical element ratio.

In this thesis, the MBE system at the PHARAO [**P**DI (Paul-Drude-Institut für Festkörperelektronik) **H**umboldt-Universität **A**rbeitsgruppe **R**öntgenbeugung **a**n **O**berflächen] beamline consists of a load-lock chamber, a preparation chamber, a transfer chamber and a growth chamber in series, and its sketch can be found in appendix A.1.[68] All these chambers are under UHV condition with a base-pressure lower than 10^{-9} mbar. During the layer deposition, the growth chamber is kept at low temperature by liquid nitrogen cooling, in order to further reduce the pressure by condensing the molecules, especially H_2O, CO_2, and heavier

hydrocarbons, onto the cold chamber side walls. This UHV environment can sufficiently suppress the incorporation of impurities, which are from the free molecules, into the epitaxial film. The MBE directly provides the essential chemical components for the growth, such as Ga flux and active oxygen atoms instead of $Ga(TM)_3$ (Trimethylgallium) and H_2O in the MOCVD growth of Ga_2O_3. It helps to avoid potential contaminations from the precursors such as carbon and hydrogen.

In the standby condition of the MBE used in this study, the gallium is kept in liquid phase at 523 K in the pyrolytic boron nitride crucible of the hot-lip effusion cell. The metal beam flux was calibrated by the beam equivalent pressure (BEP) as measured by an ion gauge filament positioned in front of the substrate. A shutter is in front of the crucible to switch on/off the Ga flux. A radio-frequency (RF) plasma cavity equipped with a mass-flow controller (MFC) is used to provide radical oxygen. Within the growth, the substrate was indium bonded on the substrate holder and heated by a SiC made heater controlling the on-site temperature from 298 to 1473 K.

This MBE instrument is combined with the six-circle diffractometer at the dedicated PHARAO beamline U125/2-KMC, Berliner Elektronenspeicherring Gesellschaft für Synchrotronstrahlung II (BESSY II), Helmholtz-Zentrum Berlin (HZB). The top view of the MBE with part of the diffractometer is sketched in figure. 3.1.

3.2 *In-situ* analytical methodologies

Literally the Latin phrase *in-situ* means “in positions” or “on site”. Here in experimental physics, it refers to a typical methodology for data collection and sample manipulation without any exposure to the external condition. In our *in-situ* analytical experiments, the sample is isolated from atmosphere by the UHV condition in the growth chamber, and the data sets are collected during either the epitaxial growth or the change of an experimental parameter, such as sample temperature. Therefore, some of the *in-situ* characterizations used in this thesis are also called “*in-vivo*”, which is however different from the definition by the biologists, and means on-site measurement throughout the ongoing or proceeding experiment.

The *in-situ* (or *in-vivo*) analytical tools used in this thesis are synchrotron-based HRXRD and RHEED, as they are very sensitive to structural information of the sample. The UHV condition in the growth chamber provides an ideal

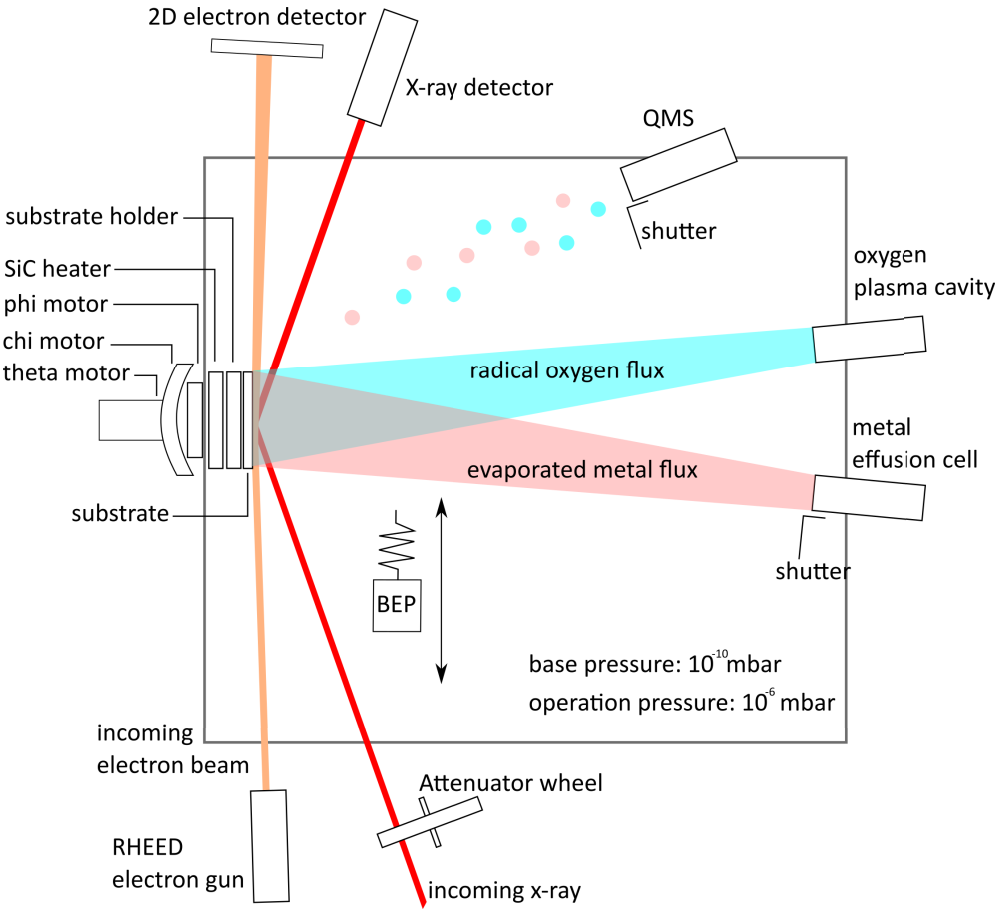

Figure 3.1 Top view schematic of the MBE growth chamber with different *in-situ* characterization tools. The metal flux from the effusion cell and the radical oxygen flux from the plasma cavity react on the substrate surface at a given temperature by the substrate heater. The *in-situ* RHEED and HRXRD are performed with the motion of the motors attached to the six-circle diffractometer. The meaning of the different motors (degrees of freedom) will be explained in the XRD setup section.

environment for the use of RHEED, since electron beams require high vacuum to reduce the collision possibility with the gas molecules in chamber, which can strongly disturb the measurement and even oxidize the RHEED filament. The *in-situ* synchrotron-based HRXRD uses a very intensive x-ray beam (around 10^{10} counts per second), so it can probe the ultra thin films (in scale of monolayers) at initial steps of MBE growth with a proper signal to noise ratio. It also fits well with the low deposition rate of MBE, which can reach even below 1 Å/min. Such an extremely low growth rate enables a very precise control of the film thickness and therefore leaves the *in-situ* HRXRD enough time to acquire the real-time structure information of the monolayers during the growth. The quadrupole mass spectrometry (QMS) helps to monitor the impurities in the vacuum of the growth chamber and determines the desorbing species from the substrate during

the growth based on their mass-to-charge ratio.

3.2.1 Synchrotron-based HRXRD

Generation of x-rays at synchrotron light source

Here the hard x-rays are considered as electromagnetic (EM) waves rather than particles with the wavelength below 2.48 Å, in other words the corresponding photon energy is larger than 5 keV. This wavelength is in the range of the inter-atom distances, therefore perfectly fits to probe the lattice parameters and strains in a semiconductor crystal. Compared with laboratory Cu-Kα source, the synchrotron light source is orders of magnitude more brilliant. In a synchrotron facility, bunches of electrons are confined in an approximately circular shaped vacuum loop by strong magnetic fields. Inside the loop, electrons are accelerated approaching the speed of light and maintained at a constant energy, e.g. the energy is 1.7 GeV at BESSY II, Berlin.

When the charged particles are forced into a curved path by the magnetic field, EM waves are generated. In a storage ring, the accelerated electrons are bended by strong magnetic fields, and therefore generate bremsstrahlung radiations. There are several devices generating these strong magnetic fields such as bending magnet, wiggler, and undulator. In the straight segments of the ring, either a wiggler or an undulator is mounted in order to generate very brilliant x-rays, which has higher efficiency than the bending magnets. The x-rays are emitted along the average trajectory of the electron bunch in the plane of the ring and in a cone shape, as plotted in figure 3.2.

Compared with a wiggler, an undulator forces the traveling electrons oscillating in a much smaller amplitude, therefore the x-rays emitted from each oscillation interfere coherently making the radiation more monochromatic at a fundamental wavelength [figure 3.2 (b)]. In a wiggler, because of the large electron oscillation amplitude, the emitted photons are incoherently added up giving a wider and continuous spectrum [figure 3.2 (a)]. Since the oscillation amplitude depends on the magnetic field B, and the dimension of the dipolar magnets, a dimensional parameter K is introduced to distinguish between a wiggler and an undulator, as shown in equation 3.2.1.

$$K = \frac{eB\lambda_u}{2\pi mc} \tag{3.2.1}$$

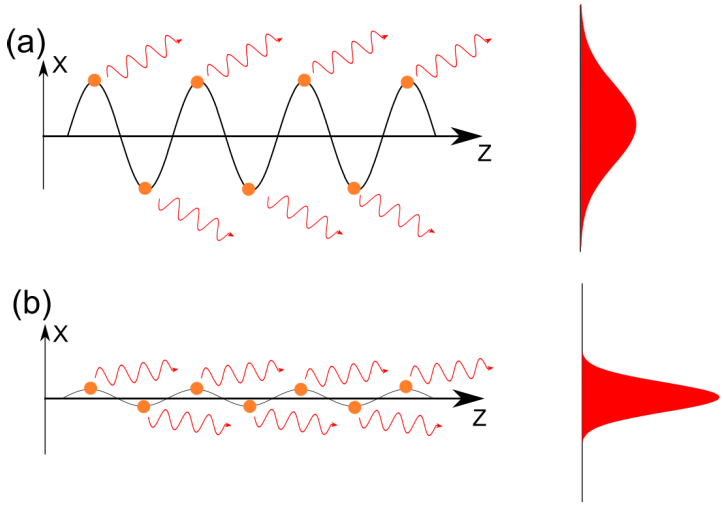

Figure 3.2 (a) The electron trajectory in a wiggler have larger amplitude and the emitted radiation is more incoherent and wider. (b) The amplitude in an undulator is much smaller and gives more coherent x-rays from each oscillation.

in which e is the electron charge, λ_u is the undulator period, m is the electron mass, and c. When $K \leq 1$, it is considered as an undulator, and for $K > 1$ it is treated as a wiggler. The divergence of the radiation is asymmetric in vertical and horizontal directions, since the large horizontal divergence of the electron bunches also contribute to the radiation. Normally, a crystal monochromator is applied to select the desired wavelength from the incoming beam based on Bragg's law

$$2dsin(\theta) = \lambda \tag{3.2.2}$$

in which d is lattice spacing, θ is the Bragg angle, and λ is the x-ray wavelength. The crystal is usually made of very high quality crystals in order to preserve the small divergence of the x-ray. In this thesis, the U-125/2-KMC beamline uses a double crystal monochromator made of (111)-oriented silicon crystal to define the x-ray wavelength with an energy resolution of 10^{-4}.

Symmetric and asymmetric high resolution x-ray diffraction

When a high energy photon impinges onto an atom, in respect of energy, it can be scattered either elastically or inelastically. The inelastic scattering can be used for chemical composition analysis by performing Auger electron spectroscopy (AES) and x-ray fluorescence (XRF). In an elastic scattering event, the x-rays

lose no energy after the scattering but differs in the propagating direction. In this case the incoming beam vector k_i has the same magnitude as the scattered beam vector k_f as $|k_i| = |k_f| = 2\pi/\lambda$, in which λ is the x-ray wavelength. The direction changes from k_i to k_f and can be attributed to a scattering vector q, which starts from the end of k_i to the end of k_f, as described in equation 3.2.3.

$$q = k_f - k_i \tag{3.2.3}$$

Since it is an elastic scattering situation, the scattering vector is only related to the directions of k_i and k_f. Therefore, by adjusting these two vectors with respect to the crystal, the end point of vector q can navigate in a sphere region in the reciprocal space, namely an Ewald sphere with a radius of $r = 2|k_i|$. However, the accessible area is limited by the diffractometer geometry when only reflection from the substrate surface is considered. In reflection, the incident angle α_i and the outgoing angle α_f of the x-ray beam with respect to the crystal surface have to be positive, described as $\alpha_i > 0$, and $\alpha_f > 0$. In such a reflection geometry, only half of the Ewald sphere can be reached by the scattering vector q. If the diffracted beam k_f lies in the same plane with the incident beam k_i and crystal normal n, the accessible planar area in the reciprocal space can be represented as the green region in figure 3.3 (a). However, it is impossible to probe the yellow areas in this geometry, since it is in a transmission geometry where $\alpha_i \times \alpha_f \leq 0$. In the accessible area, the Bragg condition as described in equation 3.2.2 is fulfilled when the momentum transfer q between incoming and diffracted x-rays coincide with a reciprocal lattice vector.

It is observed that some of the diffraction peaks predicted by Bragg's law can not be probed, e.g. α-Al_2O_3 (002) and (004). This is because of the selection rules based on the calculation of the structure factors. The intensity of the diffracted beam is proportional to the square of the structure factor, and some of the structure factors are calculated to be zero. The structure factor can be considered as the Fourier transform of the electron density for one unit cell, and will be talked in section 6.1.[69]

After a precise adjustment to the diffraction condition, several scans can be performed in order to probe different properties of the crystal. If q scans through the reciprocal lattice in a radial direction, by changing α_i and α_f by exactly the same amount, it is called an ω-2θ scan, where ω is equal to the incident angle α_i, θ is the Bragg angle, and 2θ is the angle between k_i and k_f. When the

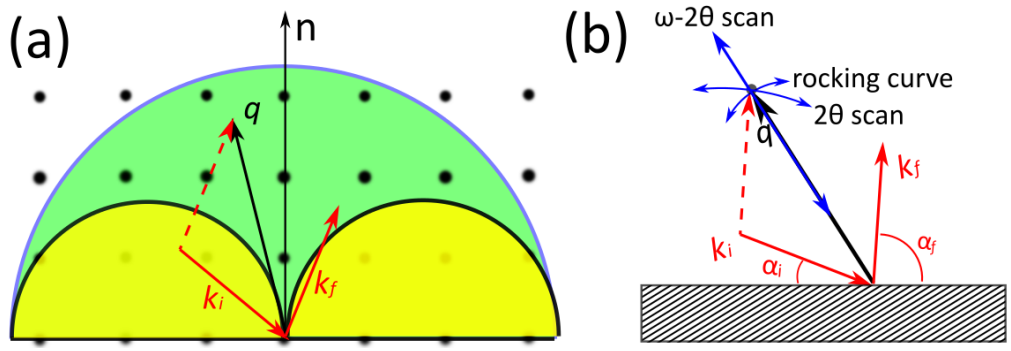

Figure 3.3 (a) In a coplanar diffraction, the measurable area (in green color) in the reciprocal space is a semi-sphere with $2|k_i|$ radius, except for the transmission cases (in yellow). (b) Three scan paths are usually used in the geometry as described in (a).

reciprocal lattice is along the crystal surface normal *n* from the origin, such a radial scan is called a symmetric ω-2θ scan. In this case the diffraction plane is the surface plane, and ω, α_i, and α_f have the same value as the Bragg angle θ. If the reciprocal lattice is not on the surface normal *n*, in which case the diffraction plane is tilted from the surface by a certain angle φ, the ω-2θ scan is asymmetric, as shown in figure 3.3 (b). In such a geometry, the incident beam angle is $\omega = \alpha_i = \theta \pm \varphi$ ($\varphi < \theta$), and the exit angle is $\alpha_f = 2\theta$ - ω. The diffraction in radial direction reflects the lattice spacing, whereas the symmetric scan is sensitive to the strain or deformation of the basal planes, and an asymmetric scan is sensitive to the related inclined planes. Therefore, the out-of-plane strain can be probed by the symmetric scan, while the in-plane strain can be reflected by the asymmetric scan together with the out-of-plane strain. If the scattering vector q is kept at a constant absolute value by maintaining 2θ, but varying α_i and α_f, the reciprocal space is scanned in the angular direction. When α_i moves only back and forth by the same amount α_f moves in the reversal direction keeping the absolute value of q constant, it is called a rocking scan, which reflects the crystal imperfections in the plane.

Grazing incidence diffraction

Another commonly used geometry in the synchrotron-based HRXRD is the grazing incidence diffraction (GID), which has been applied to determine the crystallographic relationships between the thin film and the bulk substrate and to investigate the surface reconstruction. This method is only sensitive to a limited depth from the surface since the totally externally reflected EM waves are evanescent and can only penetrate a few nanometers when the incidence angle is

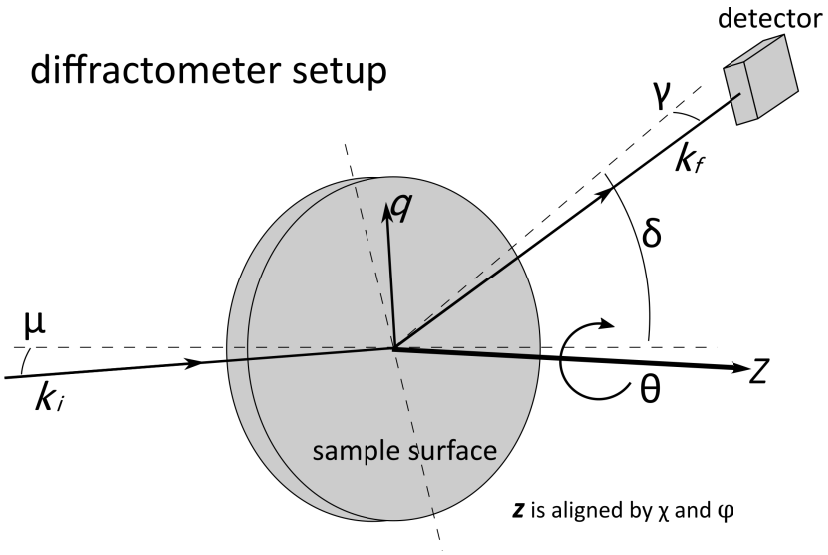

Figure 3.4 Sketch of the grazing incidence diffraction experiment in a six-circle diffractometer of the PHARAO beamline at BESSY II synchrotron facility.

below the critical angle of the material, e.g. 0.23° for sapphire at 10 keV. This geometry combines the Bragg condition and the total external reflection from the crystal surface, allowing to probe the in-plane parameters.

The sketch of this geometry at the PHARAO beamline is given in figure 3.4. The sample is vertically mounted on the diffractometer, as well in the growth chamber. The diffractometer has six degrees of rotational freedom including μ, γ, δ, θ, ϕ, and χ. Hereby μ is the angle between the incident beam k_i and the horizontally rotated entire diffractometer, which defines the incident angle of the x-rays onto the wafer. The detector arm on the diffractometer rotates pointing at the center of the wafer, in both horizontal and vertical directions, and these angles are γ and δ respectively. The sample surface normal is adjusted by the sample tilting χ and the sample rotating ϕ, in order to align it parallel with the rotation axis of θ and avoid wobbling of the sample. Both χ and ϕ are sitting on θ, therefore after the alignment, the sample is rotating only by θ. In this geometry, the *plane of incidence* is defined by the incident beam k_i and the surface normal vector *n*, while *scattering plane* contains k_i and k_f.

In this experiment, the diffracted beam intensity is recorded by a point detector mounted on a movable arm. Since the direction of incoming x-ray beam is fixed at a beamline, therefore the incident beam direction has to be manipulated by the adjustment of the wafer orientation.

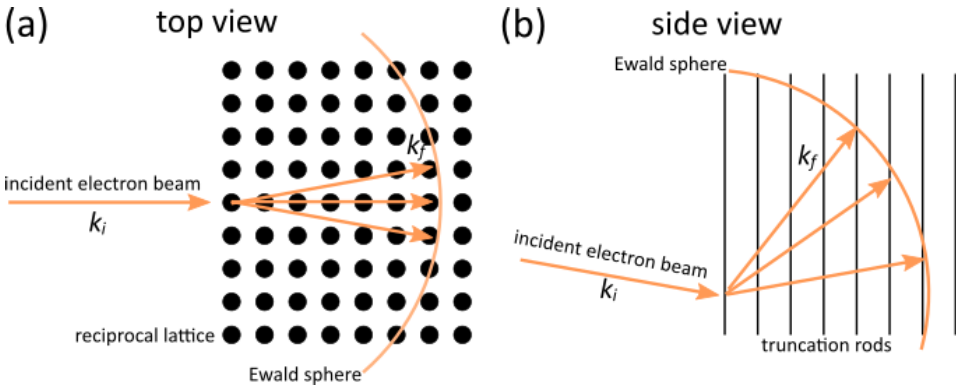

Figure 3.5 Electron diffraction geometry in RHEED for thin film. Topview (a) and side (b) of the reciprocal lattices of the thin film interact with the electron wave vector. Intersection of the reciprocal lattice and the Ewald sphere are presented as high intensity on the fluorescent screen.

3.2.2 Reflection high-energy electron diffraction

The reflection high-energy electron diffraction (RHEED) applies a collimated high-energy electron beam to characterize the structures of crystal with a high surface sensitivity. The electron beam impinges on the sample surface at a defined glancing angle and generates forward scattered diffraction patterns. The incident angle typically ranges between 0.5 and 2.5°, therefore the surface-normal component of the incident wave vector k_i is very small, and determines a shallow penetration depth into the material. So, this analytical tool is very surface sensitive. The projection of the electron beam at the sample surface is several millimeters along the beam direction due to the small incidence angle, therefore the RHEED result is a sum in this probed area.

The diffraction geometry is sketched in figure 3.5. In (a), when the momentum transfer q between the diffracted wave vector k_f and the incoming wave vector k_i, as described by equation 3.2.4, intersects with the reciprocal lattice, constructive interference takes place. In an elastic scattering condition, k_i has the same amplitude as k_f.

$$q = k_i - k_f \tag{3.2.4}$$

Since RHEED is very surface-sensitive, the sampled volume can be approximated as a two-dimensional layer. Its reciprocal lattice then shows one-dimensional truncation rods perpendicular to the sample surface, as sketched in figure 3.5 (b). These rods are probed streaks in the RHEED pattern, as shown in figure 3.6 (a).

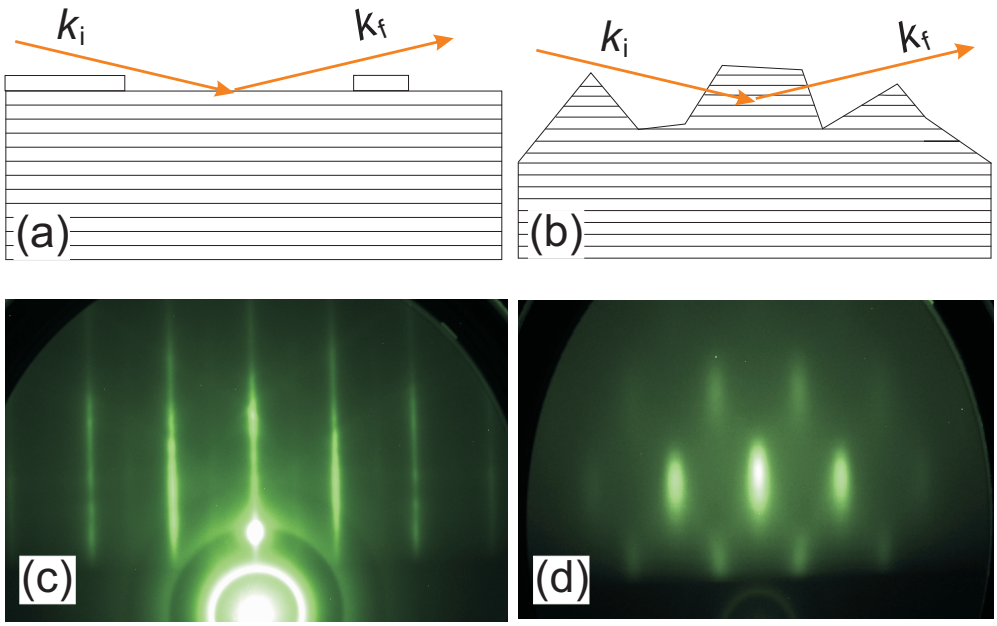

Figure 3.6 (a) Schematic of a flat (100)-oriented β-Ga_2O_3 substrate after growth (top), and its RHEED pattern along the [101] direction (down). (b) the sketch of a rough (111)-oriented In_2O_3 epitaxial film grown on c-plane sapphire substrate (top), and its RHEED pattern along the sapphire [100] direction.

The fresh split (100)-oriented β-Ga_2O_3 substrate has an atomically flat surface, its RHEED pattern presents sharp RHEED streaks in the vertical direction. As for three-dimensional (3D) islands on a rough surface, the electron beam at low incident angle goes through the islands forming transmission diffraction, and therefore shows an array of reciprocal points. For example, the rough (111)-oriented In_2O_3 grown on c-plane sapphire shows dots instead of streaks in its RHEED pattern. Since the RHEED pattern is very surface sensitive, here the RHEED pattern is used to monitor the morphology and crystallinity at the top-most layers during the growth.

The specular reflection intensity shows periodic change as plotted with the growth time, when the growth is in a two-dimensional (2D) layer-by-layer (Frank-van der Merwe growth) mode. The mechanism of the RHEED oscillation is related to the growth process of the layer-by-layer mode that the next layer only starts to form until the previous layer is essentially completed. Therefore, there is a periodic change of surface morphology (and roughness), and these changes cause the intensity modification in the specular spot. This phenomenon has been explained in several theoretical models, such as birth-death models,[70, 71] kinematical model,[72] and several dynamical scattering methods.[73–76] In this study, the birth-death mode is applied to simulate the RHEED oscillation, since

it directly describes the growth process.

In the experiments, a RHEED system requires a UHV work condition, and is typically installed in MBE systems, since gas molecules in the atmosphere scatter electrons and damage the electron emission filament during operation. It also has a good compatibility with the UHV chamber compared with other diffraction methods like low-energy electron diffraction and transmission electron diffraction. The RHEED system at the PHARAO beamline consists of a tungsten electron gun, a magnetic focus system, a phosphor fluorescent screen, and a charge-coupled device (CCD) camera. The low divergent electron beam emitted from the tungsten filament was accelerated to a kinetic energy of 20 keV, and then was focused on the sample surface with a focal length of around 500 mm. At such a glancing angle, the electron beam is very surface sensitive, and the depth is only a few atomic layers. The diffracted electron beams then are converted into visible light on the fluorescent screen and recorded by the CCD camera. According to the de Broglie equation, the matter wavelength of the E_{kin} = 20 keV electron is 0.086 Å, which is much smaller than the lattice constants of the group-III sesquioxides, and therefore fulfills the resolution requirements.

3.2.3 Quadrupole mass spectroscopy

QMS is a specific type of mass spectroscopy consisting of four parallel cylindrical rods, named quadrupole, which filter the incoming ions depending on the mass-to-charge ratio. QMS was applied for the residual gas analysis in the growth chamber and also the desorbing species from the substrate during the growth. As depicted in figure 3.1, the QMS aperture is mounted directly towards the substrate in order to make it sensitive to the material coming from the substrate. However, since the quadrupole is too far (approximately 500 mm) from the substrate, this device is not sensitive enough to probe the desorbing metal ions during the growth. Therefore, this device is mainly used to analyze the gases and contaminations in the growth chamber before and after the growth.

4 Thermal expansion of β-Ga_2O_3

This chapter reports the thermal expansion of single-crystalline β-Ga_2O_3 from RT to 1200 K. The lattice parameter characterization process is introduced, and the crystal structure of β-Ga_2O_3 is presented again in order to bridge relationship between the measured lattice spacing and the corresponding lattice parameter. The measured thermal expansion behaviour of β-Ga_2O_3 is quantitatively interpreted by the Einstein Model. In this study, the coefficients of thermal expansion (CTE) derived from the fittings are in good agreement with the previous investigations.

4.1 Motivation

β-Ga_2O_3 is a very promising candidate in various applications, such as solar-blind deep UV photodetectors and high power electronics, as introduced in chapter 2. However, such an interesting material, which has drawn a lot of attention in research and applications, has a limited number of publications concerning its thermal expansion property. In 2008 Víllora *et al.* reported the change of lattice parameters *a*, *b*, and *c* as a function of temperature from 5 to 293 K, and recently Orlandi *et al.* published the crystal thermal expansion from 300 to 700 K.[77, 78] The CTEs in three different axes as reported from these two publications are listed in table 4.1. However, the CTEs of β-Ga_2O_3 above 700 K and their dependence on temperature are not investigated yet.

In heteroepitaxy of β-Ga_2O_3, the substrate temperature needs to be kept at 973 K in MBE, 1073 K in MOCVD and 923 K in PLD.[25, 45, 79] In semiconductor industry, the furnace annealing process is important in improving the electrical properties, and it as well requires a rather high temperature.[80] Bulk β-Ga_2O_3 has been reported to transfer into α-Ga_2O_3 at 2000 K with 30 GPa pressure.[81] All these temperatures are higher than 700 K, however the thermal expansion behaviour of β-Ga_2O_3 is still unknown in this range, where the expansion of the crystal is expected to play an important role. For instance, the lattice mismatch between the heteroepitaxial layer and the substrate underneath

Table 4.1 Previous investigations on the CTEs of β-Ga_2O_3.

Temperature [K]	**CTEs [10^{-6}]**		
	α_a	α_b	α_c
5 to 293	1.8	4.2	4.2
300 to 700	1.54	3.37	3.15

is important to the epitaxial growth, since it generates stress at the interface, which therefore influences the surface energy and might induce misfit dislocations in the growing layer.[82] In addition to that, the experimental results of the thermal expansion behaviour can also help to explain different phonon modes in β-Ga_2O_3.[83] Therefore it is highly interesting and practical to precisely study the thermal expansion of β-Ga_2O_3 in a higher temperature range.

In this chapter, our research aims on a comprehensive study of the β-Ga_2O_3 thermal expansion properties to an extended temperature range. In the experiments, the lattice spacings were probed precisely by *in-situ* synchrotron-based HRXRD from 298 to 1200 K.

4.2 Thermal expansion of β-Ga_2O_3 as probed by HRXRD

The experiments were carried out at the MBE endstation of the PHARAO beamline. The lattice spacings were measured by synchrotron-based 2θ-ω HRXRD in the out-of-plane direction and GID in the in-plane directions. During the measurement, the SiC made substrate heater in the MBE is able to heat the sample from 298 K to around 1473 K in ultra high vacuum of about 10^{-10} mbar. Since the indium bonding becomes very unstable above 1200 K, the upper temperature limit is set to 1200 K. The x-ray energy used in the experiment is 10 keV with an energy resolution ΔE/E of about 10^{-4}, which yields high accuracy in the measured lattice spacing. In order to determine the true temperature of the sampled area precisely, a (111)-oriented silicon wafer was used to calibrate the thermocouple, since its lattice parameters and CTEs are already well known.[84] Both the silicon wafer and the β-Ga_2O_3 sample were mounted on the substrate holders by indium bonding, which helps to avoid external stress and increase the thermal conductivity. The calibration procedure yields a temperature uncertainty of about 10 K above and below the on-site temperature.

The (100)-oriented β-Ga_2O_3 wafers have a size of 2.5×5 mm^2, and are prepared from the bulk crystal grown by the Czochralski method at Leibniz-Institute

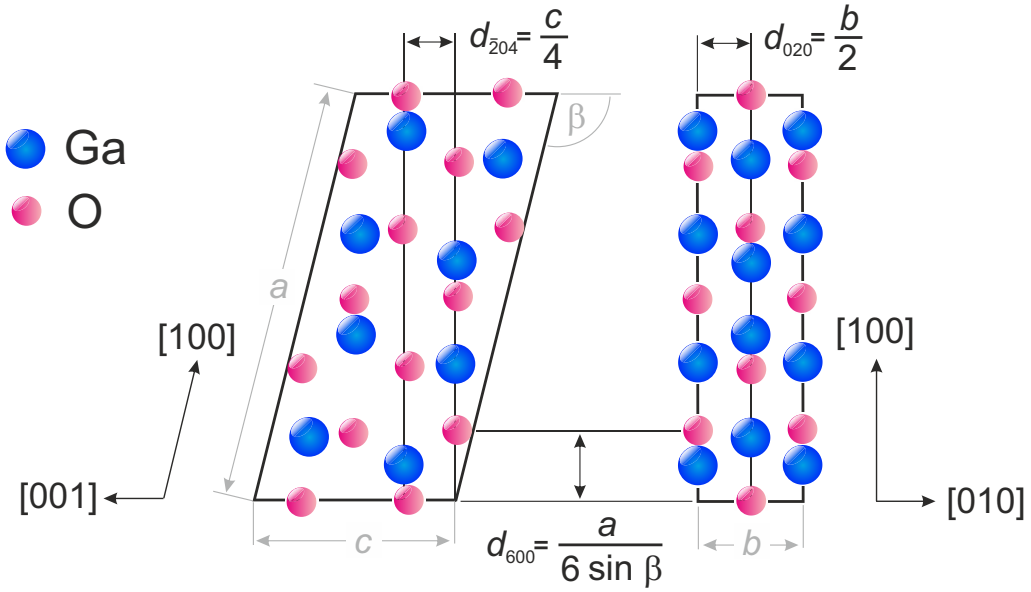

Figure 4.1 Crystal structure of β-Ga_2O_3 viewed in [010] (left) and [001] directions (right). (020), ($\bar{2}$04) and (600) planes were measured by XRD to obtain the lattice plane distance as a function of the substrate temperature.

for Crystal Growth (IKZ).[58–60] The HRTEM results have proved that these wafers are free of defects. The wafers were mounted on the substrate holder by indium bonding, and the substrate holders are made of inconel (an austenitic nickel-chromium-based superalloy).

After the preparation for HRXRD measurement, we have investigated the thermal expansion of the (600), (020) and ($\bar{2}$04) spacings in β-Ga_2O_3, as sketched in figure 4.1, from 298 K to 1200 K. If the angles between three axes of the unit cell are assumed to be constant (α=90°, β=103.85°, γ=90°) during the lattice expansion, on the basis of the measured planes, therefore the lattice parameters a, b, and c can be calculated according to a=6×$d_{(600)}$/sin(103.85°), b=2×$d_{(020)}$, and c=4×$d_{(\bar{2}04)}$/sin(89.9°). Figure 4.2 presents the HRXRD and GID measurements along [100], [010], and [$\bar{1}$02] directions of the reciprocal space. Among these diffraction peaks, we chose (600), (020), and ($\bar{2}$04) (as indicated by the blue frames in figure 4.2) to probe the plane spacing, since, within the physical limit of the six-circle diffractometer, these diffraction peaks have the largest absolute values of the reciprocal vector in the respective directions, and therefore yield a relatively smaller measurement error of the lattice parameter.

As mentioned, the monoclinic angle β is treated as a constant in this study, however it has been reported to change with temperature.[77] The β-Ga_2O_3 powder specimen was found having a slight increase of the monoclinic angle β by 0.01° as the temperature changed from 300 to 700 K. If the bulk substrate are

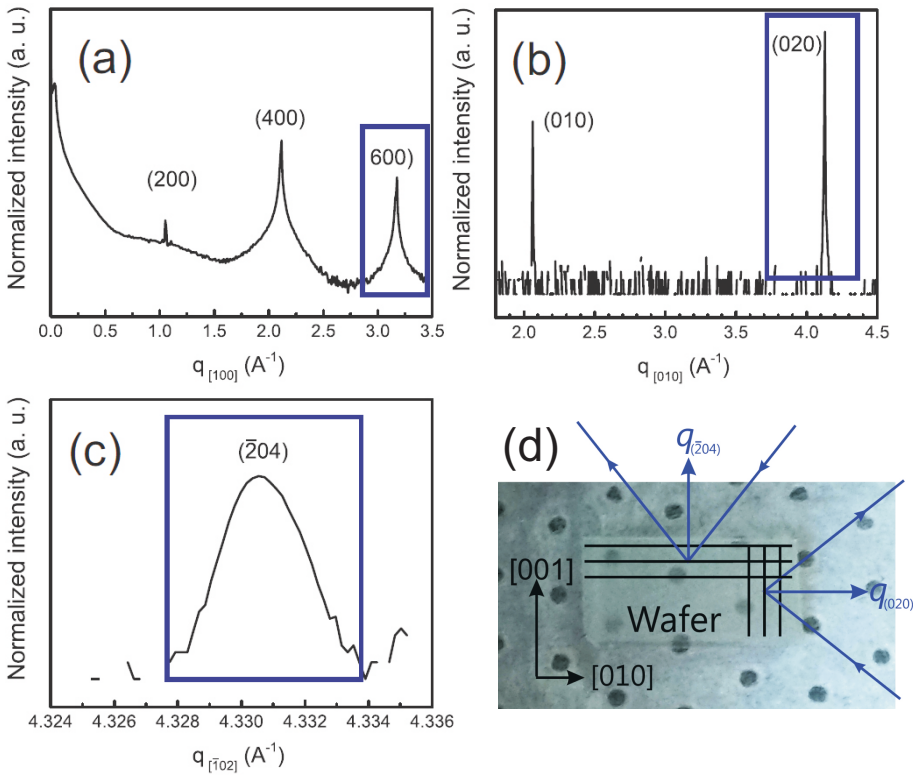

Figure 4.2 The HRXRD intensity profiles along the [100], [010], and [$\bar{1}$02] directions are plotted in (a), (b), and (c), respectively. The blue frames indicate the diffraction peaks which were used to monitor the thermal expansion in this direction.(d) Photo of the (100)-oriented single-crystalline β-Ga_2O_3 on a tissue paper. Two in-plane diffractions used in the determination of CTEs are sketched.

assumed to behave similar as the powder specimen in both the overlapped temperature range and the temperature from 700 to 1200 K, angle β will increase by about 0.02°. However, such a change of β has a rather small influence on the thermal expansion calculation (less than 5 % of CTE), and therefore can thus be neglected. According to this assumption, we treat β as a constant value during the measurement.

4.3 Analysis of the anisotropic thermal expansion

The lattice parameters a, b, and c are plotted as a function of substrate temperature T in figure 4.3 (a-c), and the red curves are the fittings based on the Einstein model. As a deviation of the red curves over temperature, the respective CTEs (α_a, α_b and α_c) are plotted together with the constant values of CTEs for powder specimen, which are also listed in table 4.1.[77, 78] It is found in the previous studies that the crystal expands anisotropically with ratio $2\alpha_a \approx \alpha_b \approx \alpha_c$, and

our findings are in good agreement with this anisotropic feature and ratio.

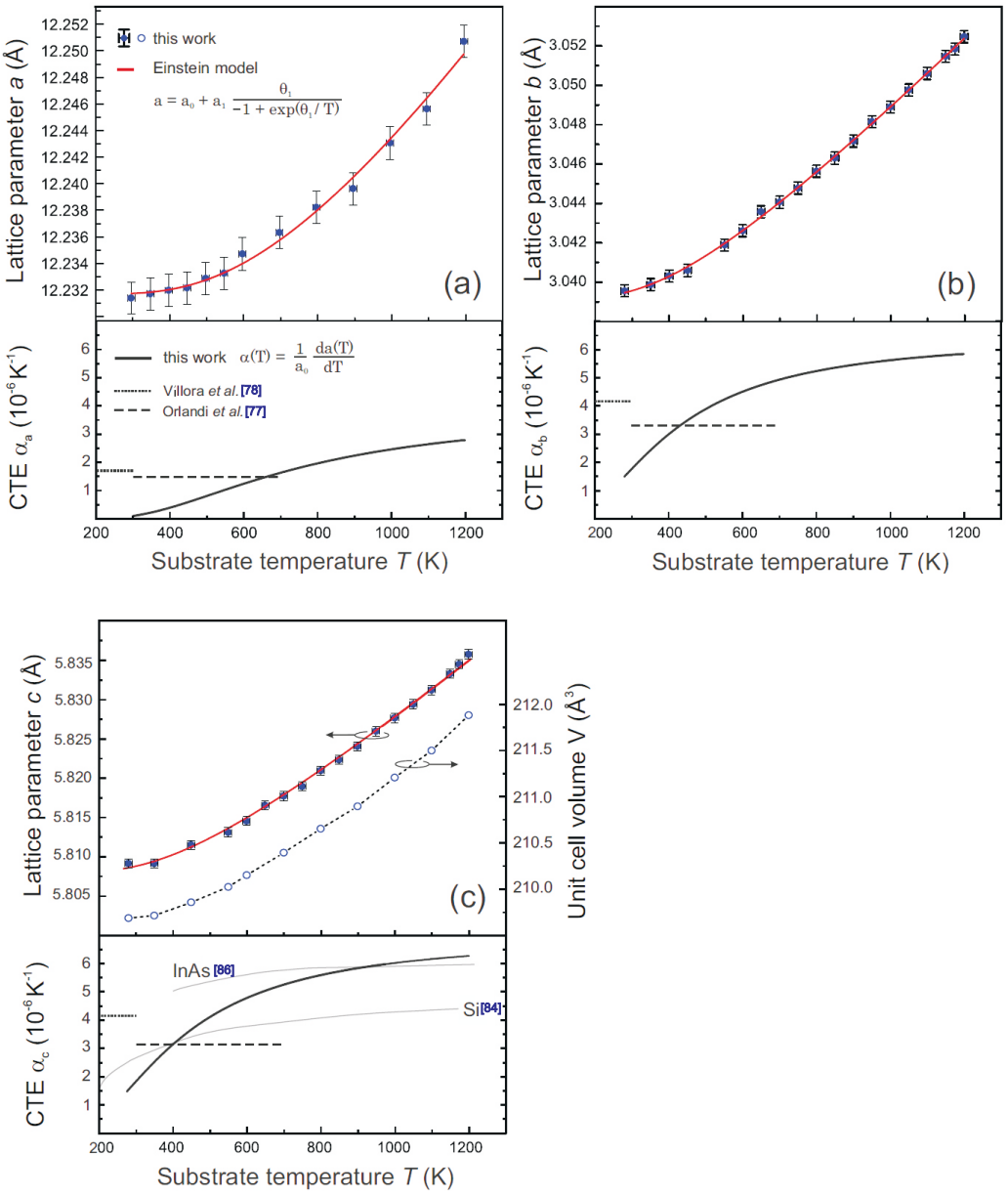

Figure 4.3 (a-c) measured lattice parameters a, b, and c and resulting unit cell volume V as function of temperature T. Red curves show numerical fits applying the Einstein model[85] of thermal expansion. The CTEs α_i along the three crystallographic directions [100], [010] and [001] of the monoclinic unit cell are the derivatives of the temperature dependent lattice parameters. They are plotted at the bottom of each figure together with data for powder β-Ga_2O_3[77, 78]. For illustrative purposes the isotropic values of α for cubic InAs[86] and Si[84] are reproduced in (c).

The definition of CTE is given by the following equation according to the

International Organization for Standardization (ISO),

$$\alpha\left(T\right) = \frac{1}{a_{RT}} \frac{da\left(T\right)}{dT} \tag{4.3.1}$$

whereby a_{RT} refers to the lattice parameter at 298 K, and $\frac{da(T)}{dT}$ is the differential lattice parameter over temperature. By neglecting now the influence of the phonon dispersion (i.e., the high temperature regime), $\alpha(T)$ can be calculated according to the Grüneisen equation [87]:

$$\alpha\left(T\right) = \frac{1}{3} \kappa \, \gamma \, C_v\left(T\right) \tag{4.3.2}$$

Here, the Grüneisen constant γ is determined by the volume derivatives of the sound velocities in all directions, and κ is the harmonic compressibility. In a simple model, both quantities can be considered as constants, independent of temperature *T*. Therefore in equation 4.3.2 $\alpha(T)$ is only proportional to $C_v(T)$, the specific heat per volume. Therefore, we need to calculate the specific heat as a function of temperature. Here, the Einstein model relates the specific heat of a solid to its phonons, all of the same frequency but with different occupation probability at various temperatures. With the Einstein temperature θ_E it yields for the specific heat:

$$C_v\left(T\right) \propto \left(\frac{\theta_E}{T}\right)^2 \frac{e^{\theta_E/T}}{\left(-1 + e^{\theta_E/T}\right)^2} \tag{4.3.3}$$

In some cases, e.g. if the CTE is partially negative, a single Einstein-term becomes insufficient and has to be replaced by a summation over *m* several terms:

$$\alpha(T) = \frac{1}{a_{RT}} \sum_{k=1}^{m} a_k \left(\frac{\theta_k}{T}\right)^2 \frac{e^{\theta_k/T}}{\left(-1 + e^{\theta_k/T}\right)^2} \tag{4.3.4}$$

Based on that the lattice parameter can be finally obtained by integration.

$$a(T) = a_0 + \sum_{k=1}^{m} a_k \frac{\theta_k}{-1 + e^{\theta_k/T}} \tag{4.3.5}$$

In this equation, a_0 is the corresponding lattice parameter at room temperature. As apparently in figure 4.3 (a-c), the simulated curves (the red line) of lattice parameters as a function of the temperature, which bases on the Einstein model (m = 1), agree very well with the discrete data points within the entire temperature window. The respective fitting parameters a_0, a_1, θ_1 for each direction including uncertainties are: [12.2317(3) Å, 4.6(6)$\times 10^{-5}$ Å/K, 2309(240) K] for

T (K)	α_a	α_b	α_c
	(10^{-6} K^{-1})		
RT	0.10	1.68	1.74
600	1.24	4.51	4.79
800	1.97	5.24	5.60
1200	2.78	5.84	6.27

Table 4.2 Coefficients of thermal expansion α_a, α_b and α_c at particular temperatures T for β-Ga_2O_3 bulk as taken from the fitting curves in figure 4.3(a-c). Please note that, according to Eq. 4.3.1, α is proportional to the derivative $\frac{da(T)}{dT}$.

[100] direction, [3.0392(1) Å, 1.94(4)10$\times^{-5}$ Å/K, 1251(44) K] for [010] direction, and [5.8096(2) Å, 4.5(1)$\times 10^{-5}$ Å/K, 1477(59) K] for [001] direction.

Since the simulations support very well with the measured lattice parameters, the CTEs can be calculated from the derivative of the thermal expansion. At the bottom of figure 4.3 (a-c), the CTEs of lattice parameter *a*, *b*, and *c* are plotted as a function of temperature. One interesting feature is that in the probed window all functions α_a, α_b, and α_c increase with temperature and tend to be saturated as the temperature gradually approaches the high temperature limit close to 1200 K. This is a general saturation effect indicative for fully occupied phonon modes as also observed at, e.g. InAs and Si,[84, 86] as indicated in figure 4.3(c). It clearly shows that α_b and α_c follow a rather similar dependency, however α_a is approximately only half of them. This anisotropic thermal expansion behaviour is in correspondence with measurement of CTEs from 5 to 700 K reported previously. The unit cell volume, as calculated from the measured lattice parameters, also depicts a similar functional dependence in figure 4.3 (c). Table 4.2 gives the numerical CTE values at four particular temperatures (RT, 600 K, 800 K, and 1200 K).

Lattice mismatch in heteroepitaxy

Since the CTEs from RT to 1200 K are already known for β-Ga_2O_3, one application is to calculate the lattice mismatch between heteroepitaxial β-Ga_2O_3 and the substrate at the elevated growth temperature. As for the growth on *c*-plane sapphire substrate, it has been reported that β-Ga_2O_3 thin films are grown in ($\bar{2}01$)-orientation with three-fold in-plane rotational domains.[25, 45] Within those films the {010} planes of β-Ga_2O_3 are parallel with the {100} planes of α-Al_2O_3, therefore the lattice parameter difference between these two sets of

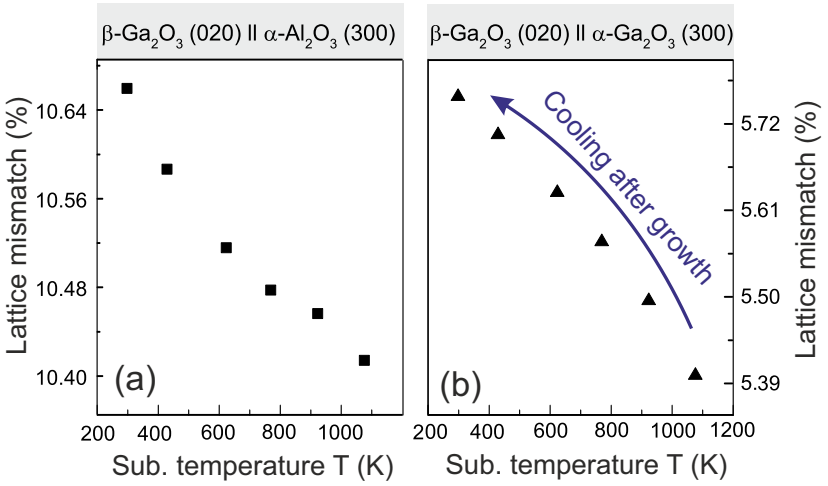

Figure 4.4 In-plane lattice mismatch between β-Ga_2O_3 and α-Al_2O_3 decreases at elevated temperatures (a), similar to the combination β-Ga_2O_3 vs. α-Ga_2O_3.

planes at the interface leads to an in-plane lattice mismatch of around 10.65% at RT. As shown in figure 4.4 (a), when the temperature is increased to the growth temperature of around 975 K, the different temperature dependencies of CTE for β-Ga_2O_3 and α-Al_2O_3 [88] yield a smaller lattice mismatch of about 10.4%. The remaining, however considerably large lattice mismatch acts as key reason for the initial formation of a three-monolayer thin pseudomorphic α-Ga_2O_3 layer before the Ga_2O_3 growth proceeds in the β-phase. In figure 4.4 (b), the lattice mismatch between the β-Ga_2O_3 epitaxial film and the α-Ga_2O_3 [89] buffer layer is plotted as a function of temperature after taking into account both CTEs. At the growth temperature, the lattice mismatch decreases to around 5.4%. As well lattice mismatch will also increase after the growth during the cooling process down to RT. Therefore, it might be important to perform cooling with a rather low rate in order to avoid a fast increase in the lattice mismatch and to prevent the formation of potential defects.

4.4 Summary

In this study, the lattice parameters *a*, *b*, and *c* of single-crystalline monoclinic β-Ga_2O_3 bulk were precisely probed by the out-of-plane HRXRD and the in-plane GID in the temperature range from 298 to 1200 K. The experimental results of β-Ga_2O_3 thermal expansion are interpreted by the Einstein model fittings based on single Einstein-term. It presents that the β-Ga_2O_3 expands anisotropically in different crystal directions, whereby the CTE along *a* is roughly half of the CTEs along *b* and *c*. Exactly this anisotropic feature is also found at lower tem-

perature. The CTEs also show strong dependence on the temperature. In the measured temperature range, the CTEs slowly increase with on-site temperature, and meanwhile the increase rates gradually approach to 0, which is described as a general saturation effect indicative for fully occupied phonon modes. This study helps to predict the lattice mismatch at high growth temperature and provides evidence for an anisotropic behavior within the investigated temperature window.

5 Growth mode evolution of (100)-oriented β-Ga_2O_3 homoepitaxy

This chapter presents a study on the growth mode of (100)-oriented β-Ga_2O_3 homoepitaxy in MBE, and interprets the formation mechanism of the twin domains found in the epitaxial film.

5.1 Motivation

Though β-Ga_2O_3 has drawn considerable attention in various applications, such as high-power electronics and solar-blind UV detectors, the crystal quality of the heteroepitaxial thin film limits its potential in devices to be fulfilled. For example the β-Ga_2O_3 layers grown on sapphire,[25, 45, 90, 91] silicon,[92] MgO,[93] yttria-stabilized zirconia (YSZ),[94] and GaAs[95] are likely to contain rotational domains, and the domain boundaries dramatically reduce the electron mobility in the epitaxial film. Recently large diameter ($\simeq$ 1 inch) β-Ga_2O_3 substrates become available because of the development in the melt growth methods for β-Ga_2O_3, such as Czochralski growth,[58–60] edge-defined film-fed growth,[61, 62] and floating zone method.[50] This is an important precondition for the study in β-Ga_2O_3 homoepitaxy. Compared with heteroepitaxy, there is no lattice mismatch and structure difference in homoepitaxy, therefore it is expected to yield high crystal quality in the epitaxial film.

In β-Ga_2O_3 crystal, the (100) plane is weakly bonded compared with the other planes,[96] so it can be easily split and cracked by itself. The split (100) surface shows an atomically smooth surface without any regular step terrace as proved by AFM,[27] therefore it is considered as an ideal surface for homoepitaxy. Studies in homoepitaxy of (100)-oriented β-Ga_2O_3 by MOCVD have reported the formation of twin domains and stacking faults in the epitaxial film.[97–99] In MOCVD growth these defects can be eliminated by applying (100)-oriented wafers with a miscut angle of 6° towards [001] to achieve a step-flow growth mode.[98] However it requires additional polishing and annealing processes to produce the misoriented substrates. These twin domain boundaries and defects greatly reduce

the electron mobility in the film. Baldini *et al.* have reported a maximum electron mobility of 41 cm^2/Vs at a free carrier concentration of 1×10^{18} for the layer with twin domains,[91] which is much lower than the mobility (130 cm^2/V) in bulk crystal at a similar doping level.[100]

Because of the existence of the twin domains, it becomes highly interesting to understand the formation mechanism of the twin domains in homoepitaxy, and the growth mode behind this phenomenon.

5.2 Preparation of substrates

The (100)-oriented β-Ga_2O_3 substrates are in the size of $5\times5\,mm^2$, and are prepared from the same bulk crystal as used in chapter 4. The high crystal quality of the substrate has been evidenced by small rocking curve FWHM below 50 arcseconds, and the absence of twin domain and stacking fault.[58–60] After a standard cleaning process with acetone and isopropanol solvents in the ultrasonic bath, the substrates were properly split at the non-polar (100) surface termination, the B-plane as shown in figure 2.3.[96] Since (100) is a preferred cleavage plane, its surface appears flat on the atomic scale. After the mechanical splitting, the cleaved piece of (100)-oriented β-Ga_2O_3 with the fresh side up was immediately mounted on a substrate holder by indium bonding, which improves thermal conductivity and thereby effectively avoids external stress induced by thermal expansion.[77] The substrate was degassed in the load-lock chamber at 473 K for 30 min, afterwards it was transferred into the growth chamber, and mounted on the substrate heater.

5.3 Layer-by-layer growth mode

The growth was carried out at the MBE of the PHARAO endstation described in chapter 3. During the growth, the substrate temperature was kept at 973 K, while the gallium cell and the hot-lip temperature were set to 973 and 1123 K, respectively. The plasma cavity was set to 400 W with a constant oxygen flux of 0.6 sccm, the pressure in the growth chamber is around 6×10^{-6} mbar. Based on these parameters, the homoepitaxy was performed at oxygen-rich conditions, and the Ga etching phenomenon can be neglected. *In-situ* analytic tools as synchrotron-based HRXRD and RHEED were used during the growth to investigate the crystal structure and the growth mode evolution.

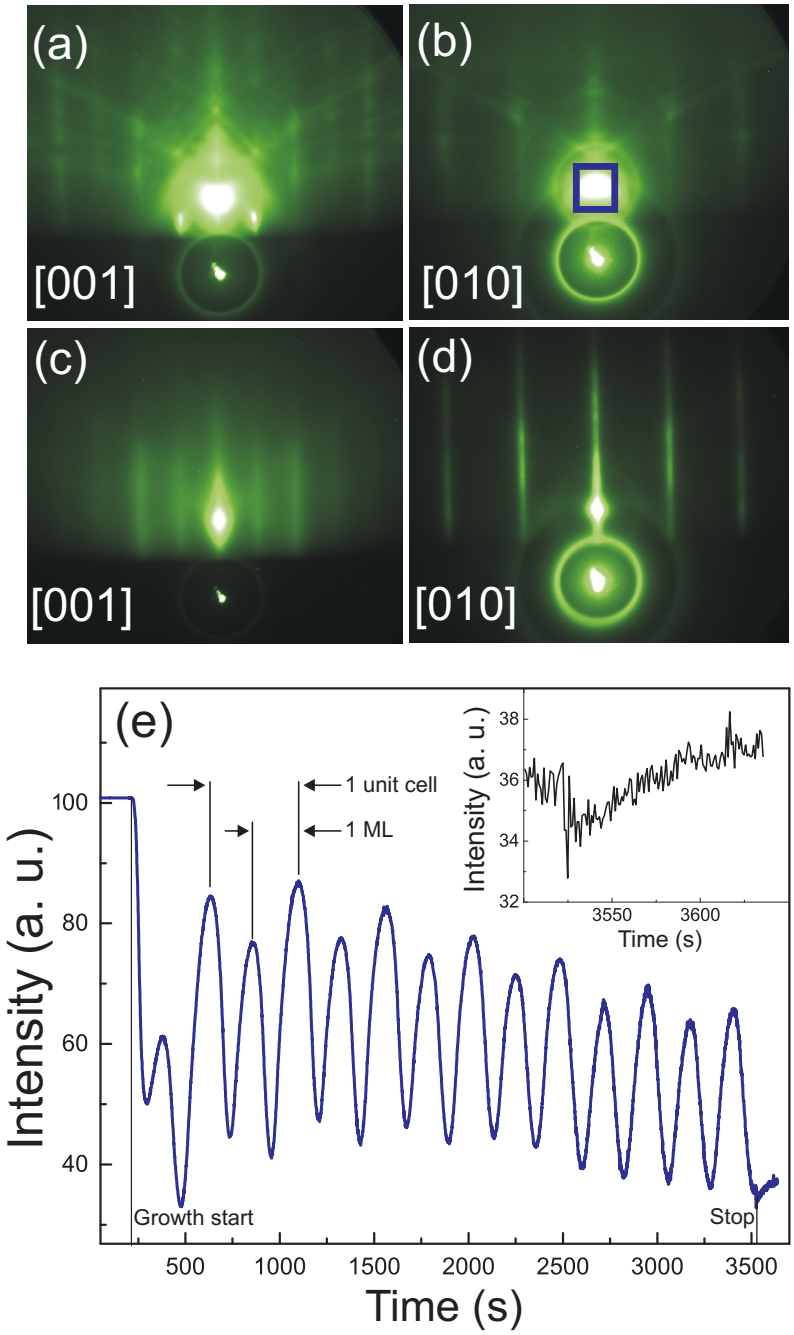

Figure 5.1 RHEED patterns before (a,b) and after (c,d) the growth in the two directions [001] and [010]. The time evolution of the specular intensity (e) as monitored by the integral intensity within the observed rectangular frame in (b) during growth depicts a particular oscillation behaviour on two discrete time scales and thus alternating strong and weak minima and maxima.

The RHEED patterns were recorded before and after the growth, respectively, along [001] and [010] azimuthal directions. Figure 5.1 (a) and (b) depict the RHEED patterns of the prepared substrate surface before growth, in which the surface streaks and the crystal Kikuchi lines can be clearly observed. The integral growth time was 3300 seconds, and the RHEED patterns were recored every 20 seconds. During the growth, the Kikuchi line shown in (b) gradually disappeared and the vertical streaks became more intense and sharper. After the growth, the RHEED patterns in figure 5.1 (c) and (d) show sharp streaks, which can be attributed to an atomically flat surface. These streaks follow the bulk diffraction patterns, and no additional ones emerge during growth, which implies a flat thin film accompanied by the formation of a (1×1) surface reconstruction.

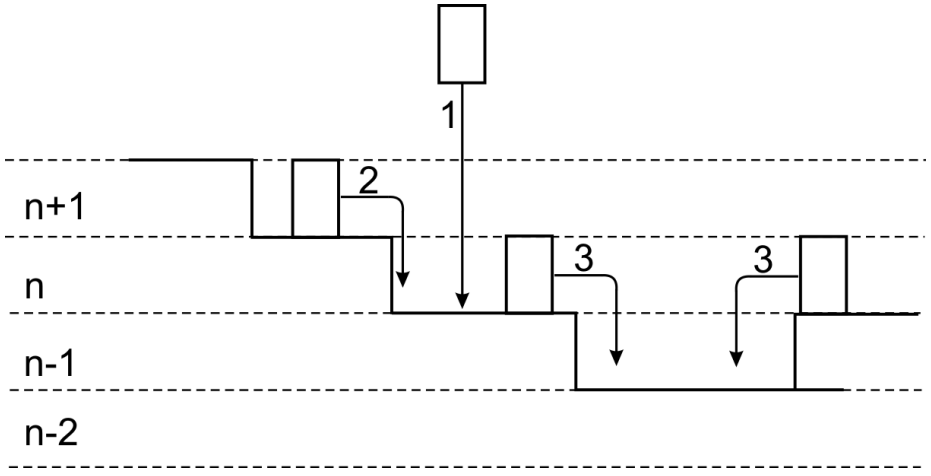

Figure 5.2 Three processes are considered to contribute to the formation of one layer on a low-index surface. Process 1 refers to the direct adhesion on top of layer n-1. Process 2 corresponds to an adatom in layer n + 1 diffusing into layer n. Process 3 corresponds to an adatom leaving layer n and moving to the uncovered sites of layer n-1.[70]

As plotted in figure 5.1 (b), an intensity integration within the blue square framed was performed to monitor the intensity of the specular beam spot during the growth. In figure 5.1 (e), the reflected beam intensity is plotted as a function of the growth time. This plot shows remarkable periodicities in time: an intense maximum is followed by a weaker one and, subsequently, by another more intense one and so on. Such an oscillating behaviour proves the nucleation of sequential, clearly distinguishable steps, suggesting that the deposition can be characterized as a two-dimensional (2D) layer-by-layer growth mode. As described by Cohen *et. al.*, the RHEED oscillation can be interpreted by the birth-death model.[70, 71] In this model, as sketched in figure 5.2, adatoms on the surface are assumed to have a possibility jumping to a lower layer, therefore there are

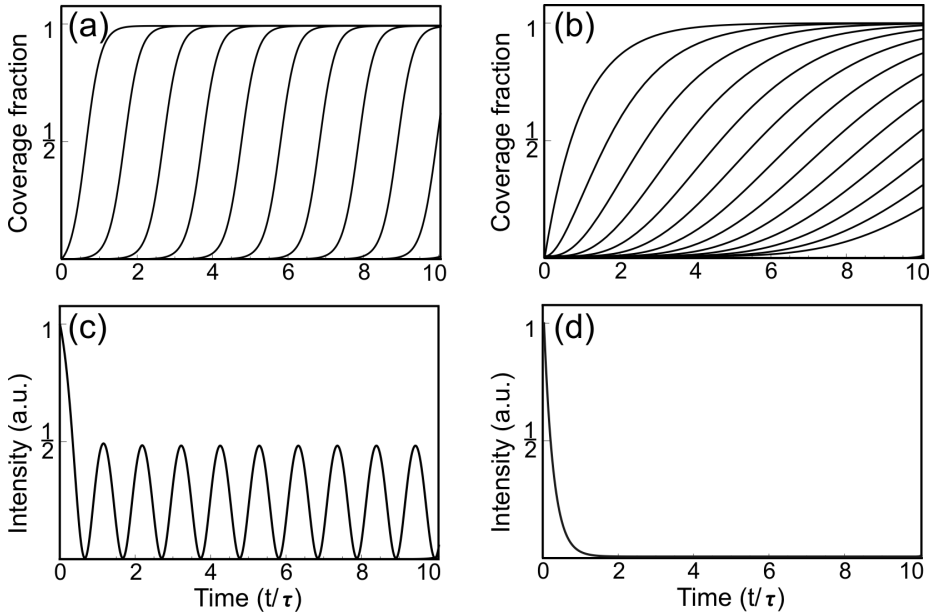

Figure 5.3 Numerical solutions of equation 5.3.1 with k = 50 and 0 are sketched in (a) and (b), whereby the *n*th layer coverage is plotted as a function of t/τ. The amount of interlayer diffusion is governed by the diffusion parameter k. The kinematic diffracted intensity based on equation 5.3.2 shows oscillation when k = 50 (c), while the intensity decreases rapidly to zero when k = 0 (d).

three processes that influence the growth in the *n*th layer: the direct adsorption in layer *n*, the adatoms jumping from layer *n+1* to layer *n*, and the adatoms moving to layer *n-1* from layer *n*. With consideration of these three processes, the net growth rate of layer *n* can be described by the differential equation 5.3.1.[70]

$$\begin{aligned} d\theta_n/d_t =& (1/\tau)(\theta_{n-1} - \theta_n) + k(\theta_{n+1} - \theta_{n+2})(\theta_{n-1} - \theta_n) \\ & - k(\theta_n - \theta_{n+1})(\theta_{n-2} - \theta_{n-1}) \end{aligned} \tag{5.3.1}$$

Here the overall growth rate is $1/\tau$ monolayers per second, θ_n is the layer coverage in the corresponding layer *n*, and k is the filling parameter that qualitatively describes the jumping probability of adatoms to a lower layer. The coverage of each layer in this model can be evaluated numerically, subject to the conditions $\theta_0(t) = 1$, $\theta_n(0) = 0$, and $\theta_\infty(t) = 0$. The numerical solutions of the layer coverage are plotted in figure 5.3 (a) and (b), with k = 50 and 0, respectively. It refers to a non-diffusive 3D growth (k = 0), since all adatoms become a part of the adjacent layer instead of diffusing to the lower layer. When the filling parameter k increases, more adatoms will jump to the lower layer and complete it. Therefore, it corresponds to a layer-by-layer growth mode when k is equal to 50. In this growth mode, one layer is nearly completed before material is added to the following layer. The specular beam intensity is calculated by equation 5.3.2 based

on the kinematic approximation.[71]

$$I = \left| \sum_{n=0}^{\infty} (\theta_n - \theta_{n+1})(-1)^n \right|^2 \tag{5.3.2}$$

The calculated intensities based on the layer coverages, as shown in figure 5.3 (a) and (b), are plotted in (c) and (d) respectively. Intensity oscillations are observed in (c), and are characteristic of the layer-by-layer growth. Intensity damping is shown in (d), and refers to a three-dimensional (3D) growth. Compared with the kinematic approximation, the measured specular beam intensity oscillation in figure 5.1 (e) proves that the growth is in a 2D layer-by-layer mode. The period between two maxima (i.e., between a stronger and a weaker one) reflects the amount of time to complete a single monolayer (ML), and the average period is 223 seconds.

It needs to be mentioned that here one ML represents half a unit cell, in respective of (100)-plane, and this will be explained later when compared with the HRTEM cross-section images of the epitaxial film. The growth was stopped after 14 periods by closing the gallium effusion cell. A short annealing treatment was performed by keeping the substrate at the growth temperature in the oxygen plasma for 120 seconds. As shown in the inset of figure 5.1(e), the transient intensity recovered slowly, which is mainly because of the chamber pressure decrease. After the gallium shutter is closed, the pressure will gradually decrease and therefore less electrons will be scattered by the ions in the growth chamber. Since there was no change in the RHEED patterns observable either, it can be concluded that the thin layers are very stable under such an annealing process in limited period.

5.4 Formation of twin domains

As for homoepitaxy, the refractive index difference between the substrate and the thin film is zero, or close to zero due to the existence of defects, so the thickness of the epitaxial film can be hardly measured by x-ray reflectometry. Other analytic methods like secondary ion mass spectrometry and ellipsometry have been reported to measure the thickness of β-Ga_2O_3 homoepitaxial layers.[101] Both methods are mainly applied for the MOCVD samples, which are typically thicker than 100 nm. However in this study, the expected thickness is less than 10 nm, which is certainly below the thickness resolution of both methods. Since

the twin domains and stacking faults are exclusively found in the homoepitaxial film, the epitaxial layer can be determined by the presence of these defects. So the sample was prepared at the (010) cross-section for the HRTEM investigation in order to distinguish the epitaxial layer.

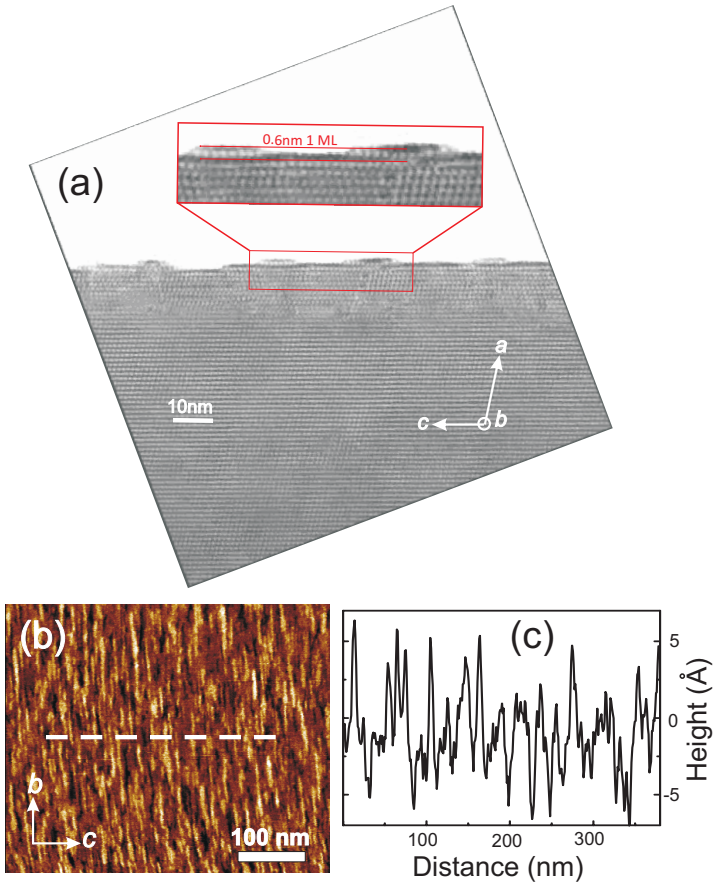

Figure 5.4 The HRTEM image at the (010) cross-section distinctly presents the projection of the islands on top of the (100) surface (a). The average sized is around 0.6 nm in height and 10 nm in width. This surface morphology is also confirmed by the AFM measurement (b). The height profile along [001] direction marked as the dashed line is plotted in (c).

The HRTEM image in figure 5.4 (a) shows the (010) cross-section of this (100)-oriented homoepitaxial thin film with the electron beam along the *b*-axis. On the (100) surface, there are several projections of the formed islands with the size of around 0.6 nm in height and 10 nm in width along the [001] direction. These islands are also observed in the AFM measurement. The surface morphology of the grown sample in figure 5.4 (b) reveals that these islands are strongly elongated along the *b*-direction and periodically distributed in the *c*-direction. The height profile at the dash line is plotted in figure 5.4 (c) showing that the nuclei have an average height of 0.6 nm and width of 10 nm approximately. With

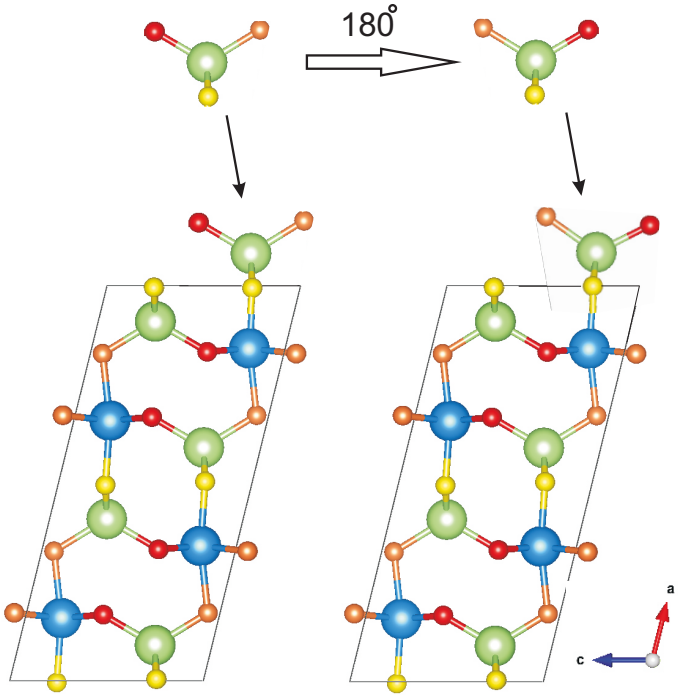

Figure 5.5 This stick and ball model depicts the double positioning of the adatoms on the (100)-oriented surface of β-Ga_2O_3. These adtoms proceed to grow and form 2D islands with the height of half-unit-cell (5.93 Å).

respective of the size of the nuclei, the HRTEM and AFM results are in correspondence with each other in the formation of the nuclei on the (100) surface.

Another HRTEM image with an increased magnification at the (010) cross-section, focusing on the defects, is shown in figure 5.6 (a). The bright dots in the phase contrast image exhibit half a unit cell [i.e., one ML] with a height of 5.93 Å. The image presents a high density of stacking faults (marked by blue lines) and formation of twin domains (green). The twins can be described by a c/2 glide reflection of the lattice,[98] and the formation can be interpreted by double positioning. As described in figure 5.5, the incoming adatoms to the (100) surface are either in the epitaxially coherent orientation (left) or in the twinned orientation (right). The growth proceeds to form 2D islands with the height of half-unit-cell (5.93 Å) in twinned orientations. Then these islands continue to grow laterally and coalesce forming a closed layer with twin domains. Comparing the selected area electron diffraction pattern of the substrate with that of the grown layers [figure 5.6 (b) and (d)], there are extra diffraction spots, highlighted by red circles, showing up in the layer pattern [figure 5.6(d)]. To have a better understanding on the origin of these extra dots, the diffraction patterns have been simulated using the JEMS software, which is based on the the multi-slice ap-

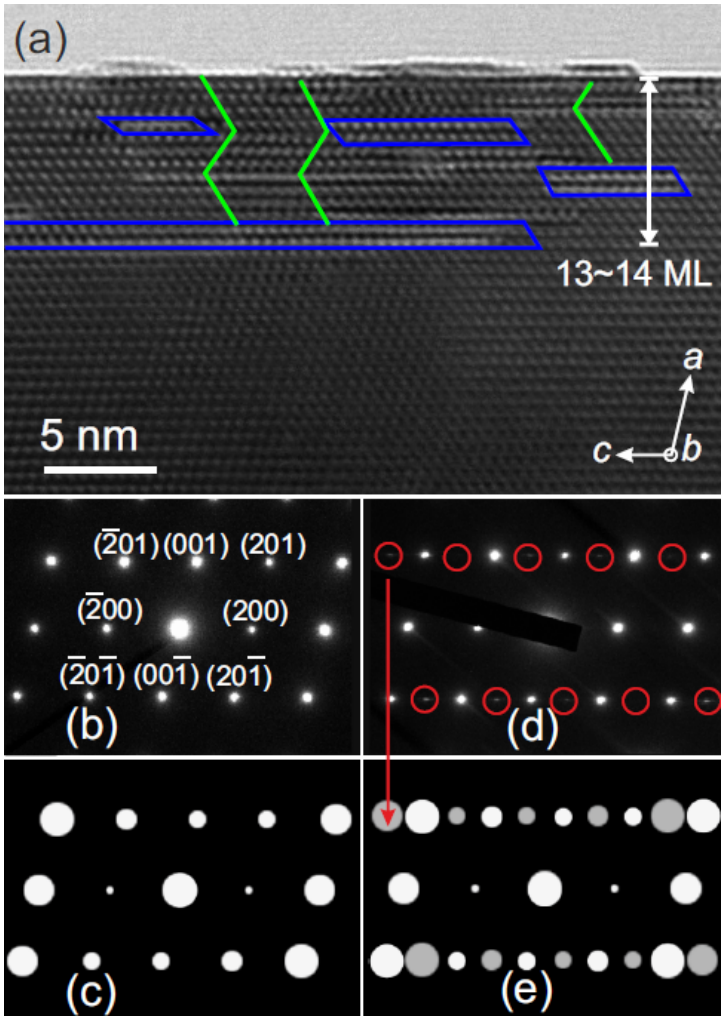

Figure 5.6 The HRTEM (a) depicts the homoepitaxial film with a thickness between 13 and 14 MLs. Twin domains and stacking faults are marked by green and blue lines, respectively. The electron diffraction patterns received at the pure substrate (b) and the grown film (d) agree very well with the simulations in (c) and (e), which confirms the presence of the twin domains in the grown layers.

proximation and the Bloch-wave method.[102, 103] In figure 5.6, the diffraction patterns are simulated for an ideal β-Ga_2O_3 structure (c) and a thin film consisted of twins as described by a c/2 glide reflection (e). The pattern in (c) shows a good agreement with the measured diffraction pattern of the substrate (b). As for the grown layers, the extra dots are also observed in (e) like in the experimental pattern (d). The qualitatively good agreement between simulation and experiments implies that these additional spots are due to twin domains exclusively present in the layer. Because of the high density of stacking faults, the homoepitaxial thin film becomes clearly distinguishable. The thickness of the epi-layer amounts to 83 Å, which is corresponding to a stacking of around 7 unit cells [i.e., 14 MLs]. Correlated with the RHEED oscillation in figure 5.1(e), which shows 14 periods, it is obvious that one oscillation is equivalent to one complete layer deposition of half a unit cell, namely one ML (5.93 Å).

As shown in figure 5.4, the nuclei have an average height of about 6 Å. They are strongly elongated along the *b*-direction. This height is very close to the thickness of one ML and is accordant with the 2D layer-by-layer growth mode as described by RHEED and HRTEM above. In this growth mode, the one-ML-high nuclei are first formed on the surface with an anisotropic shape, and some of these islands are in twinned orientation with respect to the substrate. As the growth proceeds, the islands will coalesce and construct a complete ML. This process is represented as one oscillation in the RHEED specular intensity plot. Besides that, the elongated shape of the islands also suggests that the reactants (gallium suboxides) may have higher mobility along *b*-axis than along other in-plane directions on the (100)-oriented surface. Their width of around 10 nm corresponds well with the average size of the twins in the HRTEM [figure 5.6(a)]. This proves that the twin boundaries are formed by coalescence of the nuclei on the surface (2D nucleation growth), which phenomenon is also observed in the homoepitaxy of (100)-oriented β-Ga_2O_3 in MOCVD.[98].

Crystal quality of the epitaxial film

The HRTEM results have provided detailed information on the crystal structure of the epitaxial film, it is necessary to evaluate the crystal quality over the sample. Figure 5.7 (a) shows the *in-situ* out-of-plane HRXRD curves of the pristine substrate (black) and the homoepitaxial layer (blue). It is obvious that no additional Bragg peak emerges after the growth, which already indicates there is no formation of another phase or structure. The (*h*00) peaks did not shift in the

grown sample compared with the pristine substrate within the resolution limit. It indicates that the epitaxial thin film is strain-free, as expected from homoepitaxy, and its surface plane is (100)-oriented. The (400) and (600) rocking curves have the FWHMs of around 0.02° before and after the growth, though most of the intensity comes from the substrate, however there is no further broadening under these peaks. Therefore the thin film, in respect of the out-of-plane direction, has a similar crystal quality as the substrate. It also shows that there is a rather broad diffuse scattering underneath the (200) reflection. In terms of a quantitative analysis, we have performed a Gaussian fit covering this area of the (200) diffraction curve to extract the FWHM of 0.39 $Å^{-1}$. This feature might be a result of minor distortion of the crystal structure due to the stacking faults and twins as seen in the HRTEM images.

Since the out-of-plane HRXRD is not sensitive to the in-plane domains, the in-plane structure of the layer was investigated by azimuthal RHEED scans. This scan geometry provides an almost planar cut in reciprocal space parallel to the surface at a very small vertical momentum transfer due to the small incident and outgoing angle.[104] The azimuthal RHEED maps measured before and after the growth are plotted in the same in-plane orientation in figure 5.7 (b) and (c), which have very similar patterns with each other. As known, the $(\bar{1}02)$ plane normal is vertically tilted from the [001] direction by only 0.1° in the monoclinic system of β-Ga_2O_3, so the (100)-oriented surface can be approximated as an orthorhombic structure. In this assumption, the (100)-plane normal is in the out-of-plane direction, while the in-plane (010) and $(\bar{1}02)$ are perpendicular to each other. The azimuthal RHEED pattern of the cleaved substrate showed exactly such an in-plane symmetry, and this pattern was well preserved during epitaxial growth. In both plots, the diffractions up to the second order in the $\{010\}$ direction as well as the fifth orders in the orthogonal in-plane direction have been well identified. It is worth to note that there is no additional feature indicating a different phase or orientation within the grown layer, except for the twins found in the HRTEM. By ignoring the 0.1° tilting in $(\bar{1}02)$, the twins can not break the surface lattice symmetry and therefore were not measurable in the azimuthal RHEED scans close to the surface. As a result, the in-plane azimuthal RHEED scans indicate a coherent homoepitaxial growth of the (100)-oriented β-Ga_2O_3, except for the twin domains exclusively in the epitaxial film.

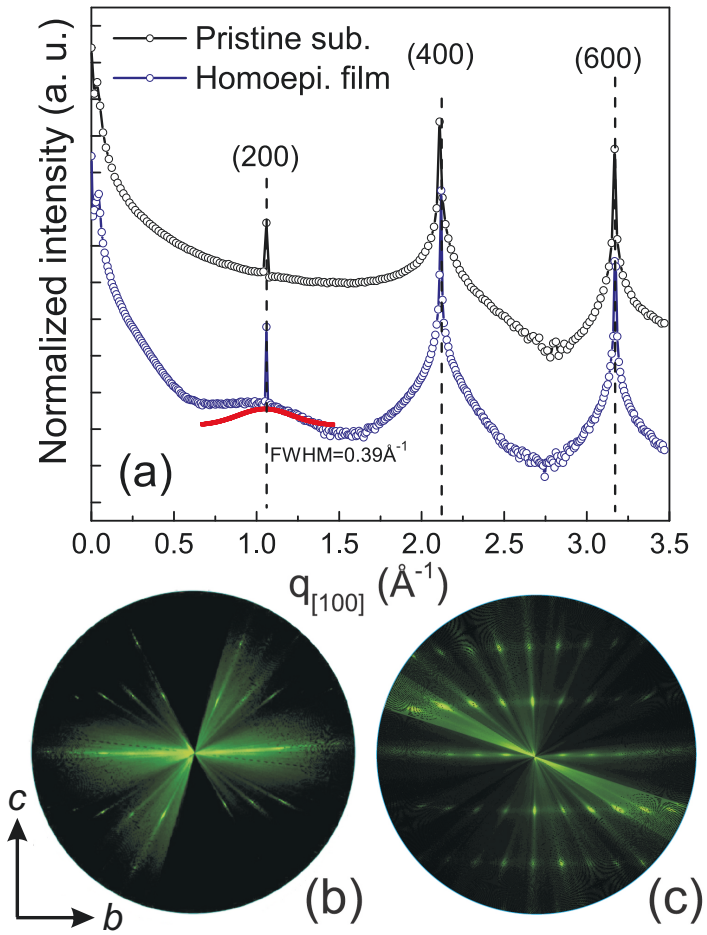

Figure 5.7 (a) X-ray diffraction profiles along the surface normal taken at the pristine β-Ga_2O_3 substrate and homoepitaxially grown layer. The homoepitaxial film shows a diffuse scattering near the (200) diffraction, and its FWHM is around 0.39 $Å^{-1}$ as calculated by a Gaussian fit (the red curve). (b) and (c) depict the in-plane azimuthal RHEED pattern before and after growth.

5.5 The growth mode at higher growth rates

The RHEED specular beam oscillations have proved a 2D layer-by-layer growth mode in the (100)-oriented β-Ga_2O_3 homoepitaxy. However, for further device applications, a thicker layer with a higher growth rate would be preferred. To increase the growth rate, the gallium flux was enlarged by increasing the effusion cell and hot-lip temperatures to 1023 and 1173 K in the first 3600 seconds, and afterwards further to 1073 and 1223 K resulting in respective growth rates of 205 and 132 seconds/ML. As shown in figure 5.8, the RHEED pattern after the growth is identical with that in figure 5.1 (d), and the azimuthal RHEED scan is equivalent to that in figure 5.7. The specular intensity evolution is plotted in figure 5.9 (a). The intensity oscillation behaves similar to figure 5.1 (e), which is characterized by alternating strong and weak maxima, one after another. However, the oscillation amplitude, or to say the difference between the maximum and minimum, declines as the layer grows thicker.

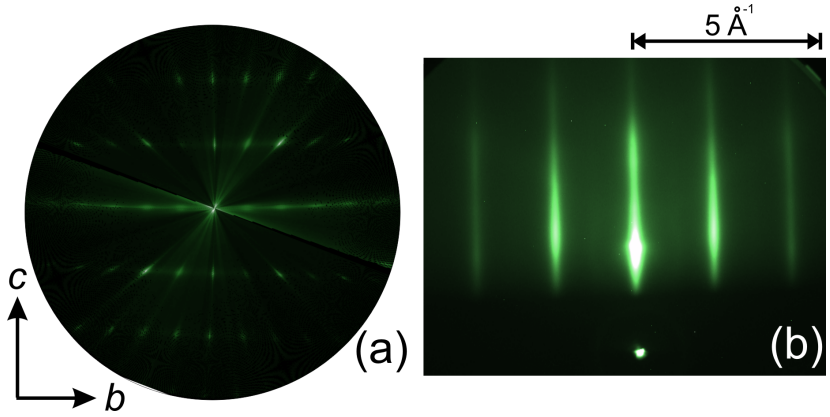

Figure 5.8 (a) The azimuthal RHEED map and (b) the RHEED pattern of the homoepitaxial (100)-oriented β-Ga_2O_3 after 47 periods of oscillations

In figure 5.9 (b), the intensity close to the (400) Bragg peak shows thickness fringes, which indicate a layer distinguishable from the substrate. Since MBE is generally expected to ensure extremely high purity of the epitaxial film, these fringes probably are caused by the phase shift due to half unit cell stacking faults in the epitaxial film that break the crystal symmetry. Based on the fringe separation, the epitaxial layer thickness can be deduced to 283 Å, equivalent to approximately 47 MLs, which agrees well with the number of RHEED oscillations plotted in figure 5.9 (a). It reconfirms the observation that the (100)-oriented β-Ga_2O_3 is homoepitaxially grown in a 2D layer-by-layer mode with half unit cell high MLs, as discussed in the thinner sample.

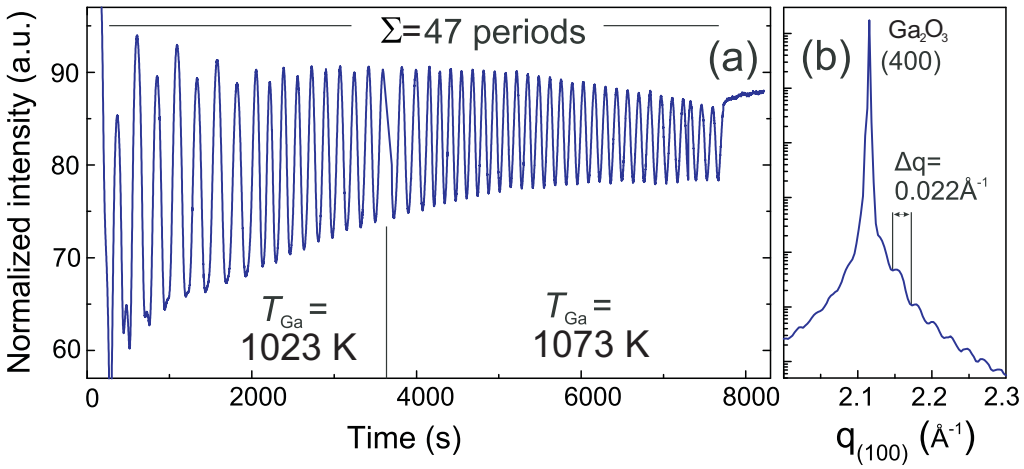

Figure 5.9 (a) The RHEED oscillations of another sample with 47 periods and higher growth rates. (b) The out-of-plane (400) Bragg diffraction with its Laue fringes.

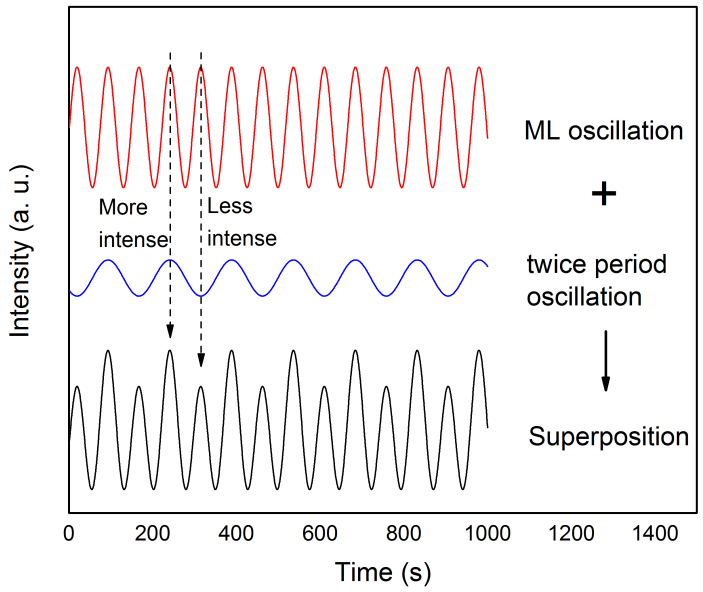

Figure 5.10 The RHEED oscillation can be treated as a superposition of two oscillations: one with a smaller period (red), the other one (blue) with a twice period and different phase.

The RHEED intensity profiles in figure 5.1 (e) and figure 5.9 (a) can be expressed as a superposition of two oscillations with different periods. Mathematically, this feature is interpreted as a superposition of two oscillations with different period and phase, as sketched in figure 5.10. The oscillation with the smaller period (red) can be well explained by ML growth, as also proved by HRTEM and AFM results. Though the oscillation with twice the period (blue)

coincides with the formation of one unit cell thickness (2 MLs), the mechanism behind is still under research. Fukutani *et al.* have found a similar behavior in the homoepitaxial Ge (111) growth and attributed it to the superposition of specular and diffuse scattering.[105] However, this interpretation can only explain a bilayer growth situation. Another issue might be the different reflectivities of domains - an effect, which has been reported for the homoepitaxial growth of Si (100) by Berrie and Loene.[106] However, based on the HRTEM cross-section images, the twin domains in our study did not present a clear periodic distribution along the growth direction [100]. In this case, the main mechanism behind the observed double periodicity needs to be further studied.

5.6 Summary

In this chapter, we have studied the growth mode of (100)-oriented β-Ga_2O_3 homoepitaxy in MBE and the formation of the twin domains and stacking faults in the epitaxial film by performing *in-situ* and *ex-situ* characterizations. The conspicuous RHEED oscillation and the evolution of the RHEED pattern have clearly proved a 2D layer-by-layer growth mode. The (100)-oriented β-Ga_2O_3 films are coherently grown on the substrates, however the films reveal twin domains and a high density of planar stacking faults, which are not found in the substrates. The formation of the twin domains is explained by double positioning of the crystal. During the growth, some of the unit cells are formed with an in-plane rotation of 180°, so the [001] axis of the formed islands are pointing to the [00$\bar{1}$] direction of the substrate. The half ML high islands are also found to be elongated along *b* axis, which implies a higher mobility of the reactants, gallium suboxides, in this direction. As the islands grow laterally, they coalesce to complete one ML and form twin boundaries. The layer-by-layer growth mode in MBE ensures an atomically smooth surface and a very precise control of the film thickness. Though the epitaxial layer consists of twin domains, it still shows high crystal quality as evidenced by the small FWHM of the HRXRD rocking curves.

6 Heteroepitaxy of Ga_2O_3 on various oriented sapphire substrates

In previous studies, *c*-plane oriented sapphire (α-Al_2O_3) has been widely used as a substrate for a broad range of heteroepitaxial growth of semiconducting materials, e.g. GaN,[107] InN,[108] and ZnO,[109] due to the similar hexagonal crystal symmetry and relatively small lattice mismatch. The heterostructure of semiconducting Ga_2O_3 thin film on insulating sapphire substrate is a very promising candidate in applications of two-dimensional electron gas devices, such as quantum wells and high-electron-mobility transistors. In a sandwich structure of Al_2O_3/Ga_2O_3/Al_2O_3, the large difference in fundamental bandgap between Ga_2O_3 (4.4—5.08 eV, depending on the modification) and α-Al_2O_3 (8.8 eV [110]) confines the charge carriers (electrons and holes) tightly in the vertical dimension of the semiconducting Ga_2O_3 thin film and allow them to move in two dimensions.[111] Among the five phases, as introduced in chapter 2, α-Ga_2O_3 shares the same crystal structure with the sapphire substrate, and has smaller lattice mismatch (4.6 % and 3.4 %, respectively along *a*- and *c*-axes). Therefore, it promotes a great challenge to grow α-Ga_2O_3/α-Al_2O_3 heterostructures in order to realize the two-dimensional structure.

The α-phase is thermodynamically favorable at very high temperature and pressure, and appears meta-stable at ambient condition. [35, 81] It has been found that, on (0001)-oriented sapphire substrate, a coherent α-Ga_2O_3 thin film is only stable in the very first three monolayers as observed by MBE, PLD, and MOCVD growth, afterwards the thermodynamically more stable β-Ga_2O_3 with in-plane rotational domains proceeds to grow on top.[45] Though this β-Ga_2O_3 layer is more stable at ambient condition and has an even larger band gap difference with the sapphire substrate, the presence of rotational domains is a serious disadvantage for applications. Therefore, it is more promising to grow single crystal α-Ga_2O_3 on sapphire substrate and try to stabilize it to the thickness for devices (i.e., at least 5 nm for quantum wells).

In this chapter, we have studied the heteroepitaxy of Ga_2O_3 on sapphire substrates in different surface orientations, focusing on the crystal modification and

the strain status during the growth. The *in-situ* analytical tools are synchrotron-based HRXRD (including GID) and RHEED.

6.1 Kinematic scattering approximation

For quantitative interpretation of HRXRD results, two approaches are commonly applied: the dynamic theory and the kinematic theory.[69, 112] In the dynamic theory, the impinged x-rays are subjected to multiple diffraction in a perfect or near perfect crystal, such as bulk silicon,[113] whereby the diffracted waves will interfere with each other, as sketched in figure 6.1 (a). However, most of the epitaxial layers in the semiconductor study are far from perfect crystal and are proved to contain mis-oriented mosaic blocks, as shown in figure 6.1 (b), therefore the multiple interference effects, that has to be considered in the dynamic case, can be neglected in the kinematic approach. In this case, the kinematic scattering approximation is used to analyze the HRXRD results in this study of heteroepitaxy.

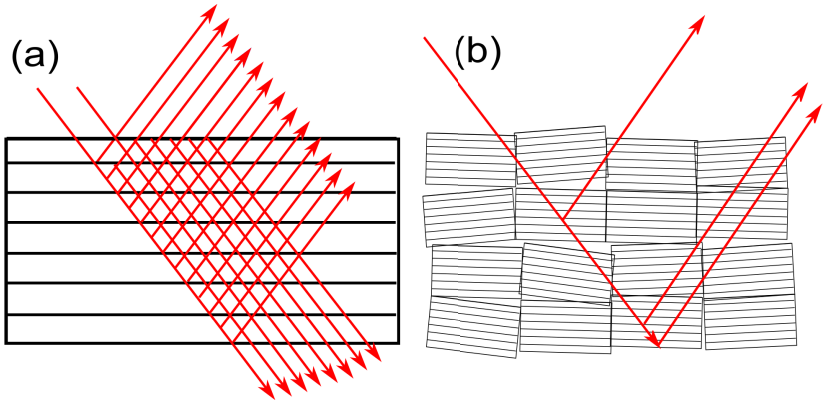

Figure 6.1 Sketch of a numerical simulation on the basis of dynamic theory (a) and kinematic theory (b). In the kinematic approximation, the crystal is considered far from perfect, therefore the multiple interference can be neglected.

When x-rays impinge on an atom or a crystal, they are scattered by the electrons. In the kinematic approximation, we simply sum all the amplitudes of the EM waves as scattered from all the electrons inside the probed structure. The amplitude of the scattered EM wave is described by the Thompson formula 6.1.1. In this formula, the incoming wave (wave vector k_i) with an amplitude of A_0 is scattered by an electron (m is the electron mass and e is the electron charge) at r_e, and the scattered wave (wave vector k_f) has an amplitude of A_1. R_0 is the distance from the electron to the detector, and c is the speed of light. These vectors in the real space are sketched in figure 6.2 (a).

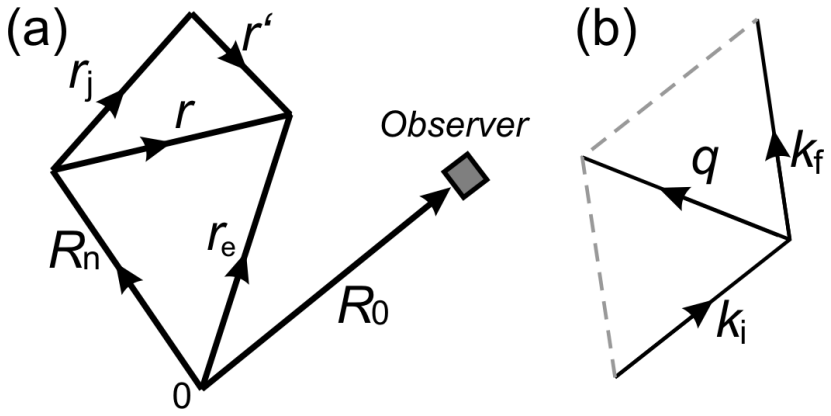

Figure 6.2 (a) In the real space, point 0 is the origin, vector R_n points to the origin of the *n*th unit cell, r_j starts from the origin of the *n*th unit cell and ends at the *j*th atom of it, *r*' points to an electron in this atom. (b) In the reciprocal space, k_i and k_f are the incident and diffracted wave vectors. The transfer momentum *q* is the difference between them following $q = k_f - k_i$.

$$\begin{aligned} A_1 exp(-ik_f \cdot r_e) &= A_0 \frac{e^2}{mc^2} \frac{1}{R_0} exp(-ik_i \cdot r_e) \\ A_1 &= A_0 \frac{e^2}{mc^2} \frac{1}{R_0} exp\left[i(k_f - k_i) \cdot r_e\right] \end{aligned} \tag{6.1.1}$$

As described in equation 3.2.3 and sketched in figure 6.2 (b), the momentum transfer vector $q = k_f - k_i$ is the difference between the out-going wave vector k_f and the incoming wave vector k_i. After the replacement of $k_f - k_i$ by q, formula 6.1.1 can be written as equation 6.1.2.

$$A_1 = A_0 \frac{e^2}{mc^2} \frac{1}{R_0} exp(iq \cdot r_e) \tag{6.1.2}$$

It is necessary to take into account the electron density distribution in the calculation, in order to calculate the scattering from one atom. Here the electron density at a certain position inside one atom, as described by vector r' in the real space, is given by ρ(r'). So the amplitude of the EM waves scattered by one atom, or the summation of all the electrons in one atom, is written as an integration 6.1.3. Here, R_n is the vector to the origin of the *n*th unit cell, and r_j is the vector to the *j*th atom in the *n*th unit cell.

$$A_2 = A_0 \frac{e^2}{mc^2} \frac{1}{R_0} \int_{-\infty}^{\infty} \rho(r') exp\left[iq \cdot (R_n + r_j + r')\right] d^3r' \tag{6.1.3}$$

It is shown in equation 6.1.3 that the volume integration over vector r' is a Fourier transform of the electron density in one atom as a function of the reciprocal vector q. This part is called the atomic form factor f(q), which is described

by equation 6.1.4.

$$f(q) = \int_{-\infty}^{\infty} \rho(r')exp(iq \cdot r')d^3r' \tag{6.1.4}$$

Therefore, the sum of the amplitudes from each electron in the *j*th atom is written as equation 6.1.5.

$$A_2 = A_0 \frac{e^2}{mc^2} \frac{1}{R_0} f(q)exp\left[iq \cdot (R_n + r_j)\right] \tag{6.1.5}$$

In a larger scale, the scattering from one unit cell can be considered as a sum of all the atoms in one unit cell. In the calculation, it is assumed that there are N_c atoms in one unit cell. The atomic form factor of the *j*th atom in the *n*th unit cell is $f_j(q)$. Since $f_j(q)$ is related to the electron density distribution in one atom, therefore it contains the chemical information of this atom. In this research, $f_j(q)$ is considered as a constant for all the atoms in the simulated structure in order to simplify the calculation. The summation of the amplitudes in the *n*th unit cell is described by equation 6.1.6.

$$\begin{aligned} A_3 &= A_0 \frac{e^2}{mc^2} \frac{1}{R_0} \sum_{j=1}^{N_c} f_j(q)exp\left[iq \cdot (R_n + r_j)\right] \\ &= A_0 \frac{e^2}{mc^2} \frac{1}{R_0} F(q)exp(iq \cdot R_n) \end{aligned} \tag{6.1.6}$$

F(q) is called the structure factor of this unit cell, as defined by equation 6.1.7.

$$F(q) = \sum_{j=1}^{N_c} f_j(q)exp(iq \cdot r_j) \tag{6.1.7}$$

Since the EM waves are scattered by the electrons, the structure factor can be considered as the Fourier transform of the electron density distribution $\rho_{uc}(r)$ in one unit cell, as described by equation 6.1.8. In this equation, r is the vector that starts from the origin of the *n*th unit cell, but also ends inside.

$$F(q) = \int \rho_{uc}(r)exp(iq \cdot r)d^3r \tag{6.1.8}$$

In a crystal, the unit cells are stacked periodically in the three-dimensional space, therefore it is necessary to add up the scattered EM waves from each unit cell in order to calculate the diffracted beam intensity. These periodically stacked unit cells constitute different planes in the crystal, and constructive interference of the scattered EM waves occurs between some of the planes at the respective

Bragg angles. For instance, a crystal is described in a coordinate system with three independent vectors a_1, a_2 and a_3, and there are N_1, N_2 and N_3 unit cells in each axis. The origin of any unit cell in this crystal can be described by vector $R_n = n_1a_1 + n_2a_2 + n_3a_3$, where n_1, n_2 and n_3 are discrete numbers smaller than N_1, N_2 and N_3 respectively. As a sum of all the unit cells, the amplitude of the scattered EM waves is written as equation 6.1.9.

$$A_3 = A_0 \frac{e^2}{mc^2} \frac{1}{R_0} F(q) \sum_{n_1=0}^{N_1-1} \sum_{n_2=0}^{N_2-1} \sum_{n_3=0}^{N_3-1} exp\left[iq \cdot (n_1a_1 + n_2a_2 + n_3a_3)\right] \quad (6.1.9)$$

In one dimension or one direction, the summation can be written as following.

$$\begin{aligned} S_N(q) &= \sum_{n=0}^{N-1} exp(iqan) \\ &= \frac{1 - exp(iqaN)}{1 - exp(iqa)} \end{aligned} \quad (6.1.10)$$

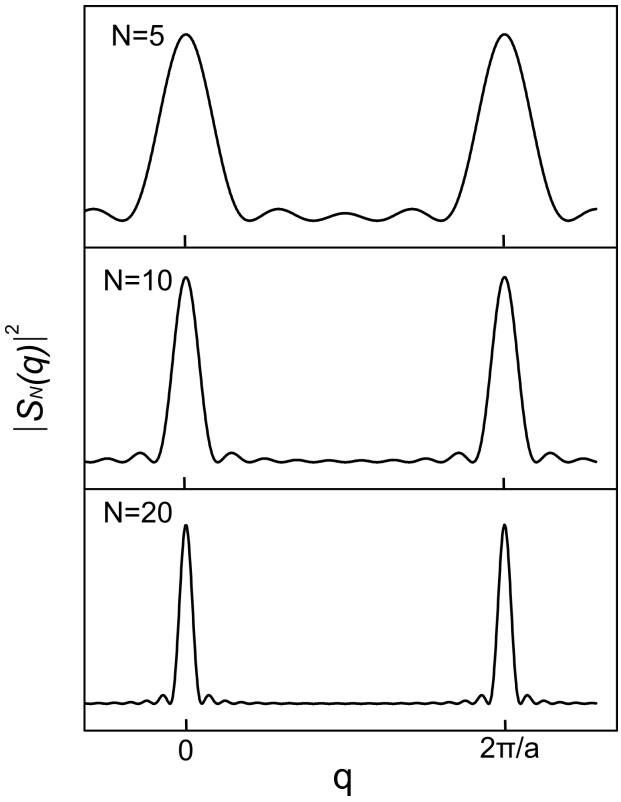

Figure 6.3 Plot of equation 6.1.11, when N is equal to 5, 10, and 20. There are N-2 fringes between two maxima.

The intensity measured in the experiment is proportional to the square of the

amplitude, which includes also the square of the summation, as presented by equation 6.1.11. In figure 6.3, the intensity is plotted as a function of q for a crystal with N = 5, 10, and 20. The maxima appear when q = 2πL/a, where L is a discrete number. There are N-2 fringes between two maxima, and two neighbor fringes are separated by 2π/Na.

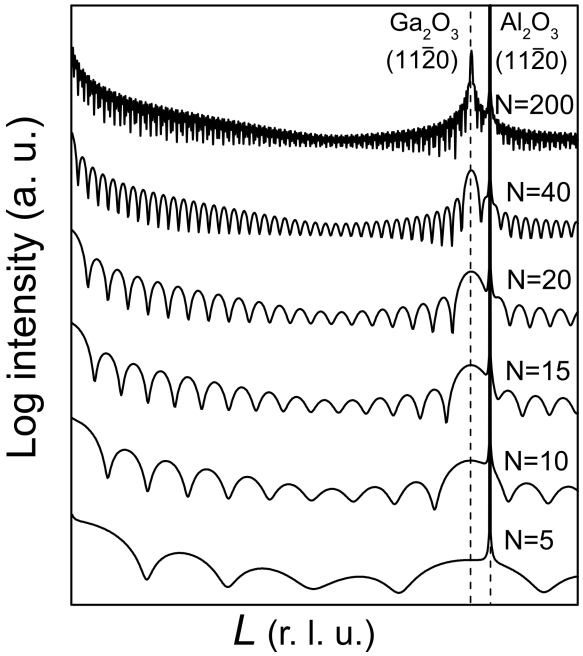

Figure 6.4 Kinematic scattering simulations based on a heteroepitaxial structure consisting of an a-plane sapphire substrate and a coherently deposited α-Ga_2O_3 layer with different thickness corresponding to different numbers N of unit cells. *L* is the Miller index in the crystallography system.

$$|S_N(q)|^2 = \frac{sin^2(Nqa/2)}{sin^2(qa/2)} \tag{6.1.11}$$

For a crystal bulk, the number of stacked unit cells in any direction is considered to be very large, therefore the numerator in equation 6.1.11 varies extremely fast with q. However, this rapid change can hardly be measured due to limited resolution, so this numerator is treated as a constant value a_c for the calculation, as shown in formula 6.1.12.

$$|S_N(q)|^2 = \frac{a_c}{sin^2(qa/2)} \tag{6.1.12}$$

In heteroepitaxy, the structure consists of a thick substrate and at least one epitaxial thin film. The thickness of the substrate is in the scale of hundreds of micrometers (a much larger N), however the thin film is only up to tens of nanometers (a small N). Therefore, the amplitude can be expressed as formula 6.1.13,

where F_S and F_L are the structure factors of the substrate and the epitaxial thin film.

$$A_{sum} = A_0 \frac{e^2}{mc^2} \frac{1}{R_0} \left[F_L \frac{1}{1 - exp(iqa)} + F_L \frac{1 - exp(iqaN)}{1 - exp(iqa)} \right] \tag{6.1.13}$$

For example, in our experiment α-Ga_2O_3 is coherently deposited on a-plane [$(11\bar{2}0)$-plane] sapphire substrate. The thickness of the substrate is around 450 μm and the epitaxial layer is less than 20 nm. Therefore we use formula 6.1.13 to calculate the kinematic scattering of this heteroepitaxial structure. The calculated intensity profiles are plotted with different N in figure 6.4. N is the number of α-Ga_2O_3 unit cells stacked along the out-of-plane direction.

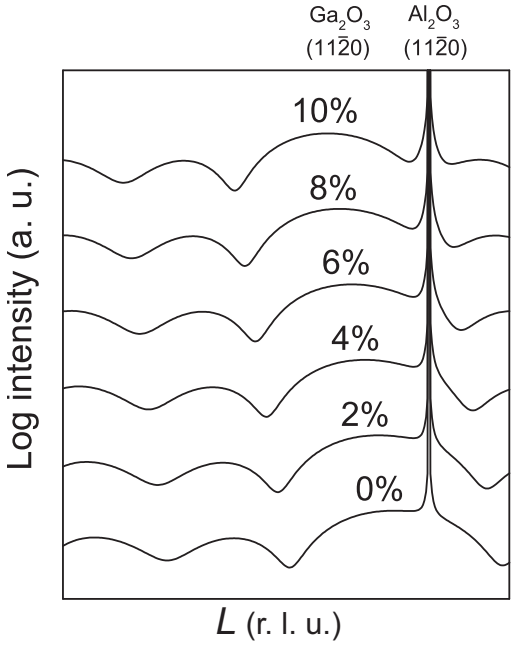

Figure 6.5 Kinematic scattering simulations based on a heteroepitaxial structure the same as figure 6.4 with N = 6. This structure is under a tensile strain ϵ_1 ranging from 0% to 10%.

In figure 6.4, the α-Ga_2O_3 $(11\bar{2}0)$ peak appears on the left side of the α-Al_2O_3 $(11\bar{2}0)$ peak, as expected from the lattice mismatch. Since no strain has been induced in the epitaxial layer, the α-Ga_2O_3 $(11\bar{2}0)$ peak stays at the same q as the thickness gradually changes from N = 5 to N = 200. Δq, the period of the fringes, gradually decreases as N increases from 5 to 200, following the relationship $\Delta q = 2\pi/Na$. If N becomes very large, such as bulk crystal, Δq will be smaller than the experimental resolution. Therefore, the measured intensity profile of the substrate is a smooth curve.

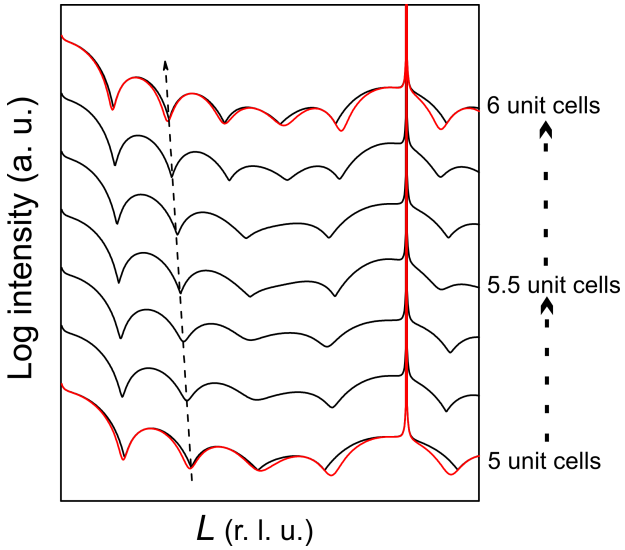

Figure 6.6 Kinematic scattering simulations based on a crystal that gradually increases its thickness from 5 to 6 unit cells with N = 1 (black curves). As a comparison, the red curves are calculated by importing one unit cell into the calculation with N = 5 and N = 6.

In heteroepitaxial growth, the lattice mismatch generates stress at interface and causes structure deformation especially in the epitaxial film. Therefore it is necessary to consider the strain of the thin film in the calculation for heteroepitaxy. In this thesis, the strain refers to the amount of deformation of the thin film compared with its strain-free bulk, and is described by equation 6.1.14.

$$\epsilon = \frac{a_L^{exp} - a_L^{bulk}}{a_L^{bulk}} \tag{6.1.14}$$

Here, ϵ is the strain in the thin film, a_L^{exp} is the lattice parameter measured in experiments, and a_L^{bulk} is the lattice parameter of the strain-free bulk. In this approach, the lattice parameter, which is expected to be strained, is replaced by a deformed lattice parameter. For example, the lattice constant a is replaced $a_1' = (1+\epsilon_1) \times a_1$, where ϵ_1 is the value of strain. An alternative is to create deformed unit cells at the initial step and then use them for the kinematic calculation. The simulation in figure 6.5 clearly shows the shift of α-Ga_2O_3 $(11\bar{2}0)$ peak as the tensile strain increases from 0 to 10% with a step size of 2%.

As discussed, the layer thickness can be tuned by adjusting N in formula 6.1.13, however, such a discrete thickness is not sufficient to describe the thin film when the thickness is very small. For example, if the layer thickness as calculated from measured fringe period Δq is 5.5N in an experiment, it can be simulated precisely by neither 5N thick film nor 6N thick film in the calculation. Therefore, instead of using a unit cell, we import just one crystal consisted of stacked unit

cells and part of one unit cell, depending on the thickness, into the calculation, and set N to 1. In this case, the structure factor F_L in formula 6.1.13 is a Fourier transform of the electron density in this created crystal, but not one unit cell.

In figure 6.6, several crystals are created with the thickness that gradually changes from 5 unit cells to 6 unit cells. The simulated intensity profiles are plotted in black. It is clear that the period of the fringes becomes smaller as the thickness increases in a step less than one unit cell thickness. The red curves are simulated based on one unit cell with N = 5 and N = 6, as discussed in figure 6.4. It indicates that the created crystal consisted of unit cells gives a similar result in the simulation, because the black and red curves have a good agreement with each other.

The heteroepitaxial study in this thesis mainly focuses on the structure modification, the thin film thickness, and the strain status. Since the heteroepitaxial films in this study are far from a perfect crystal, it is proper to use the kinematic scattering approximation to interpret the measured HRXRD results quantitatively.

6.2 The structure of Ga_2O_3 on *c*-plane sapphire substrates

In the plasma-assisted MBE growth, single-crystalline layers of meta-stable α-Ga_2O_3 grown on *c*-plane sapphire have been demonstrated only up to a thickness of about three monolayers.[25, 45] Above this critical thickness, the layer continues to grow in its monoclinic β-modification, as shown in figure 6.7, having $(\bar{2}01)$-oriented surface. However, this β-Ga_2O_3 layer is full of rotational domains due to the six-fold symmetry of the substrate. The change of the growing phase, from α-Ga_2O_3 to β-Ga_2O_3, is a phenomenon that has been also observed in MOCVD and PLD.[45, 79]

In this section, we report on a detailed *in-situ* study of the Ga_2O_3 grown on *c*-plane sapphire substrate with a focus on the change of the phase and the strain status during the growth. The epitaxial growth was carried out in the PHARAO beamline endstation as described in chapter 3. During the deposition, the growing crystal phase and the strain in the film were continuously monitored by *in-situ* out-of-plane symmetric 2θ-ω and in-plane GID scans.[114]

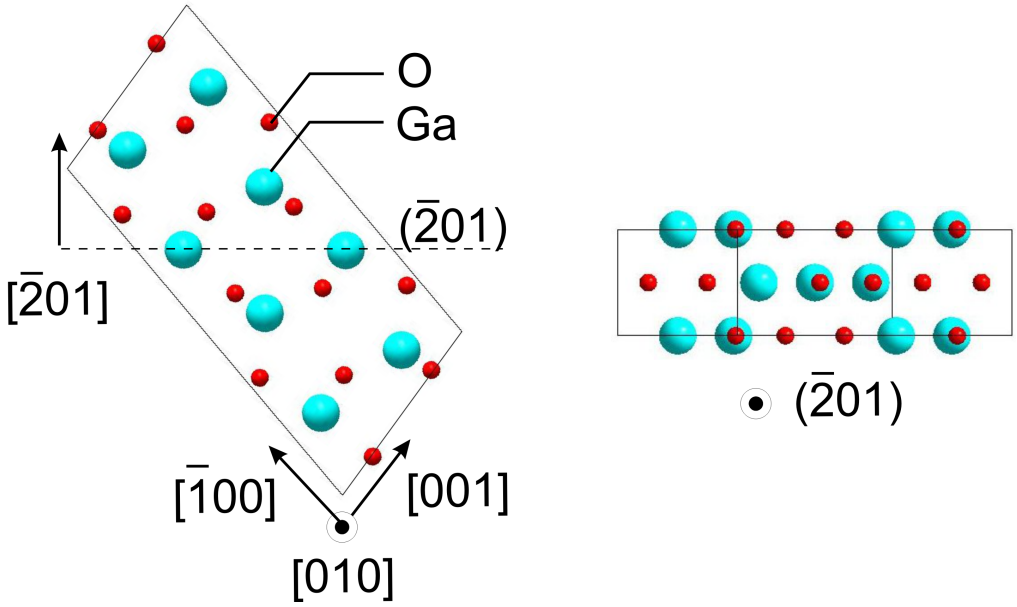

Figure 6.7 Sketch of the monoclinic unit cell of β-Ga_2O_3 as seen along (left) and perpendicular (right) to the ($\bar{2}$01) lattice plane.

6.2.1 Preparation of substrates

The substrates used for the experiments described in this chapter are single-side-polished (SSP) 2-inch α-Al_2O_3 wafers without any intentional miscut. Normally the growth of Ga_2O_3 is carried out at a temperature above 873 K,[25, 90, 115] therefore a high and stable heat transfer medium to the substrate is necessary. So the sapphire substrates were sputtered with roughly 1 μm titanium on the backside to increase the heat transfer efficiency, because titanium has a higher thermal conductivity than sapphire. After sputtering, the substrates then were cleaved into smaller parts with the size of around 3 cm^2, which yields a more homogeneous temperature distribution over the surface. Before being mounted on the substrate holder, the substrates were cleaned by ultrasonic bath in acetone for 20 min, and in isopropanol for another 20 min, having the surface ready for epitaxy. This cleaning is a standard epi-ready process for the sapphire substrates used in this thesis. The substrates were glued on the substrate holders by indium bonding.

6.2.2 β-Ga_2O_3 formation on *c*-plane sapphire substrate

Before the *in-situ* continuous measurement during the growth, we had performed preliminary *ex-situ* investigation on the strain dynamics and phase formation of thin Ga_2O_3 grown on *c*-plane sapphire substrates. Four samples were grown un-

der exactly the same condition, however with different thickness as 6.5 Å, 13 Å, 26 Å, and 133 Å. These samples were grown in a MBE system, named as M8, which is a very similar plasma-enhanced MBE system as the one at the PHARAO endstation. One exception is the sample mounting orientation, which is horizontal in M8, but vertical in the PHARAO MBE system. The growth was kept in an oxygen-rich condition, in which the growth rate is dominated by the metal flux and the etching effect caused by the gallium flux can be neglected.[90] The plasma cavity was set to 300 W at a constant oxygen flux of 1 sccm, whereas the gallium effusion cell and the hot-lip were kept at 973 and 1123 K. The substrate temperature was 973 K as measured by a thermocouple mounted on the backside of the heater.

After growth, these four samples with different layer thickness were then transfered to the MBE at PHARAO beamline. During the transfer process, the samples were exposed to atmosphere air and kept at room temperature. Because of the exposure, the samples went through a degas process in the load-lock chamber before being transferred to the main growth chamber. As these samples were mounted on a six-circle diffractometer in a synchrotron beamline, both out-of-plane crystal truncation rod (CTR) and in-plane diffractions (by GID) were carried out on these four samples, gaining a comprehensive view in the crystal structure.

The diffraction curves of these four samples are plotted in figure 6.8, whereby the curves along the growth direction, thus in the α-Al_2O_3 [0001] CTR, are plotted in (a), and those in the α-Al_2O_3 [11$\bar{2}$0] direction are plotted in (c). In both arrays of diffraction curves, a sapphire substrate reflection is inserted as a substrate reference. The layer thickness d of each sample is extracted from the period of the Kiessig fringes Δq, based on $d = 2\pi/\Delta q$.[116, 117] In figure 6.8 (a), it is clear that below a layer thickness of 26 Å, there is no indication for the presence of the β-Ga_2O_3, as neither ($\bar{2}$01) nor ($\bar{4}$02) reflection is probed, however the (0006) diffraction peak from α-Ga_2O_3 is clearly observed, indicating the formation of the pseudomorphic α-Ga_2O_3. As the Ga_2O_3 layer grows thicker, the α-Ga_2O_3 (0006) peak is systematically shifting to a larger q-value, and endorse a shrinking out-of-plane parameter. Besides the relaxation of the initial α-phase, β-Ga_2O_3 is formed as proved by the presence of a ($\bar{2}$01) maximum at a considerably larger thickness of 133 Å. The accompanying second order ($\bar{4}$02) reflection merges, however, with the closely positioned α-Ga_2O_3 (0006) peak. In figure 6.8, as a consequence at layers thicker than approximately 26Å, the α-Ga_2O_3 (0006)

peak and the β-Ga_2O_3 ($\bar{2}01$) peak become hard to disentangle. As a counterpart one can observe, in the orthogonal in-plane direction, an initial pseudomorphic growth of the α-Ga_2O_3 by a lattice-matched layer contribution of Ga_2O_3 ($11\bar{2}0$) directly underneath the substrate reference, followed by an abrupt relaxation as the layer gets thicker, see the inset in figure 6.8 (c).

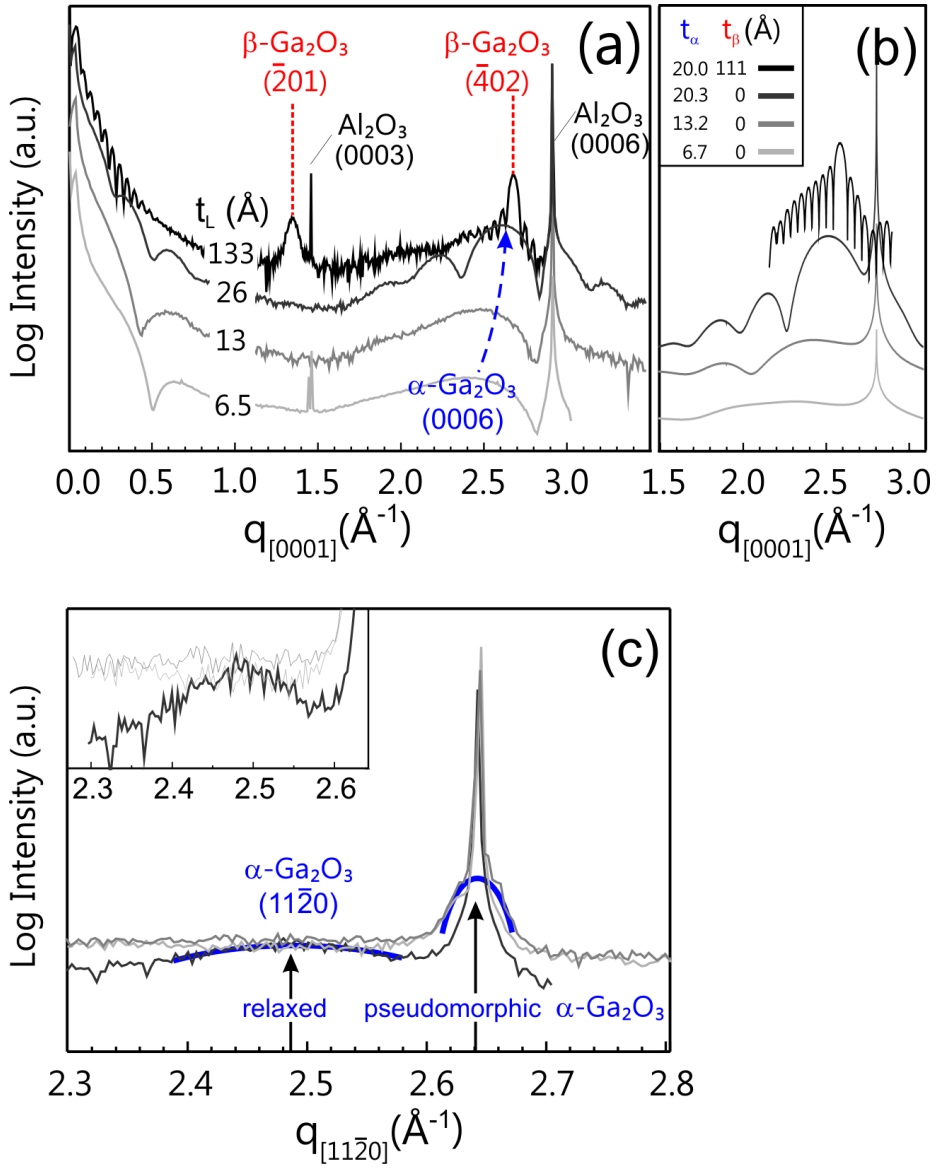

Figure 6.8 *Ex-situ* measured, out-of-plane crystal truncation rods of Ga_2O_3 layers grown at different deposition times on *c*-plane sapphire (a). Kinematic scattering simulations based on a two-layer system consisting of α- and β-Ga_2O_3 of different thicknesses $t_{\alpha,\beta}$ and relaxation (b). Grazing incidence diffraction along $[11\bar{2}0]$ (c). Both scan directions are parallel (a,b) and perpendicular (c) the surface normal, i.e. $[0001]$.

Besides the experimental results, we have performed kinematic scattering simulations, the standard approach of surface x-ray analysis, in order to extract quan-

titative information from the experimental data. The simulations in figure 6.8 (b) base on either a pure α-Ga_2O_3 ($t_L \leq 26$ Å) or a stack consisting of both α- and β-Ga_2O_3 (t_L=133 Å) quantitatively substantiate to the described growth scenario. In the simulation of α-Ga_2O_3 layer we have considered several unit cells reflecting the different layer thicknesses along the surface normal, and calculated the diffraction curves from these artificial layers. As shown in figure 6.8 (a, b), the simulated curves agree very well with the experimental data. By extracting the position of the diffraction peak from the epitaxial layer, the out-of-plane strain the α-Ga_2O_3 layer is exposed to can be derived. As the α-Ga_2O_3 layer becomes subsequently thicker [i.e., 6.7 Å (light gray), 13.2 Å (medium gray) and 20.3 Å (dark grey)], the tensile strain is partially relieved since the maximum is still on the left side of the theoretical relaxed peak. As for dark grey labeled sample, the difference between the thicknesses calculated from x-ray reflectivity fringes (26Å) and diffraction fringes (20.3Å) might be related to a noncrystalline Ga_2O_3 layer, which has the same refractive index but does not contribute to the (0006) diffraction. This out-of-plane relaxation along [0001] in conjunction with the evolution of the in-plane lattice parameter in figure 6.8 (c) gives already a first quasi-static picture of strain dynamics in thin α-Ga_2O_3 layers.

In-situ HRXRD analysis

To overcome this discrete, *ex-situ* approach we continued to perform the *in-situ* experiments, in which we continuously monitored the formation of strain and its relief for both orientations [0001] and [10$\bar{1}$0] *in-situ* during growth. After being mounted on a substrate holder, the substrate was transfered into the load-lock chamber, which was then pumped to a high vacuum of around 10^{-8} mbar. Since the substrate has been exposed to air during the preparation process, it probably absorbs undesirable water molecules on the surface. A degas process, at 473 K for 30 min, evaporated the water from the surface. Then the substrate was transfered via preparation chamber, transfer chamber, and finally mounted in the growth chamber, in which the substrate holder In the growth of such a compound material, the oxygen was supplied by a RF plasma cavity, whereas gallium was evaporated from a hot-lip effusion cell. We have chosen a plasma power of 400 W at a constant oxygen flux of 0.4 sccm. Crucible, hot-lip and substrate temperatures were set to 1023, 1173 and 873 K respectively, yielding a comparatively small Ga_2O_3 growth rate of about 2.3 Å/min, in an oxygen-rich condition.

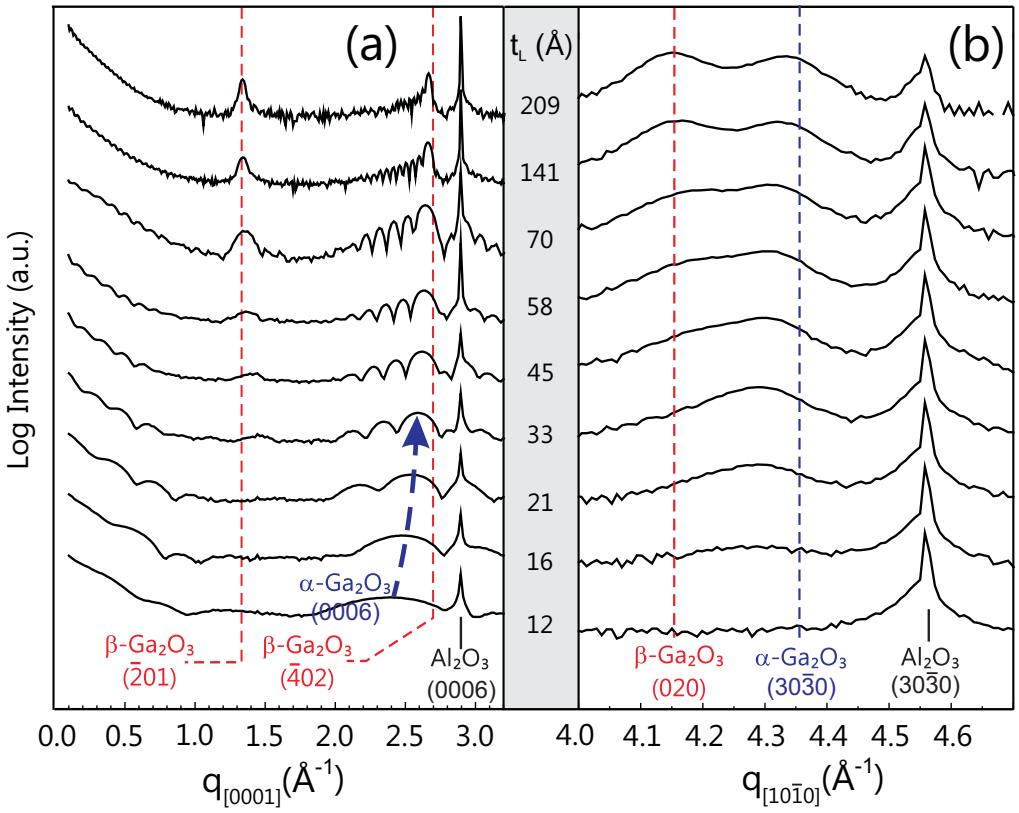

Figure 6.9 *In-situ* probe of the intensity (a) along the crystal truncation rod taken during the deposition of Ga_2O_3 on c-plane sapphire, and (b) along the $[10\bar{1}0]$ in-plane direction. Straight dashed lines (blue and red) mark the expected positions for contributions from bulk α- and β-phase. The curved blue arrow line in (a) depicts a decreasing lattice parameter out-of-plane.

In this *in-situ* experiment, the thickness-dependent experimental diffraction curves along [0001] and $[10\bar{1}0]$, as plotted in figure 6.9 (a, b), reveal a very similar growth sequence as derived via discrete steps *ex-situ* (figure 6.8) that the Ga_2O_3 layer first grows pseudomorphically, with the α-Al_2O_3, in α-phase, however later in the $(\bar{2}01)$-oriented β-phase. In particular they disclose the turning point (t_L=33 Å), at which thickness the film continues to grow as β-phase instead of α-phase. It is clearly seen that when the epitaxial layer thickness is smaller than 33 Å, as derived by the XRR fringes, only one reflection from the α-Ga_2O_3 (0006) plane emerges on the left side of the substrate (0006) diffraction peak. As the layer grows to a certain thickness between 21 Å and 33 Å, the β-Ga_2O_3 $(\bar{2}01)$ diffraction peak starts to be measurable in the out-of-plane CTR, as seen in Fig 6.9 (a). On the other hand, both α- and β-phase contributions are also well-separated in the selected $[10\bar{1}0]$ in-plane direction, figure 6.9 (b). At the initial state of growth, the α-phase $(30\bar{3}0)$ diffraction peak is probed on the left side of the substrate peak, as predicated by the larger lattice parameter, then as

the layer grows thicker, a "shoulder" shows up on the further left position. This "shoulder" is the β-Ga_2O_3 (020) contribution, and it becomes even more intense as the layer being deposited.

This part reveals the growing phase change from α-Ga_2O_3 to β-Ga_2O_3 on pristine *c*-plane α-Al_2O_3 substrates. The meta-stable α-phase only exists in the first few MLs, then as the layer grows thicker the depositing layer continues to grow in $(\bar{2}01)$-oriented β-Ga_2O_3, the thermodynamically more stable phase. It reveals the change of the growing phase by *in-situ* characterizations, demonstrating the strain relaxation during the growth. The lattice mismatch between the β-Ga_2O_3 (020) plane and the α-Al_2O_3 $(30\bar{3}0)$ plane is around 10%. Such a large mismatch, as compared with the α-Ga_2O_3, might be a reason for the formation of a few monolayers of α-Ga_2O_3, which here bridges the lattices of β-Ga_2O_3 and α-Al_2O_3 as an intermediate buffer layer.

Rotational domains in the $(\bar{2}01)$-oriented β-Ga_2O_3 layer

In addition to the one-dimensional diffraction intensity profiles, we have also measured the two-dimensional (2D) in-plane diffraction maps of the sample *in-situ*, in order to have more details of the structure change during growth. Since the epitaxial layer grown on *c*-plane sapphire substrate, more specifically the β-Ga_2O_3, has been found to contain in-plane rotational domains, the in-plane reciprocal space map serves as a proper fingerprint of layer structure.

The growth is carried out on *c*-plane sapphire substrate with exactly the same growth parameters as the experiment presented in figure 6.9. The in-plane diffraction measurement is carried out in a GID geometry, and it scans over an area defined by (0.5 0 0), (3.2 0 0), 0.5 $\overline{3.2}$ 0), and (3.2 $\overline{3.2}$ 0), 4 points in the reciprocal space. In particular, this area covers two types of diffraction, namely $(30\bar{3}0)$ and $(11\bar{2}0)$. During the first reciprocal space mapping (RSM) of the pristine substrate as plotted in figure 6.10 (a), the substrate was kept in the growth condition except for the closed gallium effusion cell shutter. This substrate map clearly shows the in-plane $(30\bar{3}0)$, $(3\bar{3}00)$, $(2\bar{1}\bar{1}0)$, and $(1\bar{2}10)$ diffraction peaks from the *c*-plane α-Al_2O_3. These contributions from the substrate serve as references for the subsequent deposited Ga_2O_3 film.

After the first mapping, the growth was started by introducing the gallium flux onto the substrate till the layer thickness amounted to around 1.5 nm, as measured by the XRR fringes. The reciprocal map at this Ga_2O_3 thickness, in figure 6.10 (b), already distinctly displays the diffraction intensity from the pseudomorphic

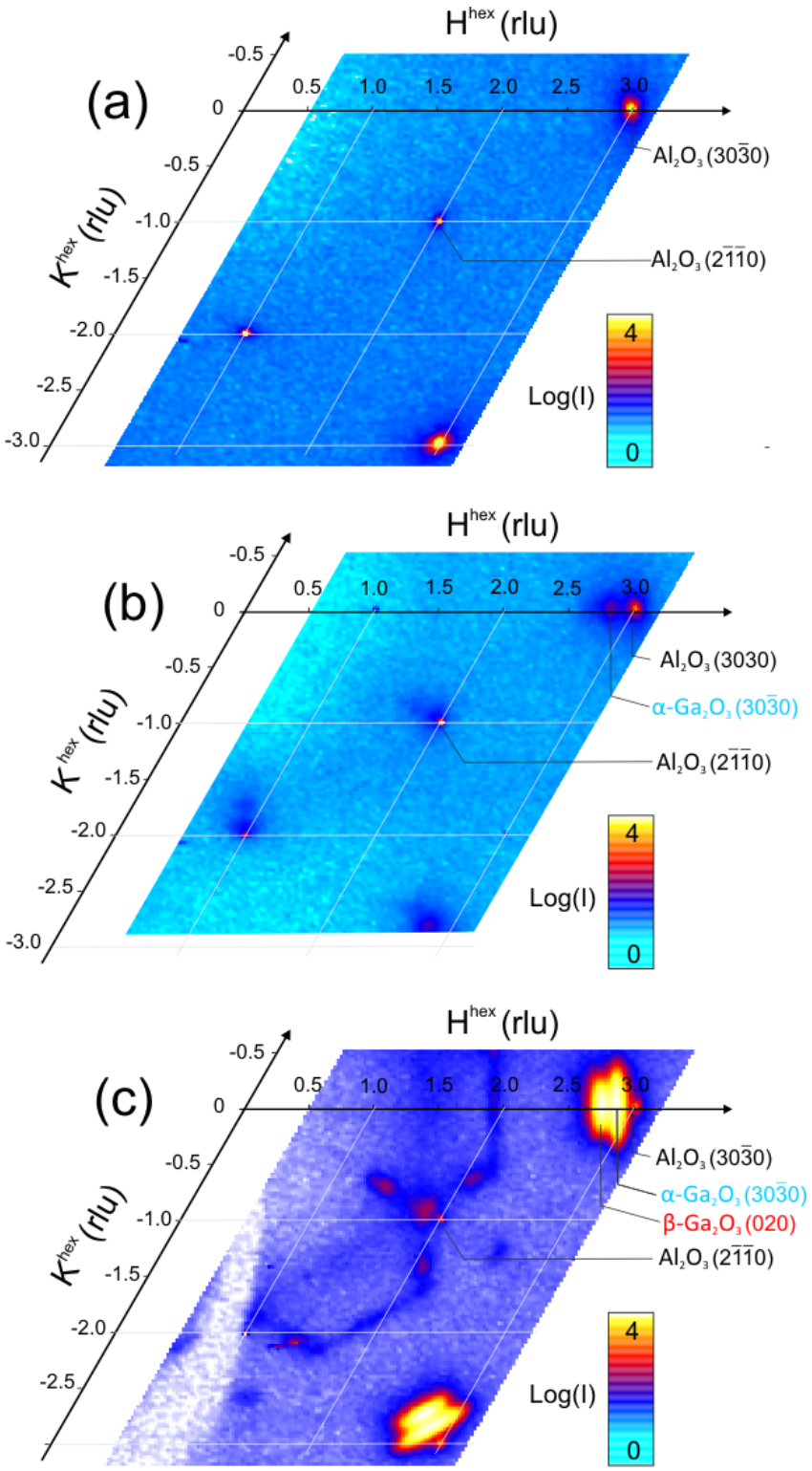

Figure 6.10 *In-situ* GID maps of the same sample after different growth thicknesses: the pristine *c*-plane oriented α-Al_2O_3 substrates before growth (a), approximately 1.5 nm growth (b), and around 18.6 nm post-growth (c).

grown α-Ga_2O_3 on the smaller $|\vec{q}|$ side of the substrate diffractions [closer to the (0000) point]. It can be distinctly observed that the deposited α-Ga_2O_3 was grown coherently with the substrate, and did not form other phases yet.

However, as the growth proceeded to a 18.6 nm thick layer, more complicated diffraction patterns were probed, as plotted in figure 6.10 (c). One obvious change is the broadening of α-Ga_2O_3 diffraction peaks, especially the $(30\bar{3}0)$ and $(3\bar{3}00)$ contributions which increased to a full width at half maximum (FWHM) of around 4°. This broadening in the azimuthal direction implies that the α-Ga_2O_3 layer was slightly twisted. Comparing plot (c) with (b), there are a plenty of extra diffraction patterns formed, and these contributions come from the top β-phase, since rather than α-Ga_2O_3, as already found from the figure 6.9, the more stable β-Ga_2O_3 continued to grow on top of the α-Ga_2O_3 monolayers. On the left side of the α-Ga_2O_3 $(30\bar{3}0)$ diffraction, a rather narrower diffraction pattern shows up, which belongs to the β-Ga_2O_3 (020) diffraction. A line profile through the β-Ga_2O_3 (020), α-Ga_2O_3 $(30\bar{3}0)$, and α-Al_2O_3 $(30\bar{3}0)$ diffractions, along the $[30\bar{3}0]$ direction is exactly the diffraction curve as shown in figure 6.9 (b) when the layer is around 20 nm.

In addition to the β-Ga_2O_3 (020) diffraction spot near the α-Ga_2O_3 $(30\bar{3}0)$, it is also found, by a 60° azimuthal offset, close to the α-Ga_2O_3 $(3\bar{3}00)$ contribution, showing a six-fold in-plane symmetry. Since β-Ga_2O_3 has a monoclinic structure, its (020) plane should present a two-fold symmetry in the azimuthal scan. This six-fold symmetry is interpreted by three-fold or six-fold in-plane rotational domains in the β-Ga_2O_3 film. However, since the β-Ga_2O_3 should follow the symmetry of the substrate, whereby the (0001) surface of α-Al_2O_3 is in a six-fold symmetry, the β-Ga_2O_3 film is expected to contain 6-fold in-plane domains. Therefore, here we can conclude the epitaxial relationship of the Ga_2O_3 grown on *c*-plane α-Al_2O_3, respectively along out-of-plane and in-of-plane directions (figure 6.11):

$$\alpha\text{-}Al_2O_3\ \{0001\} \parallel \alpha\text{-}Ga_2O_3\ \{0001\} \parallel \beta\text{-}Ga_2O_3\ \{\bar{2}01\}$$
$$\alpha\text{-}Al_2O_3\ \{10\bar{1}0\} \parallel \alpha\text{-}Ga_2O_3\ \{10\bar{1}0\} \parallel \beta\text{-}Ga_2O_3\ \{010\}$$

Near the α-Al_2O_3 $(2\bar{1}\bar{1}0)$ diffraction, the pseudomorphic α-Ga_2O_3 $(2\bar{1}\bar{1}0)$ diffraction remains the same as in figure 6.10 (b). However, there are features showing up around this α-Ga_2O_3 diffraction, aligned in a three-fold symmetry. Since these patterns appeared after the β-phase was already deposited, they might be

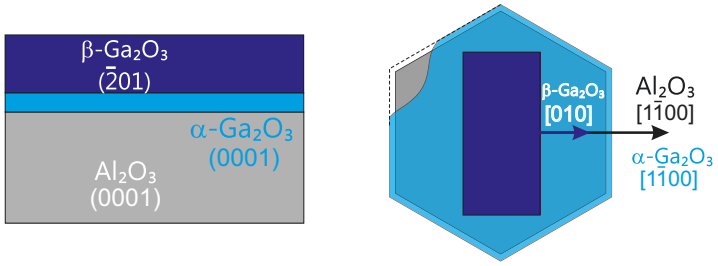

Figure 6.11 Sketch of the epitaxial relationship between α-Al_2O_3, α-Ga_2O_3 and β-Ga_2O_3, in out-of-plane (left) and in-plane directions (right).

related to the deposition of the β-Ga_2O_3 domains. One possible interpretation of these patterns is that they originate from the interface between the β-Ga_2O_3-domains, and are the interception of the CTRs at a small momentum close to L=0.

6.3 Growth and strain relaxation of single crystalline α-Ga_2O_3 thin film

It has been found that Ga_2O_3 grown on *c*-plane oriented sapphire substrates by a variety of epitaxial methodologies consists of a pseudomorphic initial α-Ga_2O_3 and on top of it a β-Ga_2O_3 film with in-plane rotational domains. However it would be preferential, for research purpose and device applications, to have an epitaxial layer containing only a single-phase film without domain formation. In particular, the large difference in bandgap, whereas α-Al_2O_3 is 8.8 eV and α-Ga_2O_3 is 5.3 eV, may pave the way towards two-dimensional electron gas.

As the large lattice mismatch and the oxygen arrangement might contribute to the formation of the $(\bar{2}01)$-oriented β-Ga_2O_3, therefore the study proceeds on α-Al_2O_3 substrates with other orientation, like *a*-, *m*-, and *r*-plane, because of the smaller lattice mismatch compared with the growth on *c*-plane sapphire (4.6%), and different surface oxygen arrangement in these planes. The lattice mismatches in different directions of α-Ga_2O_3 on the respective sapphire substrates are listed in table 6.1. Different planes in the α-Al_2O_3 unit cell are sketched in figure 6.12. In (a), $[11\bar{2}0]$ the surface normal of *a*-plane, and $[1\bar{1}00]$ the surface normal of *m*-plane are plotted, so as $[10\bar{1}2]$ the surface normal of *r*-plane in (b).

In this section, we report a study on the Ga_2O_3 growth on *a*-, *m*-plane, and *r*-plane α-Al_2O_3 substrates, focusing on the crystal phase evolution and the strain dynamics during the growth.

Substrate orientation	*a*-plane		*m*-plane		*r*-plane
Crystal direction	*c*-direction	*m*-direction	*c*-direction	*a*-direction	*a*-direction
Lattice mismatch	3.4%	4.6%	3.4%	4.6%	4.6%

Table 6.1 The lattice mismatches in different in-plane directions of α-Ga_2O_3 grown on α-Al_2O_3 in different surface orientations.

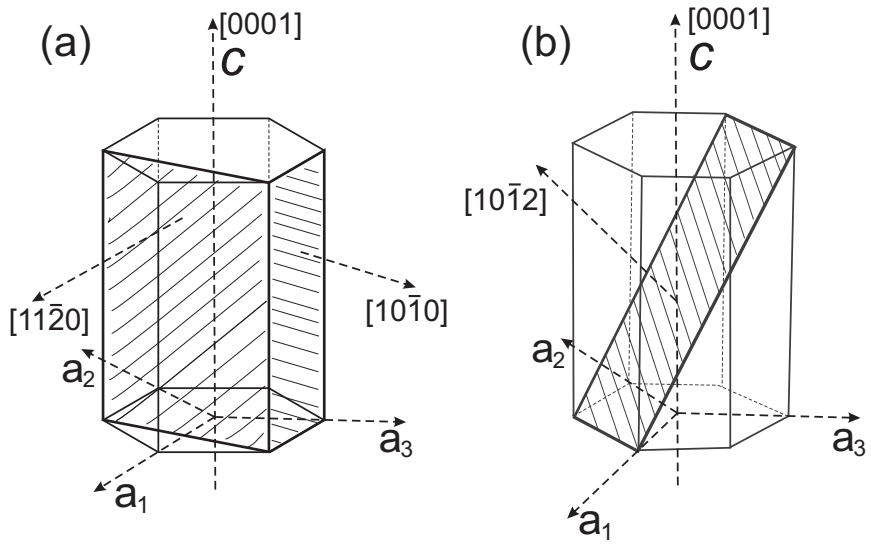

Figure 6.12 (11$\bar{2}$0), (10$\bar{1}$0) and (10$\bar{1}$2), namely a-, m-, and r-planes in the hexagonal structure.

6.3.1 Strain relaxation of high quality α-Ga_2O_3 grown on *a*-plane sapphire substrates

With respect to an *a*-plane α-Al_2O_3, the mismatch of Ga_2O_3 is reduced to 3.4% in [0001] direction and the (11$\bar{2}$0)-oriented surface possesses two-fold symmetry. The (11$\bar{2}$0) plane of both α-Al_2O_3 and α-Ga_2O_3 has an arrangement of surface oxygen atom sites compared the ($\bar{2}$01) plane of β-Ga_2O_3. Therefore, the stabilization of α-Ga_2O_3 might be easier to approach on *a*-plane sapphire.

We have performed a preliminary growth experiment of α-Ga_2O_3 on *a*-plane sapphire substrate, and after growth both out-of-plane and in-plane diffractions were measured. Meanwhile the growth parameters were kept the same as the growth on the *c*-plane substrate described in the previous section. As shown in figure 6.13 (a), the α-Ga_2O_3 (11$\bar{2}$0) diffraction was distinctly observed after the growth, and there was not any β-phase contribution probed. In the [0006] in-plane direction (b), the diffraction shows that the α-Ga_2O_3 (0006) plane is al-

most relaxed, and follows the symmetry of the substrate. The azimuthal FWHM of the α-Ga_2O_3 (0006) peak is around 1.2°, which is smaller than the FWHM of α-Ga_2O_3 in-plane peak grown on *c*-plane substrate, and indicates a higher crystal quality of the film for this heteroepitaxial growth. As calculated from the Kiessig fringes, the layer thickness is 7 nm, which is much thicker than the film thickness of α-Ga_2O_3 on *c*-plane sapphire substrates (cf. $t_c = 3.3$ nm). This initial experiment has indicated that α-Ga_2O_3 can be stabilized on *a*-plane sapphire substrate to a larger thickness.

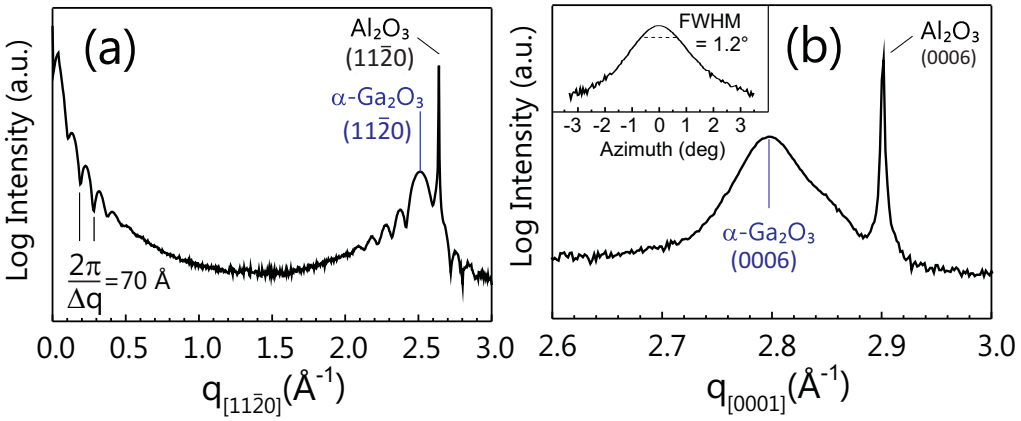

Figure 6.13 The diffraction profiles along the out-of-plane [11$\bar{2}$0] (a), and in-plane [0001] direction (b) of the α-Ga_2O_3 deposited on α-Al_2O_3 substrate. The (0006) diffraction rocking curve is the inset in (b).

in-situ HRXRD characterziations

In a more complementary experiment we have therefore proceeded the growth study on *a*-plane sapphire substrate with *in-situ* HRXRD characterizations. The *in-situ* diffraction experiments, figure 6.14, are showing the dynamics of (a) the out-of-plane strain, i.e. along [11$\bar{2}$0], and its kinematic simulation. It exhibits that the diffraction peak of the tensile strained α-Ga_2O_3 (11$\bar{2}$0) gradually shifts towards the unstrained diffraction position indicating a strain relief during the growth. The kinematic simulation of the diffraction in (a) agrees very well with the experiment, and gives a quantitative analysis on the thickness and strain status of the epitaxial film. Even at a film thickness of 143 Å, which is 4 times of the critical thickness on c-plane sapphire, the diffraction pattern depicts pronounced thickness oscillations in the reflection and diffraction, figure 6.14 (a). The in-plane strain status is measured in [0001] and [10$\bar{1}$0] directions, individually plotted in (b) and (c). In (c), the α-Ga_2O_3 (30$\bar{3}$0) plane is compressively

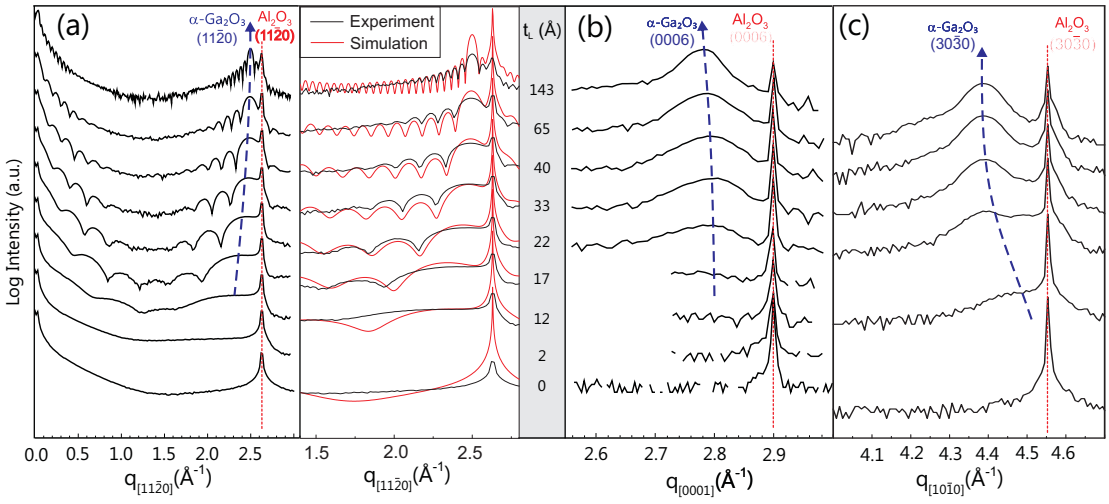

Figure 6.14 Intensity evolution along the out-of-plane crystal truncation rod, i.e. along $[11\bar{2}0]$, during the deposition of Ga_2O_3 on a-plane sapphire (a). The $(11\bar{2}0)$ diffraction peak of α-Ga_2O_3 appears on its bulk position left of the sapphire $(11\bar{2}0)$ contribution. Kinematic scattering simulations based on a system consisting of an a-plane sapphire substrate and a α-Ga_2O_3 layer of different thicknesses t_L and relaxation status. Grazing incidence diffraction curves along the substrate's $[0001]$ (b) and $[10\bar{1}0]$ (c) directions monitor the change of the in-plane strain in different planes.

strained at the initial growth, however its diffraction peak gradually shifts to smaller $|\vec{q}|$ value suggesting a strain relief process. On the other hand, unlike the α-Ga_2O_3 $(11\bar{2}0)$ and $(30\bar{3}0)$ diffractions experiencing a strain relaxation, the in-plane (0006) diffraction peak in (b) stays almost constant around the strain free position, as indicated by the blue dashed line. The shifting of the curves has described an anisotropic strain relief feature during the growth. Later in figure 6.16, it will be discussed in a more quantitative way.

Figure 6.15 (a) presents its in-plane GID map, in which α-Ga_2O_3 diffraction peaks and their corresponding substrate references are clearly plotted in the same radial direction demonstrating the coherent epitaxial relationship. Therefore, the GID map confirms the observation from the line scans in figure 6.15 (b) that the deposited α-Ga_2O_3 is in single-phase and continues the symmetry offered by the substrate without any in-plane rotational domain. Therefore, the mosaicity of the grown film consists of almost absent tilt but a quite large twist, derived from the FWHM of the $(11\bar{2}0)$ rocking curve $(41'')$ and the dependence of the (0006) peak $(1.2°)$ and the $(30\bar{3}0)$ peak $(1.4°)$. Azimuthal scans of the α-Al_2O_3 $(30\bar{3}0)$ diffraction, and the α-Ga_2O_3 $(30\bar{3}0)$ diffraction are as plotted in figure 6.15 (b).

The strain status of the α-Ga_2O_3 layer, as derived from its epi-layer Bragg peak shift, in three orthogonal directions during growth is plotted in figure 6.16. In the initial layers, a strong in-plane compressive strain (3.2 %) is accumulated

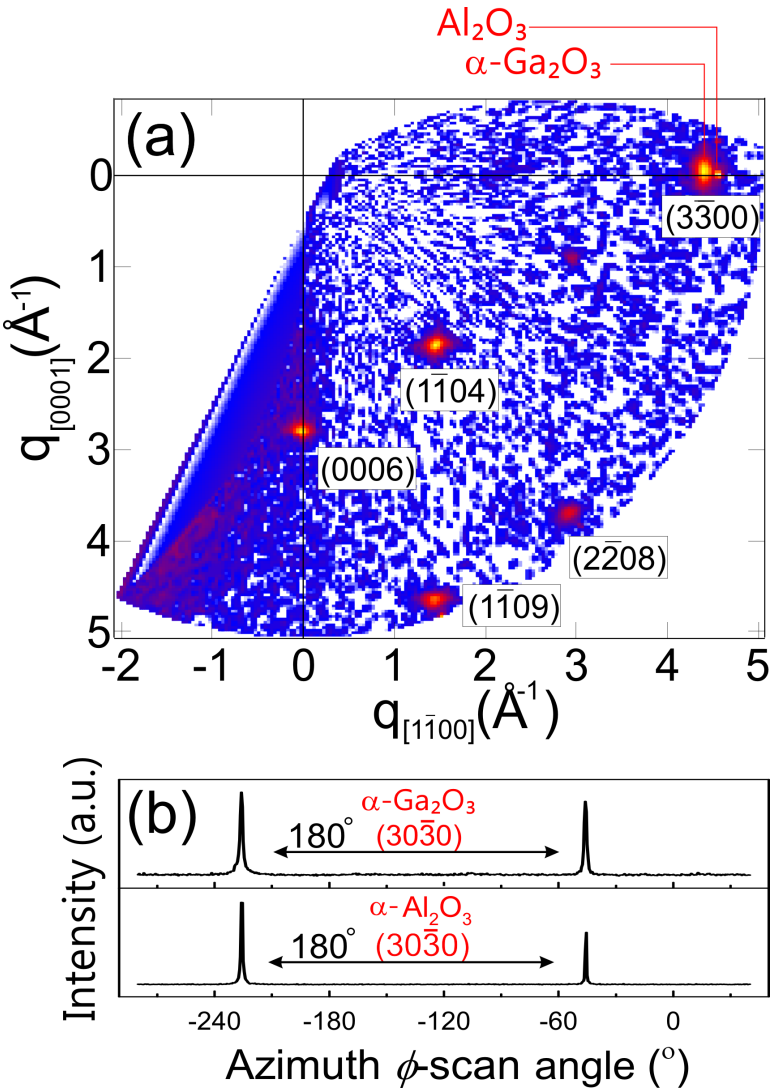

Figure 6.15 (a) *In-situ* GID map of the grown $(10\bar{1}0)$-oriented α-Ga_2O_3/α-Al_2O_3 heterostructure. The labeled indices represent both the sapphire substrate and the epi-layer. Since the x-ray penetration depth is small at the critical angle and the substrate contributions are very sharp, the map might not cover all the substrate peaks. One of them is the $Al_2O_3(3\bar{3}00)$. (b) The azimuth ϕ-scans of the in-plane Bragg peak reveals the epitaxial relation that Ga_2O_3 $[10\bar{1}0]$ $\parallel$ Al_2O_3 $[10\bar{1}0]$. Therefore, there is no in-plane rotational domains formed in the grown film.

in the $(10\bar{1}0)$ plane, as expected from the lattice mismatch, therefore generating an out-of-plane tensile strain (7.4 %). However, as the layer gradually grows to a thickness of around 30 Å, the strain relaxes to under 1 % dramatically in both directions. This fast strain relaxation is more likely to be a plastic strain relaxation and might cause misfit dislocations in the layer. Compared with the $(10\bar{1}0)$ plane, its orthogonal (0001) c-plane is almost strain free (less than 1 %) during the growth.

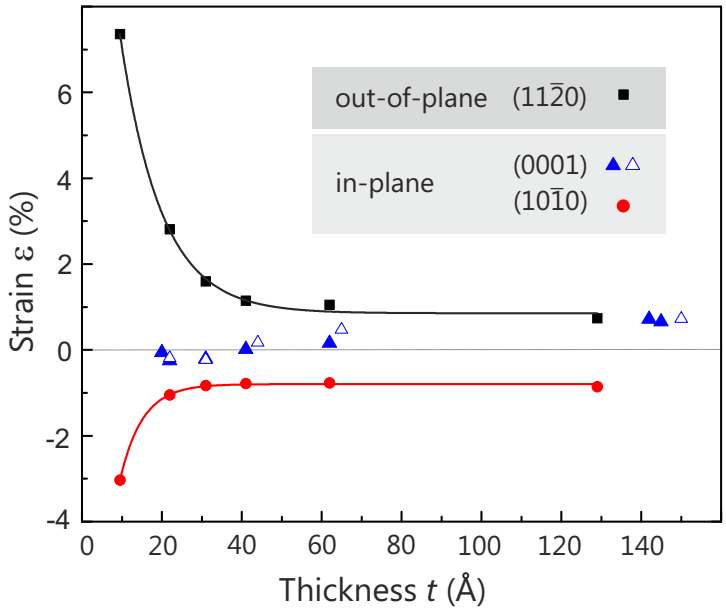

Figure 6.16 The strain relief of α-phase Ga_2O_3 in three orthogonal crystal planes, $(11\bar{2}0)$, $(10\bar{1}0)$ and (0001).

6.3.2 α-Ga_2O_3 stabilized on *m*-plane sapphire substrates

Single crystalline high quality α-Ga_2O_3 has been deposited coherently on *a*-plane sapphire substrate to a thickness of around 14 nm by plasma-assisted MBE. An interesting feature that has been observed during the growth is the anisotropically relaxed strain. To have a more complementary understanding in the α-Ga_2O_3 stabilization and strain relaxation, it is interesting to study the growth of α-Ga_2O_3 on *m*-plane substrates, focusing on the phase stabilization and strain status, like the growth study on *a*-plane substrates.

A preliminary growth has been carried out to probe the phase stabilization before the *in-situ* experiment. The deposition was performed with the same preparation process and growth parameters in case of growth on the *a*-plane substrates. After growth, the sample was characterized by *in-situ* symmetric HRXRD and azimuthal RHEED mapping. The x-ray diffraction intensity profile, in figure 6.17, presents the α-Ga_2O_3 $(30\bar{3}0)$ diffraction on the left side of the sapphire reference peak with periodic diffraction fringes. The thickness determined by the XRR fringes is approximately 9 nm, up to which the α-Ga_2O_3 is still in single-phase, and coherent with the substrate.

Because of the promising results as shown in figure 6.17, the experiment was proceeded with *in-situ* HRXRD measurements. Figure 6.18 presents x-ray diffraction curves as a function of the layer thickness derived from the XRR fringes.

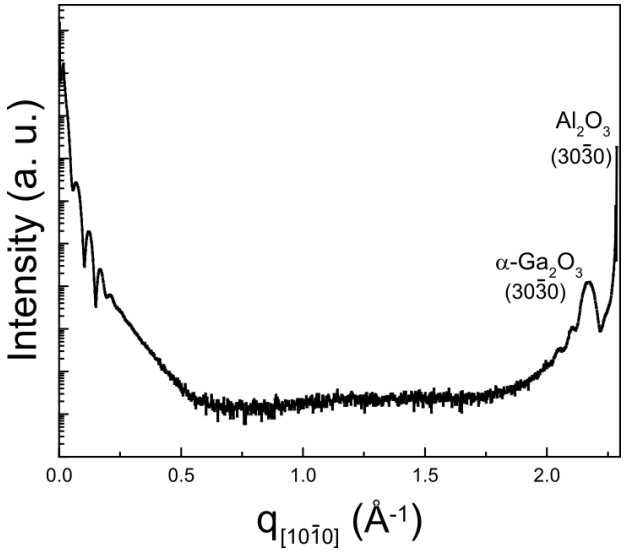

Figure 6.17 The diffraction profiles along the out-of-plane [10$\bar{1}$0].

The diffraction profiles are presented similar as in figure 6.14, however here [10$\bar{1}$0] is the out-of-plane direction, and the other are two in-plane directions. On the left side of figure 6.18 (a), it shows the intensity profile along the [10$\bar{1}$0] CTR and its evolution as the layer grows thicker from a pristine (10$\bar{1}$0)-oriented α-Al_2O_3 substrate. On the right side of (a), the experimental diffraction profiles are compared with a kinematic simulation in order to extract the strain of the epitaxial film quantitatively. Figure 6.18 (b) and (c) plot the diffraction curves in two orthogonal in-plane directions, respectively [11$\bar{2}$0] and [0001]. It demonstrates that the out-of-plane α-Ga_2O_3 (10$\bar{1}$0) peak gradually shifts from a tensile strain towards relaxation exhibiting a similar behavior as the growth on *a*-plane (figure 6.14), that the basal plane is under tensile strain at the beginning of the growth and then is continuously relaxed as the layer grows. In figure 6.18 (b), α-Al_2O_3 (11$\bar{2}$0) peak serves as a reference, whose left side appears the α-Ga_2O_3 (10$\bar{1}$0) peak pseudomorphically and it then smoothly shifts to smaller $|\vec{q}|$. It implies that α-Ga_2O_3 (10$\bar{1}$0) plane is compressively strained at the interface with the substrate, as expected from the lattice mismatch, however while the layer grows thicker, the strain is relaxed. Unlike (10$\bar{1}$0) and (11$\bar{2}$0) plane, the (0006) plane contribution remains almost at a constant position during the growth, as plotted in figure 6.18 (b), which is also observed on *a*-plane α-Al_2O_3.

The *in-situ* strain status in three orthogonal directions is quantitatively derived from the diffraction peak position and plotted in figure 6.19 as a function of layer thickness. At the beginning of the growth, the in-plane (11$\bar{2}$0) plane is compressively strained to around 1.7%, and induces an out-of-plane tensile strain of

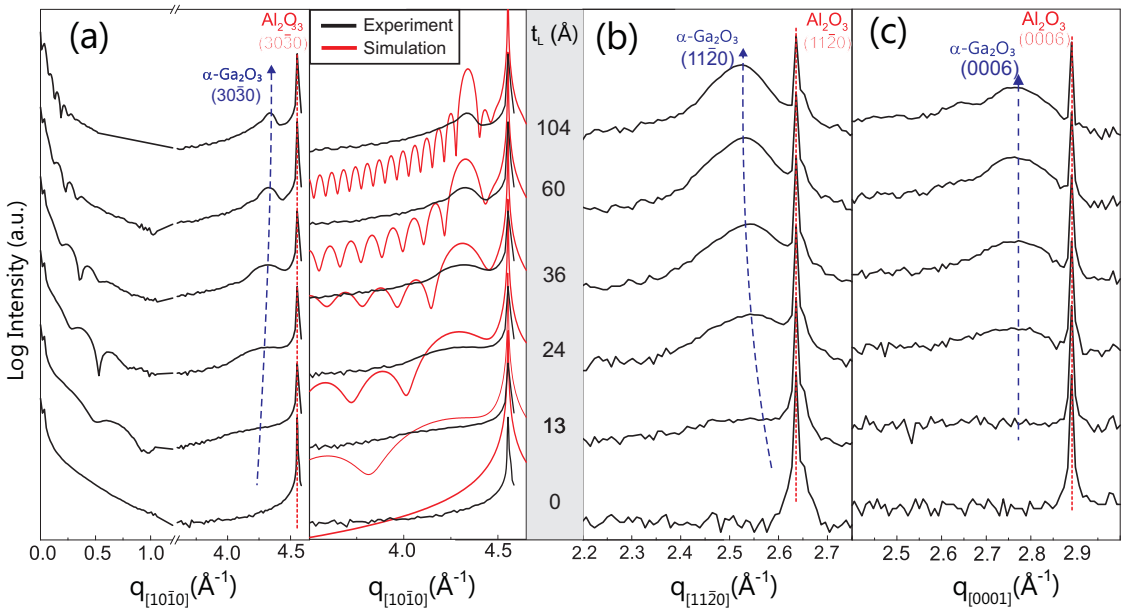

Figure 6.18 Intensity evolution along the out-of-plane crystal truncation rod, i.e. along $[10\bar{1}0]$, during the deposition of Ga_2O_3 on *m*-plane sapphire (a). The $(30\bar{3}0)$ diffraction peak of α-Ga_2O_3 appears on its bulk position left of the sapphire $(30\bar{3}0)$ contribution. Kinematic scattering simulations based on a system consisting of an m-plane sapphire substrate and a α-Ga_2O_3 layer of different thicknesses t_L and relaxation status. GID curves along the substrate's $[11\bar{2}0]$ (b) and [0001] (c) directions monitor the change of the in-plane strain in different planes.

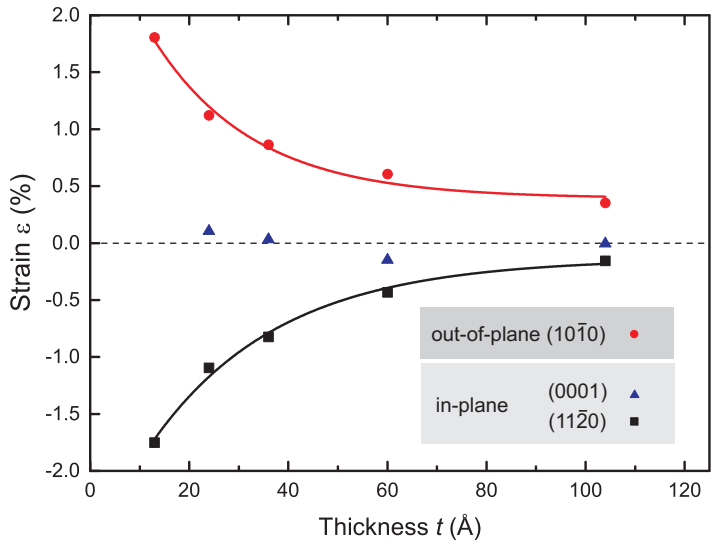

Figure 6.19 *In-situ* strain relief of α-phase Ga_2O_3 in three orthogonal crystal planes, $(11\bar{2}0)$, $(10\bar{1}0)$ and (0001).

approximately 1.8%. In contrast, the deformation of the (0001) plane is always less than 0.2% during the growth. This anisotropic strain relaxation is very similar with the observation on a-plane as shown in figure 6.16, that no matter on *a*-

or *m*-plane substrate the in-plane (0001) plane is already relaxed at the very initial state of the growth and shows an almost strain-free status during the growth, but the strain is more accumulated in other in-plane directions and resulting a tensile strain in the out-of-plane direction due to the Poisson effect. As it grows thicker, the thin film is relaxed in both out-of-plane and in-plane directions, as sketched in figure 6.19.

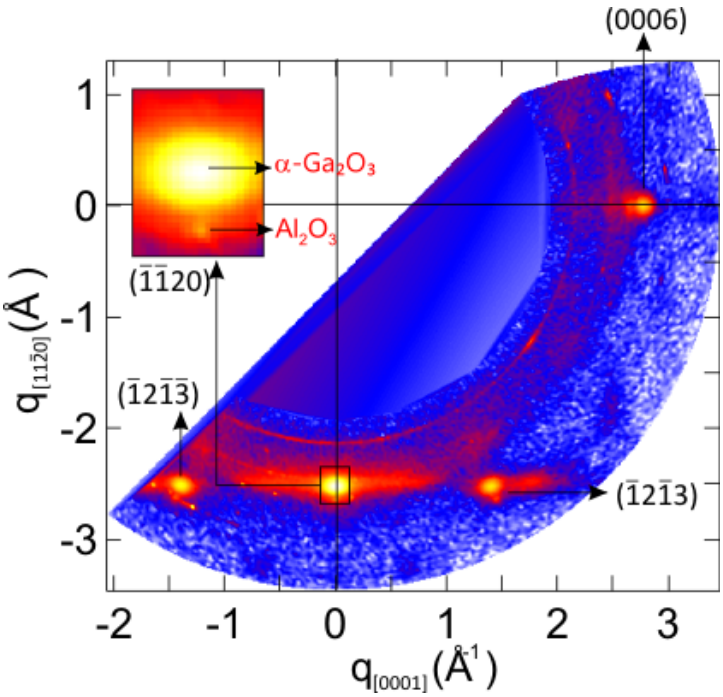

Figure 6.20 *In-situ* GID map of the grown $(10\bar{1}0)$-oriented α-Ga_2O_3/α-Al_2O_3 heterostructure. The labeled indices represent both the sapphire substrate and the epi-layer. Since the x-ray penetration depth is only a few MLs at the critical angle and the FWHM of substrate contributions are around tens of arcseconds, the map might not cover all the substrate peaks. One of them is the $Al_2O_3(3\bar{3}00)$.

Figure 6.20 presents the in-plane RSM of the α-Ga_2O_3 grown on *m*-plane sapphire substrate as probed by GID. The contributions from α-Ga_2O_3 (0006), $(\bar{1}\bar{1}20)$, $(\bar{1}2\bar{1}\bar{3})$, and $(\bar{1}2\bar{1}3)$ diffractions are well visible. Since the film is already around 10 nm, therefore the intensity from the α-Al_2O_3 substrate is relatively weak and not easy to be detected by the in-plane RSM. For example, the $(\bar{1}\bar{1}20)$ diffractions from both the substrate and the thin film are visible in the inset of figure 6.20, though the α-Al_2O_3 $(\bar{1}\bar{1}20)$ peak is sharp and weak.

The RSM confirms that the α-Ga_2O_3 is grown in a single-phase without rotational domains, and it follows the crystal orientation of the substrate. However the Bragg peak from the epitaxial layer is much more broader than the substrate peak and there is a certain amount of polycrystalline Ga_2O_3 within the layer,

probed as the rings in the map. Compared with α-Ga_2O_3 grown on *a*-plane sapphire substrate, its crystal quality is worse and might be improved by adjusting the growth parameters.

6.3.3 α-Ga_2O_3 stabilized on *r*-plane sapphire substrates

Though employing the same growth parameters, Ga_2O_3 still grows in different phases depending on the surface orientation of α-Al_2O_3 substrates, where β-Ga_2O_3 with rotational domains is deposited on *c*-plane, however α-Ga_2O_3 is found on *a*- and *m*-plane oriented α-Al_2O_3. To have a better understanding on the stabilization of different Ga_2O_3 phases on sapphire substrates, the experiment proceeded with the growth on the *r*-plane $(10\bar{1}2)$-oriented substrates. As sketched in figure 6.12 (b), the surface normal of *r*-plane $[10\bar{1}2]$ is in the same plane with [0001] and $[10\bar{1}0]$, therefore the amount of lattice mismatch is also between that of these two directions.

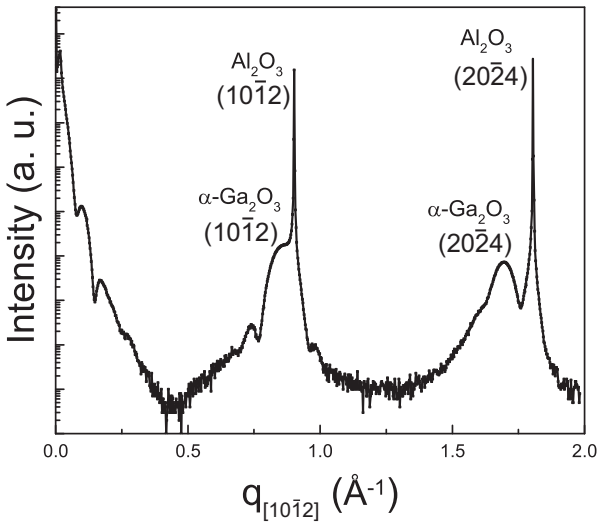

Figure 6.21 The diffraction profiles along the out-of-plane $[10\bar{1}2]$ proves the formation of coherently grown α-Ga_2O_3.

The growth was carried out with the same growth parameters as on *a*-plane and *m*-plane substrates. The out-of-plane diffraction in figure 6.21 (a) shows the α-Ga_2O_3 $(10\bar{1}2)$ and $(20\bar{2}4)$ contributions near the corresponding substrate peaks. In addition to the α-Al_2O_3 and α-Ga_2O_3 contribution, there is no intensity from other phases found. The thickness of the grown layer is around 3.8 nm as calculated by the XRR and XRD fringes. This growth shows that up to this thickness, Ga_2O_3 appears only in α-phase without rotational domain.

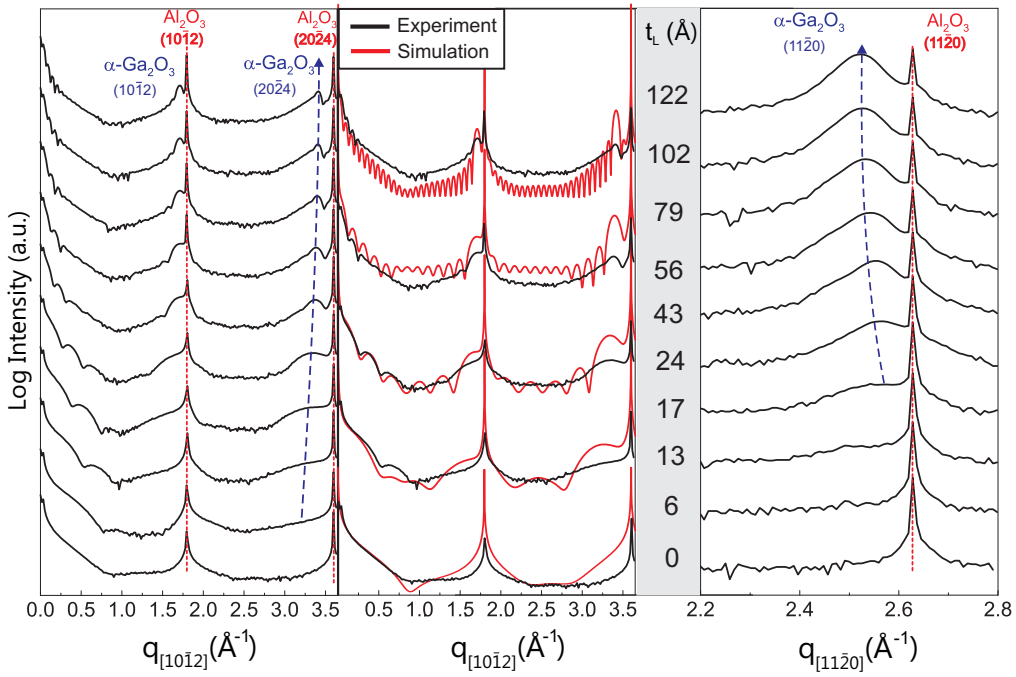

Figure 6.22 Intensity evolution along the out-of-plane crystal truncation rod, i.e. along [10$\bar{1}$2], during the deposition of Ga_2O_3 on r-plane sapphire (a). The (20$\bar{2}$4) diffraction peak of α-Ga_2O_3 appears on its bulk position left of the sapphire (20$\bar{2}$4) contribution. Kinematic scattering simulations based on a system consisting of a r-plane sapphire substrate and a α-Ga_2O_3 layer of different thicknesses t_L and relaxation status. The GID curves along the substrate's [11$\bar{2}$0] direction monitor the change of the in-plane strain in different planes (c).

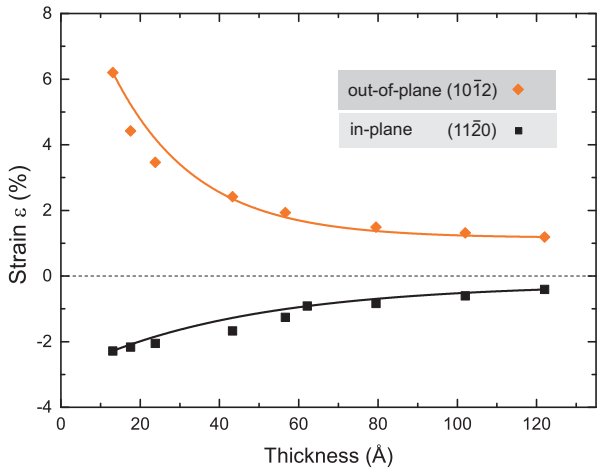

Figure 6.23 *In-situ* strain relief of α-phase Ga_2O_3 in the out-of-plane [10$\bar{1}$2] direction and in-plane (11$\bar{2}$0) direction.

Figure 6.22 (a) presents the *in-situ* (10$\bar{1}$2) diffraction curves in the out-of-plane direction, and on the right side their corresponding kinematic simulation (b). It is obviously noticed that the α-Ga_2O_3 (10$\bar{1}$2) and (20$\bar{2}$4) contributions appear on the left of the respective substrate peaks shortly after the growth starts (above

13Å). Meanwhile, the in-plane α-Ga_2O_3 ($11\bar{2}0$) diffraction emerges on the left side of α-Al_2O_3 ($11\bar{2}0$), which was probed in a grazing incidence geometry. The thickness of the heterostructure is calculated based on the XRR fringes. As the α-Ga_2O_3 layer grows thicker, its ($10\bar{1}2$) and ($20\bar{2}4$) diffractions shift towards the corresponding α-Al_2O_3 peaks, while the its in-plane ($11\bar{2}0$) diffraction gradually moves left to the strain-free position. On the right side of figure 6.22 (a), the experimental diffraction profiles are compared with a kinematic simulation in order to extract the strain status of the epitaxial film quantitatively. The plot clearly shows that up to a thickness of around 12 nm, there is no other phase probed rather the α-Ga_2O_3.

The derived *in-situ* strain status is plotted in figure 6.23. At the beginning of the growth, α-Ga_2O_3 is under a compressive strain of around 2.2% in the [$11\bar{2}0$] direction, as expected from the lattice mismatch with the sapphire substrate. The compressive strain, similar as the growth on other planes, induces a strong tensile strain, more than 6%, in the out-of-plane direction. As the α-Ga_2O_3 layer then grows thicker, the crystal is rapidly relaxed partially in these two probed directions in the first 4 nm.

6.4 Summary

This chapter has presented a comprehensive study on the phase modification and the strain dynamics of Ga_2O_3 during the growth on sapphire substrates with different surface orientations.

The growth on *c*-plane sapphire substrates shows the formation of monoclinic β-Ga_2O_3 consisting of in-plane rotational domains after a thin initial layer of the meta-stable α-Ga_2O_3. Because of the six-fold symmetry of the substrate, this ($\bar{2}01$)-oriented β-Ga_2O_3 film consists of in-plane six-fold rotational domains, which follow the epitaxial relationship that α-Ga_2O_3 ($1\bar{1}00$) $\parallel$ α-Ga_2O_3 ($1\bar{1}00$) $\parallel$ β-Ga_2O_3 (010). The HRXRD line scans and the RSMs have clearly proved this epitaxial relationship.

As mentioned, the lattice mismatch is around 4.6% in respective of lattice constant *a*. The strain caused by this lattice mismatch at the initial state of the growth might prohibit the formation of ($\bar{2}01$)-oriented β-Ga_2O_3, but temporally stabilize the α-Ga_2O_3 within the first few nm. However, as the layer grows thicker, the strain is relaxed rapidly, as shown in figure 6.8 and 6.9. The strain relaxation therefore reduces the *in-situ* lattice mismatch between α-Ga_2O_3 and β-Ga_2O_3. In addition to the lattice mismatch, the ($\bar{2}01$) plane in β-Ga_2O_3 also has a similar

oxygen atom arrangement as the (0001) plane of α-Ga_2O_3.[118, 119] Therefore, the thermodynamically more favorable β-Ga_2O_3 starts to grow on top of the *c*-plane α-Ga_2O_3. However, in other planes, such as *a*-, *m*-, and *r*-plane, the lattice mismatch is a little bit smaller (3.4% in *c* axis), and the surface atom arrangement is not in correspondence with any plane of β-Ga_2O_3. Therefore, the thermodynamically unfavorable α-Ga_2O_3 can be coherently grown on the sapphire substrate to more than 10 nm without the formation of β-Ga_2O_3.

The *in-situ* HRXRD results clearly depict the film thickness and strain evolution of the growing α-Ga_2O_3. With the help of the kinematic scattering simulation, it is possible to interpret the experimental results in a quantitative respect. For the single crystalline α-Ga_2O_3 grown sapphire substrates in different orientations, the strain status is plotted as a function of the layer thickness. It is found that the strain is anisotropically distributed in the in-plane directions for *m*- and *a*-plane α-Ga_2O_3, whereas the [0001] direction is almost strain-free, however accumulated in the orthogonal in-plane direction. The in-plane compressive strain induces a tensile strain in the out-of-plane direction as expected from Poisson's effect. However, as the layer grows thicker, the strain in both in-plane and out-of-plane directions is rapidly relaxed in the first a few nanometer. It is interesting to notice that sapphire, in a similar crystal structure, also has a harder *c*-axis than *a*-axis.[120] Therefore, this study helps to have a better understanding in the mechanical properties of the rhombohedral structure. Further study on the defect formation in the *a*-plane α-Ga_2O_3 layer, by electron microscopy, would be necessary for a deeper understanding in the strain relief process.

The growth of high quality single crystalline α-Ga_2O_3, especially *a*-plane α-Ga_2O_3, on the large bandgap sapphire substrate would be definitely interesting for the two-dimensional gas electronics. It can also serve as a substrate for further post growth with higher growth rate, such as MOCVD and Mist-CVD.

7 Summary and outlook

In this thesis, an *in-situ* study on the thermal expansion of bulk β-Ga_2O_3, the growth mode evolution during the β-Ga_2O_3 homoepitaxy, and the strain relaxation and the phase formation in the Ga_2O_3 heteroepitaxy has been reported. The CTEs of β-Ga_2O_3 are determined from RT to 1200 K, and appear anisotropic depending on the crystal directions. The (100)-oriented β-Ga_2O_3 homoepitaxy is observed in a 2D layer-by-layer growth mode with the formation of twin domains. In heteroepitaxy, α-Ga_2O_3 can be stabilized on the sapphire substrates in different surface orientations (*a*-, *m*-, and *r*-plane) except for *c*-plane, and the strain within the epitaxial thin film is anisotropically distributed and rapidly relaxed during the growth.

Summary

β-Ga_2O_3 is a promising TSO material for a wide variety of applications, however its thermal expansion property above 700 K has not been comprehensively studied. Therefore, we carried out an investigation on the CTEs of β-Ga_2O_3 from RT to 1200 K. The lattice parameters *a*, *b*, and *c* of a single-crystalline β-Ga_2O_3 bulk were precisely probed by synchrotron-based HRXRD at different temperatures. These sets of measured lattice parameters are well interpreted by the fittings based on the Einstein model. It is found that the absolute values of CTEs are anisotropic in different directions that the CTE in *a* direction is approximately only half of the CTEs along *b* and *c* directions in the probed temperature range. It also proves that the CTEs are not constant with the on-site temperature. Instead, the CTEs gradually increase with the temperature and get saturated near 1200 K. The results have shown good agreement with related studies in the thermal conductivity and the phonon modes of β-Ga_2O_3. With respect to the heteroepitaxy, the CTE results can help to predict the on-site lattice mismatch for β-Ga_2O_3 on different substrates at a high growth temperature.

The growth mode of the (100)-oriented β-Ga_2O_3 homoepitaxy in MBE has been well studied by the means of various *in-situ* and *ex-situ* characterizations. It

is found that the growth on this orientation is carried out in a 2D layer-by-layer mode. The growth starts with the nucleation of small islands on the substrate surface. These nuclei are periodically distributed along the *c*-direction and elongated in *b*-direction. The islands as shown in the HRTEM image at the (010) cross-section have roughly 10 nm width and 0.6 nm height, which are in correspondence with its surface morphology probed by AFM and size of the twin domains in the epitaxial film. The very pronounced RHEED specular beam intensity oscillation, the determined epitaxial layer thickness, and the measured surface morphology together depict a picture of the growth process of (100)-oriented β-Ga_2O_3 homoepitaxy. The growth starts with the formation of nuclei on the fresh substrate surface, then the nuclei coalesce to form a complete ML with the height of half unit cell. Afterwards, the next ML starts the nucleation on the previous coalesced layer. However, because of the double positioning of the adjacent molecules, some of the nuclei are formed in the opposite crystal orientation in respect of axis *c*. These minus *c* oriented nuclei proceed to grow and then form the twin domains in epitaxial film. This work helps us to understand the formation of the defects in the (100)-oriented β-Ga_2O_3 thin film grown in MBE and allows to very precisely control the layer thickness according to the RHEED oscillations.

For device applications, the heterostructure of materials with different bandgap plays an important role, therefore it is essential to study the heteroepitaxy of Ga_2O_3 on substrates like sapphire. It is found that the rhombohedral α-Ga_2O_3 is only stable in the first a few MLs on *c*-plane sapphire, on which the $(\bar{2}01)$-oriented β-Ga_2O_3 proceeds to grow, however on the sapphire substrates in other orientations the α-Ga_2O_3 can be coherently grown in single crystal above 10 nm. During the heteroepitaxial growth, it is observed that the lattice mismatch induced strain is anisotropically distributed in different in-plane directions, and relaxes rapidly in the first 3 nm. Such a fast strain relaxation in the α-Ga_2O_3 reduces the mismatch against β-Ga_2O_3, and the $(\bar{2}01)$-oriented β-Ga_2O_3 starts to grow on the *c*-plane α-Ga_2O_3, which has also a similar oxygen arrangement as the $(\bar{2}01)$ plane of β-Ga_2O_3. However, on other orientations α-Ga_2O_3 can proceed to grow coherently with the sapphire substrate without the formation of β-Ga_2O_3. This stabilization is attributed to the smaller lattice mismatch and different surface symmetry in other planes than the *c*-plane.

Outlook

The CTEs of β-Ga_2O_3 in principle can be measured to a further extended temperature range with the help of another mounting method which assures a stable mounting above 1200 K. The PHARAO beamline has shown a great possibility for the determination of CTEs in the wide range of temperature, therefore it might help to probe the thermal expansion of other materials. As for the homoepitaxial growth of (100)-oriented β-Ga_2O_3, it has been found in the MOCVD growth, a mis-orientation of around 6 ° induces a step-flow growth mode, in which the twin domains are difficult to form. The influence of the substrate miscut on the formation of twins in the MBE growth would be highly interesting in the future. The heteroepitaxial α-Ga_2O_3 on *a*-plane sapphire substrate appears good crystal quality and improved stability. The structure and strain of this layer have been well studied, however on to way to either research or industry applications, one importance is to manipulate the electrical properties. Therefore, more study on the doping of the heteroepitaxial α-Ga_2O_3 thin film would be an important issue.

Bibliography

[1] Roy R, Hill V G and Osborn E F 1952 Polymorphism of Ga_2O_3 and the System Ga_2O_3—H_2O *J. Am. Chem. Soc.* 74 719

[2] Zhang J, Xia C, Deng Q, Xu W, Shi H, Wu F and Xu J 2006 Growth and characterization of new transparent conductive oxides single crystals β-Ga_2O_3: Sn *J. Phys. Chem. Solids* 67 1656

[3] Suzuki N, Ohira S, Tanaka M, Sugawara T, Nakajima K and Shishido T 2007 Fabrication and characterization of transparent conductive Sn-doped β-Ga_2O_3 single crystal *Phys. Status Solidi C* 4 23110

[4] Víllora E G, Shimamura K, Yoshikawa Y, Ujiie T and Aoki K 2008 Electrical conductivity and carrier concentration control in β-Ga_2O_3 by Si doping *Appl. Phys. Lett.* 92 202120

[5] Ahmadi E, Koksaldi O S, Kaun S W, Oshima Y, Short D B, Mishra U K and Speck J S 2017 Ge doping of β-Ga_2O_3 films grown by plasma-assisted molecular beam epitaxy *Appl. Phys. Express* 10 041102

[6] Shinji N, Toshihiro M, Syuhei T and Yoshihiro K 2013 Deep ultraviolet photodiodes based on β-Ga_2O_3/SiC heterojunction *Appl. Phys. Lett.* 103 072105

[7] Oshima T, Okuno T and Fujita S 2007 Ga_2O_3 thin film growth on c-plane sapphire substrates by molecular beam epitaxy for deep-ultraviolet photodetectors *Jpn. J. Appl. Phys.* 46 7217

[8] Oshima T, Okuno T, Arai N, Suzuki N, Ohira S and Fujita S 2008 Vertical solar-blind deep-ultraviolet Schottky photodetectors based on β-Ga_2O_3 substrates *Appl. Phys. Express* 1 011202

[9] Fleischer M, Haurierder W and Meixner H 1990 Stability of semiconducting gallium oxide thin films *Thin Solid Films* 190 93

[10] Lin H J, Gao H and Gao P X 2017 UV-enhanced CO sensing using Ga_2O_3-based nanorod arrays at elevated temperature *Appl. Phys. Lett.* 110 043101

[11] Lin H J, Baltrus J P, Gao H, Ding Y, Nam C Y, Ohodnicki P and Gao P X 2016 Perovskite nanoparticle-sensitized Ga_2O_3 nanorod arrays for CO detection at high temperature *ACS Appl. Mater. Interfaces* 8 8880

[12] Ogita M, Higo K, Nakanishi Y and Hatanaka Y 2001 Ga_2O_3 thin film for oxygen sensor at high temperature *Appl. Surf. Sci.* 175 721

[13] Chen C-C and Chen C-C 2004 Morphology and electrical properties of pure and Ti-doped gas-sensitive Ga_2O_3 film prepared by rheotaxial growth and thermal oxidation *J. Mater. Res.* 19 1105

[14] Lampe U, Fleischer M and Meixner H 2017 Lambda measurement with Ga_2O_3 *Sens. Actuators B Chem.* 17 187

[15] Green A J, Chabak K D, Heller E R, Fitch R C, Baldini M, Fiedler A, Irmscher K, Wagner G, Galazka Z, Tetlak S E, Crespo A, Leedy K and Jessen G H 2016 3.8-MV/cm breakdown strength of MOVPE-grown Sn-doped-Ga_2O_3 MOSFETs *IEEE Electron Device Lett.* 37 902

[16] Green A J, Chabak K D, Baldini M, Moser N, Gilbert R, Fitch R C, Wagner G, Galazka Z, Mccandless J, Crespo A, Leedy K and Jessen G H 2017 β-Ga_2O_3 MOSFETs for radio frequency operation *IEEE Electron Device Lett.* 38 790

[17] Higashiwaki M, Sasaki K, Kuramata A, Masui T and Yamakoshi S 2012 Gallium oxide (Ga_2O_3) metal-semiconductor field-effect transistors on single-crystal β-Ga_2O_3 (010) substrates *Appl. Phys. Lett.* 100 013504

[18] Chabak K D, Moser N, Green A J, Walker Jr. D E, Tetlak S E, Heller E, Crespo A, Fitch R, McCandless J P, Leedy K, Baldini M, Wagner G, Galazka Z, Li X, and Jessen G, 2016 Enhancement-mode Ga_2O_3 wrap-gate fin field-effect transistors on native (100) β-Ga_2O_3 substrate with high breakdown voltage *Appl. Phys. Lett.* 109 213501

[19] Higashiwaki M, Sasaki K, Kamimura T, Wong M H, Krishnamurthy D, Kuramata A, Masui T and Yamakoshi S 2013 Depletion-mode Ga_2O_3

metal-oxide-semiconductor field-effect transistors on β-Ga_2O_3 (010) substrates and temperature dependence of their device characteristics *Appl. Phys. Lett.* 103 123511

[20] Matsuzaki K, Yanagi H, Kamiya T, Hiramatsu H, Nomura K, Hirano M and Hosono H 2006 Field-induced current modulation in epitaxial film of deep-ultraviolet transparent oxide semiconductor Ga_2O_3 *Appl. Phys. Lett.* 88 092106

[21] Higashiwaki M, Sasaki K, Kuramata A, Masui T and Yamakoshi S 2014 Development of gallium oxide power devices *Phys. Status Solidi A* 211 21

[22] Weiser H B and Milligan W O 1940 An electron diffraction study of hydrous oxides amorphous to x-rays *J. Phys. Chem.* 44 1081

[23] Nishinaka H, Tahara D, Morimoto S and Yoshimoto M 2017 Epitaxial growth of α-Ga_2O_3 thin films on a-, m-, and r-plane sapphire substrates by mist chemical vapor deposition using α-Fe_2O_3 buffer layers *Mater. Lett.* 205 28

[24] Shinohara D and Fujita S 2008 Heteroepitaxy of corundum-structured α-Ga_2O_3 thin films on α-Al_2O_3 substrates by ultrasonic mist chemical vapor deposition *Jpn. J. Appl. Phys.* 47 7311

[25] Cheng Z, Hanke M, Vogt P, Bierwagen O and Trampert A 2017 Phase formation and strain relaxation of Ga_2O_3 on c-plane and a-plane sapphire substrates as studied by synchrotron-based x-ray diffraction *Appl. Phys. Lett.* 111 162104

[26] Williams D B and Carter C B 1996 Transmission electron microscopy III: imaging *Springer* IBSN 0-306-45247-2

[27] Bellitto V 2012 Atomic force microscopy—imaging, measuring and manipulating surfaces at the atomic scale *InTech (open source)*

[28] Yoshioka S, Hayashi H, Kuwabara A, Oba F, Matsunaga K and Tanaka I 2007 Structures and energetics of Ga_2O_3 polymorphs *J. Phys.: Condens. Matter* 19 346211

[29] Kroll P, Dronskowski R and Martin M 2005 Formation of spinel-type gallium oxynitrides: a density-functional study of binary and ternary phases in the system Ga-O-N *J. Mater. Chem.* 15 3296

[30] He H, Blanco M A and Pandey R 2006 Electronic and thermodynamic properties of β-Ga_2O_3 *Appl. Phys. Lett.* 88 261904

[31] von Wenckstern H 2017 Group III sesquioxides: growth, physical properties and devices *Adv. Electron. Mater.* 3 1600350

[32] Åhman J, Svensson G and Albertsson J 1996 A reinvestigation of β-gallium oxide *Acta Cryst.* C52 1336

[33] Geller S 1960 Crystal structure of β-Ga_2O_3 *J. Chem. Phys.* 33 676

[34] Cuong N D, Park Y W and Yoon S G 2009 Microstructural and electrical properties of Ga_2O_3 nanowires grown at various temperatures by vapor-liquid-solid technique *Sens. Actuators, B* 140 240

[35] Marezio M and Remeika J P 1967 Bond length in the α-Ga_2O_3 structure and the high pressure phase of $Ga_{2-x}Fe_xO_3$ *J. Chem. Phys.* 46 1862

[36] Fujita S, Oda M, Kaneko K and Hitora T 2016 Evolution of corundum-structured III-oxide semiconductors: growth, properties, and devices *Jpn. J. Appl. Phys.* 55 1202A3

[37] Playford H Y, Hannon A C, Tucker M G, Dawson D M, Ashbrook S E, Kastiban R J, Sloan J and Walton R I 2016 Characterization of structural disorder in γ-Ga_2O_3 *J. Phys. Chem. C* 118 16188

[38] Kohn J A, Katz G and Broder J D 1957 Characterization of β-Ga_2O_3 and its alumina isomorph, θ-Al_2O_3 *Am. Mineral.* 42 398

[39] Pearton S J, Yang J, Cary IV P H, Ren F, Kim J, Tadjer M and Mastro M A 2018 A review of Ga_2O_3 materials, processing, and devices *Appl. Phys. Rev.* 5 011301

[40] Oshima T, Nakazono T, Mukai A and Ohtomo A 2012 Epitaxial growth of γ-Ga_2O_3 films by mist chemical vapor deposition *J. Cryst. Growth* 359 60

[41] He H, Orlando R, Blanco M A and Pandey R 2006 First-principles study of the structural, electronic, and optical properties of Ga_2O_3 in its monoclinic and hexagonal phases *Phys. Rev. B* 74 195123

[42] Pauling L and Hendricks S B 1925 The crystal structure of hematite and corundum *J. Am. Chem. Soc.* 47 781

[43] Kawaharamura T, Dang G T and Furuta M 2012 Successful growth of conductive highly crystalline Sn-doped α-Ga_2O_3 thin films by fine-channel mist chemical vapor deposition *Jpn. J. Appl. Phys.* 51 040207

[44] Kumaran R, Tiedje T, Webster S E, Penson S and Li W 2010 Epitaxial Nd-doped α-$(Al_{1-x}Ga_x)_2O_3$ films on sapphire for solid-state waveguide lasers *Opt. Lett.* 35 3793

[45] Schewski R, Wagner G, Baldini M, Gogova D, Galazka Z, Schulz T, Remmele T, Markurt T, von Wenckstern H, Grundmann M, Bierwagen O, Vogt P and Albrecht M 2015 Epitaxial stabilization of pseudomorphic α-Ga_2O_3 on sapphire (0001) *Appl. Phys. Express* 8 011101

[46] Remeika J P and Marezio M 1966 Growth of α-Ga_2O_3 single crystals at 44 kbar *Appl. Phys. Lett.* 8 87

[47] Foster L M and Stumpf C H 1951 Analogies in the gallia and alumina systems. The preparation and properties of some low-alkali gallates *J. Am. Chem. Soc.* 73 1590

[48] Tadjer M J, Mastro M A, Mahadik N A, Currie M, Wheeler V D, Freitas Jr. J A, Greenlee J D, Hite J K, Hobart K D, Eddy Jr. C R and Kub F J 2016 Structural, optical, and electrical characterization of monoclinic β-Ga_2O_3 grown by MOCVD on sapphire substrates *J. Electron. Mater.* 45 2031

[49] Ueda O, Ikenaga N, Koshi K, Iizuka K, Kuramata A, Hanada K, Moribayashi T, Yamakoshi S and Kasu M 2016 Structural evaluation of defects in β-Ga_2O_3 single crystals grown by edge-defined film-fed growth process *Jpn. J. Appl. Phys.* 55 1202BD

[50] Ueda N, Hosono H, Waseda R and Kawazoe H 1997 Anisotropy of electrical and optical properties in β-Ga_2O_3 single crystals *Appl. Phys. Lett.* 71 933

[51] Schubert M, Korlacki R, Knight S, Hofmann T, Schöche S, Darakchieva V, Janzén E, Monemar B, Gogova D, Thieu Q T, Togashi R, Murakami H, Kumagai Y, Goto K, Kuramata A, Yamakoshi S and Higashiwaki M 2016 Anisotropy, phonon modes, and free charge carrier parameters in monoclinic β-Ga_2O_3 single crystals *Phys. Rev. B* 93 125209

[52] Guo Z, Verma A, Wu X, Sun F, Hickman A, Masui T, Kuramata A, Higashiwaki M, Jena D and Luo T 2015 Anisotropic thermal conductivity in single crystal β-gallium oxide *Appl. Phys. Lett.* 106 111909

[53] Slomski M, Blumenschein N, Paskov P P, Muth J F and Paskova T 2017 Anisotropic thermal conductivity of β-Ga_2O_3 at elevated temperatures: effect of Sn and Fe dopants *J. Appl. Phys.* 121 235104

[54] Qian L X, Liu X Z, Sheng T, Zhang W L, Li Y R and Lai P T 2016 β-Ga_2O_3 solar-blind deep-ultraviolet photodetector based on a four-terminal structure with or without Zener diodes *AIP Adv.* 6 045009

[55] Zhao X, Wu Z, Zhi Y, An Y, Cui W, Li L and Tang W 2017 Improvement for the performance of solar-blind photodetector based on β-Ga_2O_3 thin films by doping Zn *J. Phys. D: Appl. Phys.* 50 085102

[56] Higashiwaki M, Sasaki K, Murakami H, Kumagai Y, Koukitu A, Kuramata A, Masui T and Yamakoshi S 2016 Recent progress in Ga_2O_3 power devices *Semicond. Sci. Technol.* 31 034001

[57] Huang A Q 2017 Power semiconductor devices for smart grid and renewable energy systems *Proceedings of the IEEE* pp. 1-29

[58] Galazka Z, Uecker R, Klimm D, Irmscher K, Naumann M, Pietsch M, Kwasniewski A, Bertram R, Ganschow S and Bickermann M 2017 Scaling-up of bulk β-Ga_2O_3 single crystals by the Czochralski method *ECS J. Solid State Sci. Technol.* 6 Q3007

[59] Galazka Z, Uecker R, Irmscher K, Albrecht M, Klimm D, Pietsch M, Brützam M, Bertram R, Ganschow S and Fornari R 2010 Czochralski growth and characterization of β-Ga_2O_3 single crystals *Cryst. Res. Technol.* 45 1229

[60] Galazka Z, Irmscher K, Uecker R, Bertram R, Pietsch M, Kwasniewski A, Naumann M, Schulz T, Schewski R, Klimm D and Bickermann M 2014

On the bulk β-Ga_2O_3 single crystals grown by the Czochralski method *J. Cryst. Growth* 404 184

[61] Kuramata A, Koshi K, Watanabe S, Yamaoka Y, Masui T and Yamakoshi S 2016 High-quality β-Ga_2O_3 single crystals grown by edge-defined film-fed growth *Jpn. J. Appl. Phys.* 55 1202A2

[62] Vasyltsiv V I, Rym Y I and Zakharko Y M 1996 Optical absorption and photoconductivity at the band edge of β-$Ga_{2-x}In_xO_3$ *Phys. Status Solidi B* 195 653

[63] Cho A Y and Arthur J R 1975 Molecular beam epitaxy *Prog. Solid State Chem.* 10 157

[64] Passlack M, Hong M, Mannaerts J P, Opila R L, Chu S N G, Moriya N, Ren F and Kwo J R 1997 Low D_{it}, thermodynamically stable Ga_2O_3-GaAs interfaces: fabrication, characterization, and modeling *IEEE Trans. Electron Devices* 44 214

[65] Hong M, Mannaerts J P, Bower J E, Kwo J, Passlack M, Hwang W Y and Tu L W 1997 Novel $Ga_2O_3(Gd_2O_3)$ passivation techniques to produce low D_{it} oxide-GaAs interfaces *J. Cryst. Growth* 175 422

[66] Ren F, Abernathy C R, MacKenzie J D, Gila B P, Pearton S J, Hong M, Marcus M A, Schurman M J, Baca A G and Shul R J 1998 Demonstration of GaN MIS diodes by using AlN and $Ga_2O_3(Gd_2O_3)$ as dielectrics *Solid-State Electron.* 42 2177

[67] Guo D, Wu Z, Li P, An Y, Liu H, Guo X, Yan H, Wang G, Sun C, Li L and Tang W 2014 Fabrication of β-Ga_2O_3 thin films and solar-blind photodetectors by laser MBE technology *Opt. Mater. Express* 4 1067

[68] Jenichen B, Braun W, Kaganer V M, Shtukenberg A G, Daeweritz L, Schulz C-G, Ploog K H, and Erko A 2003 Combined molecular beam epitaxy and diffractometer system for *in-situ* x-ray studies of crystal growth *Rev. Sci. Instrum.* 74 1267

[69] Robinson I K and Tweet D J 1992 Surface x-ray diffraction *Rep. Prog. Phys.* 55 599

[70] Cohen P I, Petrich G S, Pukite P R, Whaley G J and Arrott A S 1989 Birth-death models of epitaxy: I. Diffraction oscillations from low index surfaces *Surf. Sci.* 216 222

[71] Petrich G S, Pukite P R, Wowchak A M, Whaley G J, Cohen P I and Arrott A S 1989 On the origin of RHEED intensity oscillations *J. Cryst. Growth* 95 23

[72] Pukite P R, Cohen P I and Batra S 1988 The contribution of atomic steps to reflection high energy electron diffraction from semiconductor surfaces *NATO ASI Ser. B* 188 427

[73] Peng L M and Whelan M J 1990 Dynamkal RHEED from MBE growing surfaces *Surf. Sci.* 238 L446

[74] Peng L M and Whelan M J 1991 Dynamical calculations for RHEED from MBE growing surfaces. I. Growth on a low-index surface *Proc. R. Soc. Lond.* A432 195

[75] Peng L M and Whelan M J 1991 Dynamical calculations for RHEED from MBE growing surfaces. II. Growth interruption and surface recovery *Proc. R. Soc. Lond.* A435 257

[76] Peng L M and Whelan M J 1991 Dynamical calculations for RHEED from MBE growing surfaces. III. Heteroepitaxial growth and interface formation *Proc. R. Soc. Lond.* A435 269

[77] Orlandi F, Mezzadri F, Calestani G, Boschi F and Fornari R 2015 Thermal expansion coefficients of β-Ga_2O_3 single crystals *Appl. Phys. Express* 8 111101

[78] Víllora E G, Shimamura K, Ujiie T and Aoki K 2008 Electrical conductivity and lattice expansion of β-Ga_2O_3 below room temperature *Appl. Phys. Lett.* 92 202118

[79] Kranert C, Lenzner J, Jenderka M, Lorenz M, von Wenckstern H, Schmidt-Grund R and Grundmann M 2014 Lattice parameters and Raman-active phonon modes of $(In_xGa_{1-x})_2O_3$ for x $\leq$ 0.4 *J. Appl. Phys.* 116 013505

[80] Kim H W and Kim N H 2004 Annealing effects on the properties of Ga_2O_3 thin films grown on sapphire by the metal organic chemical vapor deposition *Appl. Surf. Sci.* 230 301

[81] Ma Y-M, Chen H-Y, Yang K-F, Li M, Cui Q-L, Liu J and Zou G-T 2008 High-pressure and high-temperature behaviour of gallium oxides *Chin. Phys. Lett.* 25 1603

[82] Kaneko K, Kawanowa H, Ito H and Fujita S 2012 Evaluation of misfit relaxation in α-Ga_2O_3 epitaxial growth on α-Al_2O_3 substrate *Jpn. J. Appl. Phys.* 51 020201

[83] Santia M D, Tandon N and Albrecht J D 2016 Thermal properties of β-Ga_2O_3 from first principles *MRS Adv.* 1 109

[84] Yasumasa O and Yozo T 12 1984 Precise determination of lattice parameter and thermal expansion coefficient of silicon between 300 and 1500 K *J. Appl. Phys.* 56 314

[85] Einstein A 1907 Die Plancksche Theorie der Strahlung und die Theorie der spezifischen Wärme *Ann. Phys.* 22 180

[86] Glazov V M and Pashinkin A S 20007 Thermal expansion and heat capacity of GaAs and InAs *Inorg. Mater.* 36 225

[87] Ibach H 1969 Thermal expansion of silicon and zinc oxide (I) *Phys. Status Solidi(b)* 31625

[88] Yim W M and Paff R J 1974 Thermal expansion of AlN, sapphire, and silicon *J. Appl. Phys.* 45 1456

[89] Eckert L J and Bradt R C 1973 Thermal expansion of α-Ga_2O_3 *J. Am. Ceram. Soc.* 56 229

[90] Vogt P and Bierwagen O 2016 Reaction kinetics and growth window for plasma-assisted molecular beam epitaxy of Ga_2O_3: incorporation of Ga vs. Ga_2O desorption *Appl. Phys. Lett.* 108 072101

[91] Baldini M, Albrecht M, Fiedler A, Irmscher K, Klimm D, Schewski R and Wagner G 2016 Semiconducting Sn-doped β-Ga_2O_3 homoepitaxial layers grown by metal organic vapour-phase epitaxy *J. Mater. Sci.* 51 3650

[92] Marie P, Portier X and Cardin J 2008 Growth and characterization of gallium oxide thin films by radiofrequency magnetron sputtering *Phys. Status Solidi A* 205 1943

[93] Nakagomi S and Kokubun Y 2017 Crystal orientation of monoclinic β-Ga_2O_3 thin films formed on cubic MgO substrates with a γ-Ga_2O_3 interfacial layer *J. Cryst. Growth* 479 67

[94] Kaneko K, Ito H, Lee S.-D. and Fujita S 2013 Oriented growth of beta gallium oxide thin films on yttrium-stabilized zirconia substrates *Phys. Status Solidi C* 10 1596

[95] Holland M, Stanley C R, Reid W, Hill R J W, Moran D A J, Thayne I, Paterson G W and Long A R 2007 Ga_2O_3 grown on GaAs by molecular beam epitaxy for metal oxide semiconductor field effect transistors *J. Vac. Sci. Technol. B* 25 1706

[96] Bermudez V 2006 The structure of low-index surfaces of β-Ga_2O_3 *Chem. Phys.* 323 193

[97] Wagner G, Baldini M, Gogova D, Schmidbauer M, Schewski R, Albrecht M, Galazka Z, Klimm D and Fornari R 2014 Homoepitaxial growth of β-Ga_2O_3 layers by metal-organic vapor phase epitaxy *Phys. Status Solidi A* 211 27

[98] Schewski R, Baldini M, Irmscher K, Fiedler A, Markurt T, Neuschulz B, Remmele T, Schulz T, Wagner G, Galazka Z and Albrecht M 2016 Evolution of planar defects during homoepitaxial growth of β-Ga_2O_3 layers on (100) substrates—a quantitative model *J. Appl. Phys.* 120 225308

[99] Wagner G, Baldini M, Gogova D, Schmidbauer M, Schewski R, Albrecht M, Galazka Z, Klimm D and Fornari R 2014 Homoepitaxial growth of β-Ga_2O_3 layers by metal-organic vapor phase epitaxy *Phys. Status Solidi A* 211 27

[100] Irmscher K, Galazka Z, Pietsch M, Uecker R and Fornari R 2011 Electrical properties of β-Ga_2O_3 single crystals grown by the Czochralski method *J. Appl. Phys.* 110 063720

[101] Baldini M, Albrecht M, Fiedler A, Irmscher K, Schewski R and Wagner G 2017 Si- and Sn-doped homoepitaxial β-Ga_2O_3 layers grown by MOVPE on (010)-oriented substrates *ECS J. Solid State Sci. Technol.* 6 Q3040

[102] Cowley J and Moodie A F 1957 Fourier images: I - The point source *Proc. Phys. Soc.* B70 (1957) 486, 497, and 505

[103] Bethe H 1928 Theorie der Beugung von Elektronen an Kristallen *Ann. Phys.* 392 55

[104] Braun W, Möller H and Zhang Y-H 1998 Reflection high-energy electron diffraction during substrate rotation: a new dimension for *in-situ* characterization *J. Vac. Sci. Technol. B* 16 1507

[105] Fukutani K, Daimon H and Ino S 1992 Reflection high-energy electron diffraction study of the growth of Ge on the Ge(111) surface *J. Appl. Phys.* 31 3429

[106] Berrie C L and Leone S R 2000 Observation of monolayer and bilayer period RHEED oscillations during epitaxial growth of Ge on Ge(100) *J. Cryst. Growth* 216 159

[107] Amano H, Akasaki I, Hiramatsu K, Koide N and Sawaki N 1988 Effects of the buffer layer in metalorganic vapour phase epitaxy of GaN on sapphire substrate *Thin Solid Films* 163 415

[108] Ivanov S V, Shubinaa T V, Jmerik V N, Vekshin V A, Kopev P S and Monemar B 2004 Plasma-assisted MBE growth and characterization of InN on sapphire *J. Cryst. Growth* 269 1

[109] Vispute R D, Talyansky V, Trajanovic Z, Choopun S, Downes M, Sharma R P, Venkatesan T, Woods M C, Lareau R T, Jones K A and Iliadis A A 1997 High quality crystalline ZnO buffer layers on sapphire (001) by pulsed laser deposition for III-V nitrides *Appl. Phys. Lett.* 70 2735

[110] French R H 1990 Electronic band structure of Al_2O_3, with comparison to Alon and AIN *J. Am. Ceram. Soc.* 73 477

[111] Krishnamoorthy S, Xia Z, Joishi C, Zhang Y, McGlone J, Johnson J, Brenner M, Arehart A R, Hwang J, Lodha S and Rajan S 2017 Modulation-doped β-$(Al_{0.2}Ga_{0.8})_2O_3$/Ga_2O_3 field-effect transistor *Appl. Phys. Lett.* 111 023502

[112] Holý V, Pietsch U and Baumbach T 1999 High-resolution x-ray scattering from thin films and multilayers *Springer-Verlag Berlin Heidelberg New York* ISBN 978-3-540-49625-0

[113] Chapek D L, Conrad J R, Matyi R J and Felch S B 1994 Structure characterization of plasma-doped silicon by high resolution x-ray diffraction *J. Vac. Sci. Technol.* 12 951

[114] Proessdorf A, Niehle M, Hanke M, Grosse F, Kaganer V, Bierwagen O and Trampert A 2014 Epitaxial polymorphism of La_2O_3 on Si(111) studied by *in-situ* x-ray diffraction *Appl. Phys. Lett.* 105 021601

[115] Cheng Z, Hanke M, Galazka Z and Trampert A 2018 Growth mode evolution during (100)-oriented β-Ga_2O_3 homoepitaxy *Nanotechnology* 29 395705

[116] Kiessig H 1931 Interferenz von Röntgenstrahlen an dünnen Schichten *Ann. Physik* 10 715

[117] Parratt L G 1954 Surface studies of solids by total reflections of x-rays *Phys. Rev.* 95 359

[118] Chaplygin G V and Semiletov S A 1976 Preparation, structure and electrical properties of epitaxial films of Ga_2O_3 on sapphire substrates *Thin Solid Films* 32 321

[119] Nakagomi S and Kokubun Y 2012 Crystal orientation of β-Ga_2O_3 thin films formed on c-plane and a-plane sapphire substrate *J. Cryst. Growth* 349 12

[120] Wadley H N G, Lu Y and Goldman J A 1995 Ultrasonic determination of single crystal sapphire fiber modulus *J. Nondestruct. Eval.* 14 31

Appendices

A Sketch of the PHARAO beamline

Appendix A provides the supplementary description to the dedicated PHARAO endstation U125/2-KMC at BESSY II, HZB. Figure A.1 is the sketch of the combination of MBE and diffractometer. Figure A.2 presents the six-circle diffractometer.

A.1 Combination of MBE and diffractometer

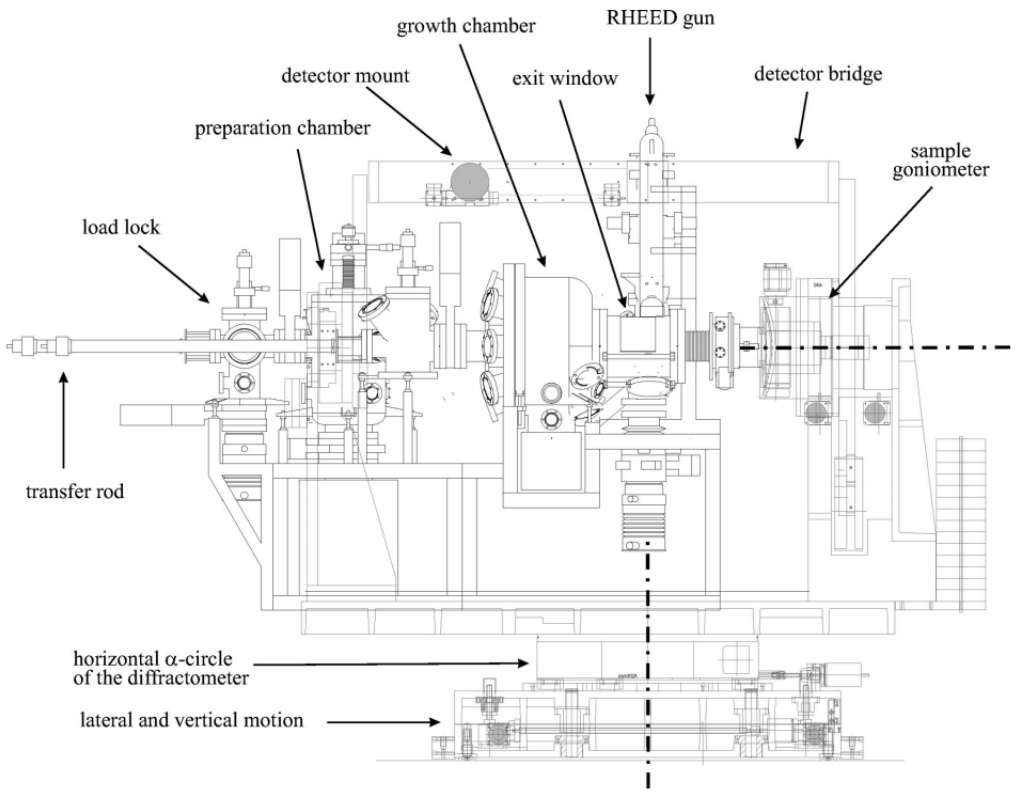

Figure A.1 This schematic shows the MBE system and the six-circle diffractometer at the PHARAO beamline U125/2-KMC at BESSY II (Helmholtz-Zentrum Berlin). The sample is positioned at the intersection of the horizontal and vertical axis of the diffractometer, facing left.[68]

A.2 The six-circle diffractometer

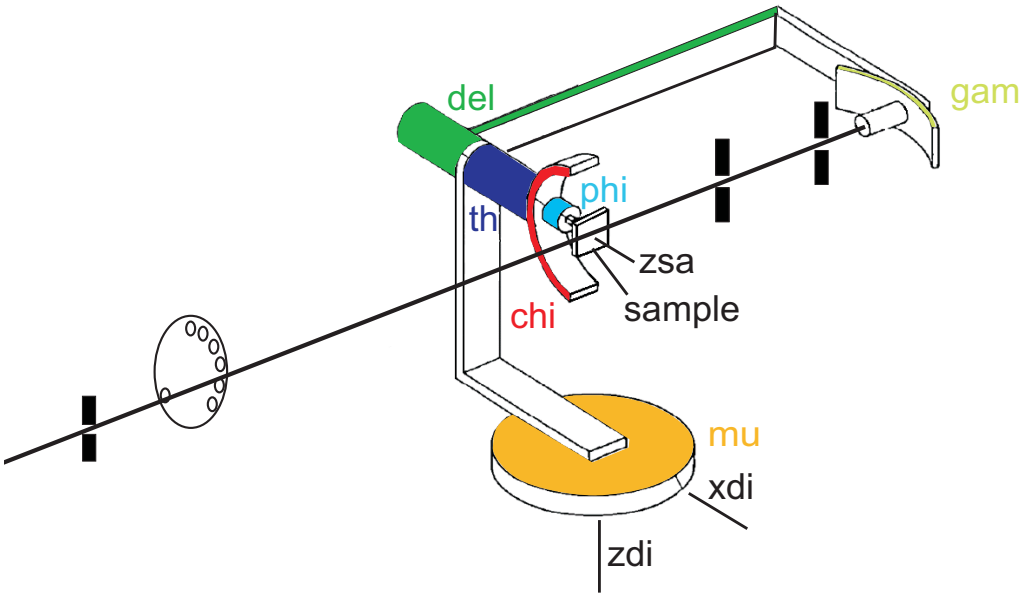

Figure A.2 A schematic of the six-circle diffractometer installed at the PHARAO beamline with all the motors at zero position. The six circles of mu, gam, del, th, phi, and chi are explicitly presented. The entire diffractometer moves the mu circle; the rotation and tilting of the sample depend on th, phi,and chi; the detector moves with gam and del.

B Code of numerical simulation

```
SetDirectory[" Please insert the directory of the imported files"];
(*GITTERPARAMETER WELLENLAENGE*)
LAMBDA = 0.5;


(*EXPERIMENT*)
s1 = Import["__ga2o3_beta_1_uc_284atoms.csv", "csv"];
s2 = Import["m8_2045.txt", "table"];

(*Al2O3*)
as = 4.757; bs = 4.757; cs = 12.988; alphas = 90; betas = 90; gammas = 120;
rs = Import["__al2o3_alpha_1_uc_30atoms.csv", "CSV"];

(*ALPHA Ga2O3*)
aa = 4.9791; ba = 4.9791; ca = 13.437; alphaa = 90; betaa = 90; gammaa = 120;
ra = Import["__ga2o3_alpha_2_uc_41atoms.csv", "CSV"];

(*BETA Ga2O3*)
a = 12.214; b = 3.0371; c = 5.7981; alpha = 90; beta = 103.83; gamma = 90;
rb = Import["__ga2o3_beta_1_uc_20atoms.csv", "CSV"];

(*Si****)
(*a =5.43;b=5.43;c=5.43; alpha=90;  beta=90; gamma=90; LAMBDA=0.5;
r=Import["si_1_uc_313961__.csv","CSV"];*)

rb[[1]];
 AtomAnzSub = Length[rs];
 AtomAnzBeta = Length[rb];
 AtomAnzAlpha = Length[ra];

(*STRUKTURAMPLITUDE*)
f1a[h_, k_, l_] := Abs[Sum[Exp[-2 Pi I ra[[i]].{h, k, l}], {i, 1, AtomAnzAlpha}]];
f1b[h_, k_, l_] := Abs[Sum[Exp[-2 Pi I rb[[i]].{h, k, l}], {i, 1, AtomAnzBeta}]];
f1s[h_, k_, l_] := Abs[Sum[Exp[-2 Pi I rs[[i]].{h, k, l}], {i, 1, AtomAnzSub}]];
(*ContourPlot[Log[f1[h,0,l]],{h,-5,5},{l,-5,5},PlotRange→Automatic]
 Plot3D[f1[qx,qy,0],{qx,-3,3},{qy,-3,3}]*)

(*GITTERAMPLITUDE*)
f2[U1_, U2_, U3_, h_, k_, l_] := (Sin[U1*Pi*h]/Sin[Pi*h])*(Sin[U2*Pi*k]/Sin[Pi*k])*
   (Sin[U3*Pi*l]/Sin[Pi*l]);
(*Plot[Log[f2[1,1,10,1.0,1.0,l]],{l,0,6}]
 ContourPlot[f2[50,20,20,h,0.1,l],{h,0,5},{l,0,5}]
 Plot[Log[f1[1,1,l]*f2[1,1,1000,1.0,1.0,l]],{l,0,6},Mesh->All]*)

(*BRAGGWINKEL = tth/2*)
```

Figure B.1 Code of the structure factor numerical calculation for a kinematic approximation, as performed in Wolfram Mathematica 10, part I.

```
f3 =
  (1 + 2 Cos[alpha Degree] Cos[beta Degree] Cos[gamma Degree] - Cos[alpha Degree]^2 - Cos[beta Degree]^
     Cos[gamma Degree]^2)^(-1);
f4[h_, k_, l_] := 1/a^2 h^2 * Sin[alpha Degree] * Sin[alpha Degree] +
   1/b^2 k^2 * Sin[beta Degree] * Sin[beta Degree] + 1/c^2 l^2 * Sin[gamma Degree] * Sin[gamma Degree] +

       2 h*k/(a*b) (Cos[alpha Degree] Cos[beta Degree] - Cos[gamma Degree]) +
       2 k*l/(b*c) (Cos[beta Degree] Cos[gamma Degree] - Cos[alpha Degree]) +
       2 l*h/(a*c) (Cos[gamma Degree] Cos[alpha Degree] - Cos[beta Degree]);
d[h_, k_, l_] := Sqrt[(f3 * f4[h, k, l])^(-1)] ;
th[h_, k_, l_] := ArcSin[LAMBDA / 2 / d[h, k, l]];
|


Show[
 Plot[1000 * {Log[Exp[-(0 Pi / d[l, 0, 0])^2]
       * (Abs[
          f1b[l, 0, 0] / (1 - Exp[2 Pi I l]) + 0.1 * f1b[l, 0, 0] * (1 - Exp[2 * 2 Pi I l]) / (1 - Exp[2 Pi I l])
         ])^2

     ]} + 0 * {Log[Exp[-(0 Pi / d[l, 0, 0])^2]
       * (Abs[
          f1b[l, 0, 0] * (1 - Exp[10 * 2 Pi I l]) / (1 - Exp[2 Pi I l])
         ])^2

     ]},
  {l, 0, 7.1}, PlotStyle -> {Blue, Thick}, PlotRange → Full]
]


gr = Plot[1000 * {Log[Exp[-(0 Pi / d[l, 0, 0])^2]
       * (Abs[
          f1b[l, 0, 0] / (1 - Exp[2 Pi I l]) + 0 * f1b[l, 0, 0] * (1 - Exp[7 * 2 Pi I l]) / (1 - Exp[2 Pi I l])
         ])^2

     ]} + 0 * {Log[Exp[-(0 Pi / d[l, 0, 0])^2]
       * (Abs[
          f1b[l, 0, 0] * (1 - Exp[10 * 2 Pi I l]) / (1 - Exp[2 Pi I l])
         ])^2
```

Figure B.2 Code of the structure factor numerical calculation for a kinematic approximation, as performed in Wolfram Mathematica 10, part II.

Acknowledgement

I would like to express my sincere gratitude to those who contributed to this thesis and supported me in the scientific research and personal improvement in the last four years.

My deepest gratitude goes to Prof. Dr. Henning Riechert for this precious opportunity he gave that allowed me to accomplish my doctorate research at the Paul-Drude-Institut für Festkörperelektronik (PDI).

I am very much grateful to Dr. Michael Hanke. He is a very knowledgeable and kind scientist who guides me into the reciprocal world. I express my appreciation to all the valuable discussions with him, which greatly improved my understanding in HRXRD and inspired many ideas in the research.

Many thanks go to Dr. Achim Trampert, the head of the microstructure department for his valuable advices and the introduction to HRTEM. I would like to thank Dr. Oliver Bierwagen for his detailed introduction to MBE and group-III sesquioxides.

I thank Dr. Bernd Jenichen for the XRD introduction, Steffen Behnke for his great technical supports in both the MBE and the PHARAO beamline, and Claudia Herrmann for her kind introduction to AFM and the cleanroom. I also would like to thank my office colleagues Hardy Drube, Markus Terker, and Lars Nicolai for kind scientific discussions and a very convenient working atmosphere.

Eidesstattliche Erklärung

Ich erkläre hiermit an Eides statt, dass ich die Dissertation selbständig und nur unter Verwendung der von mir gemäß §7 Abs. 3 der Promotionsordnung der Mathematisch-Naturwissenschaftlichen Fakultät I, veröffentlicht im Amtlichen Mitteilungsblatt der Humboldt-Universität zu Berlin Nr. 126/2014 am 01.04.2015, angegebenen Hilfsmittel angefertigt habe.

Berlin, den 7 Februar 2019 . . . . . .